Charge Transport in Organic Crystals

seit 1558

vorgelegt dem Rat der Physikalisch-Astronomischen Fakultät
der Friedrich-Schiller-Universität Jena

von Dipl.-Phys. Frank Ortmann

geboren am 08.10.1980 in Mühlhausen/Thüringen

Gutachter:

1. Prof. Dr. Friedhelm Bechstedt, Friedrich-Schiller-Universität Jena

2. Prof. Dr. Jens Pflaum, Universität Würzburg

3. Dr. Peter Bobbert, TU Eindhoven, Netherlands

Tag der letzten Rigorosumsprüfung: 02.07.2009

Tag der öffentlichen Verteidigung: 15.07.2009

Contents

Chapter 1

Introduction

1.1 Scientific Background

In recent years, applications based on organic electronics have become common as can be seen from displays based upon organic light emitting diodes (OLEDs) [1–3]. Organic semiconductors have also been used in organic electronic devices such as organic field effect transistors (OFETs) [4–9], organic thin film transistors (OTFTs) [10, 11], or organic solar cells [12–14]. Besides π-conjugated polymers, in particular organic molecular crystals (OMCs) have attracted strong experimental and theoretical interest since the long-range order in these materials allows for the study of fundamental questions in physics and chemistry [8, 15–19]. This includes especially investigations of underlying elementary processes and interactions that lead to their specific optical and transport properties, which can be markedly different from those in conventional covalent or ionic crystals such as the traditional semiconductors Si and GaAs.

The charge transport in OMCs has been under strong debate ever since the pioneering experimental work of Karl *et al.* [20] who spent decades preparing and measuring high quality organic crystals. Many of these results are still a benchmark today. Karl even succeeded to demonstrate hot carrier effects in naphthalene crystals. [21] Despite such outstanding experimental achievements, a recent review article states that the "*understanding of charge transport ... remains limited.*" [8] Similarly another recent review expects that comprehensive understanding will arise in the future from several improvements in the theoretical modeling and description of transport. This includes the number of computational studies that has to be increased but more importantly the required higher level of the theoretical treatment. [22] The dominating impression from such conclusions in the most recent reviews and books is that many fundamental questions are not satisfactorily answered.

The natural question arises what is actually understood so far about the charge trans-

port in OMCs and why is the situation by far more complex than in traditional inorganic
semiconductors. An excellent indicator of the difficulties in understanding and describing
charge transport in organic crystals can be found in a monograph by Silinish and Čápek.
[23] They speak of a *"mobility puzzle"* which is that *"on one hand, the mean free path l_0
of the carrier ... from room temperature to down to 150 K is actually of the order of lattice
constant a_0 ($l_0 \approx a_0$) and strongly suggests a hopping model approach. On the other hand, the
typical $\mu(T)$ dependences ... $\mu \propto T^{-\gamma}$ are often supposed to speak in favor of some band-type
carrier transport."*[1] [23] Thereby hopping or band transport in organic crystals are assumed
to be the exclusive transport mechanisms for either localized or delocalized charge carriers,
respectively.

In fact, the bare electronic bandwidth of organic molecular crystals can reach 500 meV
[24–26] or even more [27]. In comparison to the thermal energy this is large and a supporting
argument for band-like transport similar to the case of conventional inorganic semiconductors.
A large bare bandwidth, however, is not a sufficient criterion for this mode of transport in
organic semiconductors and can only serve as an indicator for high mobilities. This is different
to the traditional inorganic semiconductors. The reason is that, due to thermal (vibrational)
disorder, the bandwidth (i.e. the electronic coupling) is on average smaller than the value
obtained for fixed geometry at zero temperature [28]. The effect is known as band narrowing
and can be rationalized by means of the polaron concept. [25, 29, 30] Such polaron effects
may trigger a transition from band transport to hopping motion.

The formation of polarons has been studied in the past but the influence on carrier motion
is by far not sufficiently described and understood. In fact, so far there was only one single
paper applying a sophisticated (non-perturbative) transport theory along with state-of-the-
art *ab initio* calculations for material parameters. [31] In contrast thereto, several model
studies appeared during the last decades [32–37] which, however, do not easily facilitate
direct and systematic computational investigations for real materials. Other studies, based
on the propagation of electron wave packets using a one-dimensional Schrödinger equation,
are limited to high temperatures and might be too demanding for studies of three-dimensional
crystals. [28, 38] As a result of these studies the community has seemingly come to a common
belief that, at least for the high temperature regime, the incoherent hopping dominates in
organic crystals. The contribution of coherent band transport is still under debate and
depends strongly on the temperature. In particular, the influence of the common assumption
of narrow bands on the description is poorly understood. [34] The above quotations from
various reviews show that the accurate modeling of both transport mechanisms remains an
important task to obtain a deeper understanding of charge transport in organic crystals.

---

[1]μ is the charge carrier mobility.

Apart from these fundamental questions about the transport mechanism which are not satisfactorily answered, there is also the issue of the anisotropy of the carrier mobility in real crystals, which has been rarely studied theoretically so far, even though many experiments exist. [16, 20, 39–43] The anisotropy is of special interest because it allows to study the relationship between molecular orientation and transport efficiency. Such an analysis must necessarily go beyond the various model studies which have been carried out in literature. It has also not been addressed so far by the methods based on the propagation of the Schrödinger equation, presumably because it is computationally too expensive in higher dimensions than 1D.

In order to investigate the mobility anisotropy for a real crystal, a combination of a sophisticated transport theory on the one hand and a complete set of *first principles* material parameters on the other hand is required. A visualization of the transport channels in real space would also be helpful to improve the basic understanding of the mobility anisotropy and its relation to the stacking motif of the molecules in OMCs.

1.2   How This Work Contributes

This work deals with the transport of charges in crystalline organic semiconductors. In view of the above-mentioned "mobility puzzle" it aims at providing a deeper understanding and improved description of the relevant processes for charge transport in these materials. This is done from two aspects: (1) a theoretical analysis and (2) computational studies of various organic crystals.

In the first part of this thesis, a novel theory is developed which describes the motion of dressed charge carriers (i.e. charge carriers with their accompanying lattice polarization cloud[2]) including the full anisotropy and temperature dependence. Since the modeling of charge transport is essentially the modeling of the scattering of charge carriers, I have developed a transport theory based on the Holstein Hamiltonian for electron-phonon scattering. The carrier mobility is derived from a non-perturbative evaluation of the Kubo formula and represents a generalization of the original Holstein model. [29]

A schematic representation how this new theory is related to other approaches is depicted in Fig. 1.1. The Holstein model (black frame) is based on the assumptions of purely local electron-phonon coupling and narrow electronic bands. Previous extensions of the Holstein model were focused on the inclusion of additional non-local electron-phonon interaction [44] but were still restricted to narrow bands. In the present theory (red frame in Fig. 1.1)

---

[2]With lattice polarization the polarization based on the change of geometry (electron-phonon interaction) is meant in contrast to the electronic polarization based on electron-electron interaction.
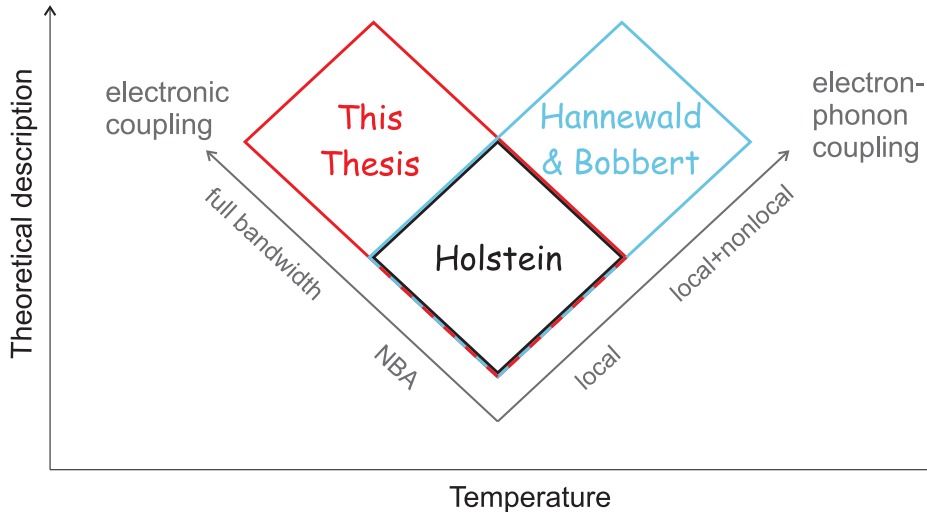
Figure 1.1: Schematic illustration of the development of the present theory (red frame) in relation to the previous theory by Hannewald and Bobbert [44] (blue frame) and Holstein's small polaron model [29] (black frame).

the assumption of narrow bands is dropped and a generalization towards the full electronic bandwidth is derived.

Within the applied framework one can describe the electron-phonon interaction microscopically and take other scattering mechanisms (impurity, electron-electron scattering, etc.) implicitly into account. As an important finding of this part of the thesis, the carrier mobility is interpreted in terms of contributing scattering events, which nicely illustrates the different transport mechanisms. Although originally designed for organic molecular crystals, where the lattice polarization dominates, the developed theory is valid for arbitrary bulk semiconductors, because the temperature dependence of the mobility in the traditional inorganic semiconductors is also governed by the lattice polarization. [45]

The second part of the thesis is an *ab initio* investigation of organic materials with potentially high carrier mobilities. It is focused on the understanding of the relationship between transport anisotropy and underlying geometric structure. This second part includes basic geometry and electronic structure simulations from *first principles* and, on top of these studies, an investigation about the transport characteristics including the simulation of the temperature dependent mobility tensor of the charge carriers. The mobility formula of the first part is applied hereby to naphthalene crystals and the structure/property relationship is studied for durene and guanine crystals, which serve as representatives for two different classes of OMCs. Similarities and differences are discussed in detail.

1.3   Goals of This Work

- To derive an analytical expression for the charge carrier mobility.

- The mobility formula should be usable directly with *ab initio* parameters for arbitrary crystalline materials and shall provide a starting point for computational studies from *first principles.*

- To analyze the mobility with respect to coherent band transport and incoherent thermally activated hopping, in particular, the crossover point and the relative importance of both contributions.

- To gain more insight into the temperature dependence of the mobility. The $T^{-\gamma}$ power law dependence of the mobility and the role of the parameter γ deserve particular attention.

- To establish the connection between polaron transport theories and the Boltzmann transport equation.

- To study a diverse set of molecular crystals which might be good charge-transport materials.

- To investigate the relationship between mobility anisotropy and molecular geometry.

- To improve the understanding of the mobility anisotropy by an intuitive visualization tool.

1.4 Outline

In Chapter 2 an introduction to the concept of polarons is given. This includes a general discussion of polaronic effects along with an example from experiments as well as an introduction of basic terms like electronic coupling and electron-phonon coupling. An analytical description of the polarons is given in Chapter 3. This chapter introduces the formalism and notation developed previously [25], but its presentation is adapted to the present needs in the thesis. Chapter 4 presents a novel polaron transport theory which I have developed in the course of my studies. The derivation is accompanied by a comprehensive discussion of the underlying physical concepts. The relation of limiting cases to other theories is analyzed as well. The transport theory is illustrated in Chapter 5 with a detailed discussion of its features which is based on numerical studies of a model crystal. Chapter 6 compiles the findings from the computational studies of the organic crystals naphthalene, durene, and guanine, which are obtained with *ab initio* material parameters of these crystals. It covers results on structural, vibrational, and electronic properties as well as the description of charge transport based on the carrier mobilities. The discussion of the mobilities includes its temperature dependence and anisotropy. A summary and an outlook in the last chapter complete the thesis.

Chapter 2

Introduction to Polarons

2.1 What is a Polaron?

A polaron is a dressed charge carrier and is therefore always based on two ingredients: a charge carrier (electron or hole) and a polarization cloud that is bound to this charge carrier. The polarization cloud can be an intrinsic one or an extrinsic one as can best be seen with an example. Consider the DNA molecule with its famous double helix form in aqueous solution and consider one of the DNA bases being charged. This electron or hole will cause a reaction of the molecule upon charging which is seen in its deformation (intrinsic polarization). On the other hand it will cause a reorientation of surrounding water molecules owing to their dipoles moments (extrinsic polarization). Intrinsic or extrinsic reactions can be described as polarization effects which occur because the nuclei degrees of freedom couple to the charge. As a consequence of the coupling, the energy level of ionization is shifted downwards upon relaxation. The carrier is bound with the polaron binding energy E_p. Or in other words, the polarization cloud is bound to the carrier.

Similarly, in bulk semiconductors, which are under investigation here, an intrinsic coupling of excess charges to the atomic/molecular vibrations is observed. [23] An extrinsic effect can also be found at crystal surfaces where the charge polarizes the medium above the surface. [17] In this thesis I am concentrating on intrinsic polarization in crystalline bulk materials and OMCs in particular because already the intrinsic transport mechanism is still not well described in OMCs. [8, 22, 23]

So far, the effect of an excess charge on the material has been discussed as a response of the host crystal leading to a polarization cloud. Another viewpoint is of equal interest. One can ask the other way around what is the effect of vibrating atoms/molecules on a traveling charge carrier? Taking this point of view one is at the heart of the important question how the temperature influences the charge motion. Clearly, the effective potential felt by the charge carrier is changed by changes in the geometry and the carrier will be scattered by
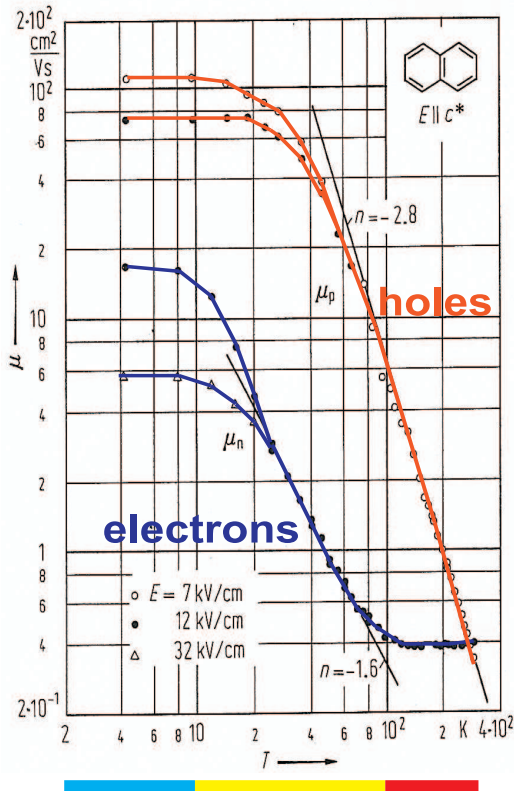
Figure 2.1: Experimental charge carrier mobility in c^* direction in naphthalene crystals (see geometry in Fig. 2.2) reproduced from Ref. [20]. For clarity, solid lines are guide to the eye. Electric-field dependencies representing hot carrier effects are visible for low temperatures where respective curves are split by different electric field strengths.

such changes in the potential. Increasing temperature amplifies this effect and thus reduces the mean free path of the carrier. Since the atomic motion always implies a potential change, such an interaction is present everywhere, though with different strength. This important interaction between the electronic and nuclei degrees of freedom is the basis of the polaron concept and is called electron-phonon coupling. Hereby, the vibrations are described by lattice phonons.

2.2 Polaron Transport

Polaronic effects in charge carrier transport are strong in organic semiconductors like organic molecular crystals and semiconductors based on polymers. Fig. 2.1 shows the very prominent example of carrier mobility studies by Karl and co-workers. [20, 21] These studies were carried out at single crystals of naphthalene, the structure of which is depicted in Fig. 2.2.

Figure 2.1 shows the temperature dependence of the carrier mobilities along a specific direction which exhibits some interesting features. For almost all temperatures is the mobility a decreasing function of temperature. There are two exceptions. The first exception (indicated by a blue bar in Fig. 2.1) is the low-T limit, where the mobilities approach a constant value. Such a plateau is seen in all directions for electrons and holes for different applied voltages. The second exception (red bar in Fig. 2.1), which appears in the regime between 100 K and

Figure 2.2: Naphthalene crystal structure. (a) A view along c^* (monoclinic b axis up) shows a 2D herring-bone stacking of molecules in planes. (b) A view in b direction exhibits the stacking of such herring-bone planes in the perpendicular direction.

300 K, is observed for the electrons only. In this temperature range a pronounced plateau is measured which at least allows for the possibility that the mobilities might increase for larger T again. In between (yellow bar in Fig. 2.1), the mobility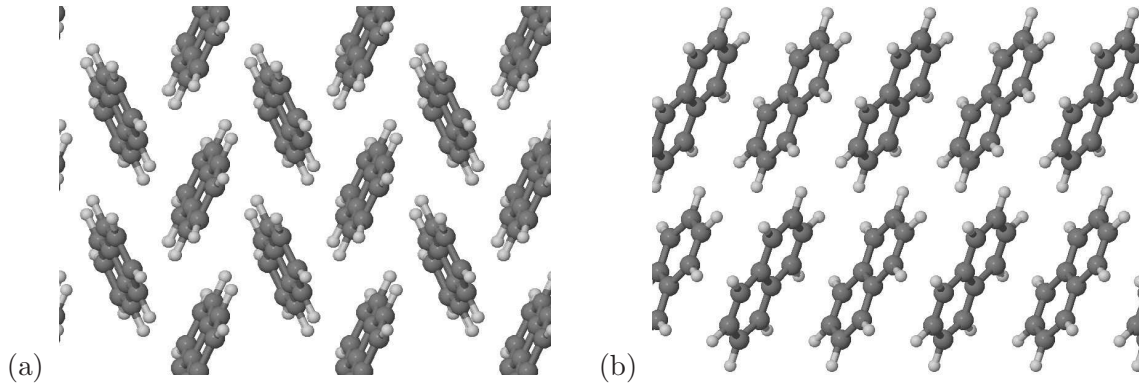 decrease follows a power-law dependence according to $T^{-\gamma}$ with $\gamma = 2.8$ for holes and $\gamma = 1.6$ for electrons. The three regimes indicate that different transport modes operate at different temperatures. Such a complex characteristic cannot be explained with traditional approaches to carrier transport such as the Boltzmann equation based on the assumption of band transport. It cannot be modeled by hopping approaches such as the classical Marcus theory [46, 47] either. It puts high demand on a unified theory. In particular it requires better modeling such as the introduction of polarons on a quantum mechanical basis. In the present thesis I will explain the underlying mechanisms in detail which may lead to the observed temperature dependence of the mobility.

What is the difference to traditional semiconductors like Si or GaAs that the charge transport in OMCs cannot be simulated by the Boltzmann equation? There is a pronounced difference in the bandwidths and, more importantly, the strength of electron-phonon coupling. While the bare electronic bandwidths of organic single crystals rarely exceed 700 meV [27, 48, 49] the bandwidths of traditional semiconductors are one order of magnitude larger. On the other hand, the electron-phonon interaction is stronger in organic semiconductors than in the technologically relevant inorganic ones. This is due to the fact that the relevant frequencies of scattering phonons are much lower in OMCs or polymers since these materials are softer. For instance, the weak van der Waals bonds in OMCs give rise to intermolecular vibrations around 100 cm^{-1}. The resulting larger vibration amplitudes lead to a larger variation of the wavefunction overlap of adjacent sites (i.e. the variation of the electronic coupling) [50]. The changes in the electronic coupling with varying geometry (i.e. the electron-phonon coupling) are stronger.

In general, however, polaronic effects are not simply present or absent. Similarly, the strength of the electron-phonon interaction is not either weak or strong but can vary continously. This also holds for the bandwidth. Inorganic semiconductors can also have small bandwidths like, e.g., transition-metal-based crystals with narrow d-bands or bands derived from superlattices. As a consequence, one needs a unified theory that describes charge transport not only in the two limiting cases introduced before but which also describes a seamless transition for all intermediate materials. A theory is required which is valid for continously varying material parameters. In particular, the interesting organic crystals like pentacene, naphthalene, durene, or rubrene are exactly such materials for which an assignment to either limit is not valid for all temperatures. In addition, the limit of diminishing electron-phonon interaction of a sophisticated polaron transport theory should also cover the description of the bare particles (undressed electrons or holes) and give the same results as obtained from the Boltzmann equation.

2.3 Description of Polarons

2.3.1 Holstein Picture

Since Holstein's papers on "Studies of polaron motion" half a century ago [29, 51] using a one-dimensional molecular crystal model there is an ongoing discussion in literature about polaron sizes in materials. This is motivated by the theoretical treatment because the size of the polaron governs the theoretical means used to describe their transport characteristics in most of the studies carried out so far. These methods are restricted to either small or large polarons. In order to follow this discussion one should, as a first step, define a size to which the polaron size is compared. This is typically a lattice constant or a few.

Holstein introduced an energy ratio between polaron binding energy E_p and electronic coupling, namely $\frac{E_p}{B}$, where B is the electronic bandwidth. This ratio is directly related to the polaron size as obtained from his classical considerations about polarons. [51] For small $\frac{E_p}{B}$ the electronic coupling dominates and the electron-phonon interaction can be treated as a perturbation. This is the limit of large polarons. In the other case of a large ratio $\frac{E_p}{B}$, the electronic coupling is treated as a perturbation to localized polarons. The latter case is closely related to the narrow-band approximation (NBA) which is expressed in $B \to 0$. This approximation has been assumed in all subsequent studies on polaron transport in the tradition of Holstein's model [32, 33, 35, 44] and has lead to the term "small polaron" in connection to the Holstein picture. For small polarons the delocalization aspect of the electronic coupling is overcompensated by the localization aspect introduced by polaron binding. Localized polarons are assumed to be confined to either one or a few (molecular) sites.

Nowadays the Hamiltonian

$$H = \sum_{MN} a_M^\dagger \varepsilon_{MN} a_N + \sum_{M\mathbf{Q}} a_M^\dagger a_M \hbar\omega_\mathbf{Q} g_{MM}^\mathbf{Q} \left(b_\mathbf{Q}^\dagger + b_{-\mathbf{Q}} \right) + \sum_\mathbf{Q} \hbar\omega_\mathbf{Q} \left(b_\mathbf{Q}^\dagger b_\mathbf{Q} + \frac{1}{2} \right) \qquad (2.1)$$

is denoted as Holstein Hamiltonian. [25, 30] It consists of an electronic part, a phononic part and a coupling term between electrons and phonons. The particle annihilation (creation) operators $a_M^{(\dagger)}$ are represented in real space (site $\mathbf{R}_M$) and the phonon annihilation (creation) operators $b_\mathbf{Q}^{(\dagger)}$ are represented in reciprocal space (mode $\mathbf{Q} = (\lambda, \mathbf{q})$). The electron transfer integrals ε_{MN} describe the electronic coupling between orbitals at sites $\mathbf{R}_M$ and $\mathbf{R}_N$ and give rise to finite bandwidth B and band dispersion in periodic systems. The on-site energies ε_{MM} can be set to zero according to the freedom of choosing an energy zero. The diagonal coupling constants $g_{MM}^\mathbf{Q}$ describe the changes in the on-site energies induced by a lattice distortion according to the mode $\mathbf{Q}$. A derivation of (2.1) is given in Sec. 3.1.

2.3.2 Fröhlich Polarons

Large polarons are often identified with polarons described by the Fröhlich Hamiltonian [30]

$$H = \sum_\mathbf{p} \varepsilon_\mathbf{p} a_\mathbf{p}^\dagger a_\mathbf{p} + \sum_{\mathbf{pQ}} \frac{\overline{M}}{|\mathbf{Q}|} a_{\mathbf{p}-\mathbf{Q}}^\dagger a_\mathbf{p} (b_\mathbf{Q}^\dagger + b_{-\mathbf{Q}}) + \sum_\mathbf{Q} \hbar\omega_\mathbf{Q} b_\mathbf{Q}^\dagger b_\mathbf{Q}. \qquad (2.2)$$

The difference to the Holstein Hamiltonian is the free electron energy dispersion $\varepsilon_\mathbf{p} = \frac{p^2}{2m}$ and the particular form of electron-phonon coupling which is derived from the interaction of the particles with LO phonons in the Fröhlich model. As seen from the energy dispersion, the Fröhlich Hamiltonian (2.2) assumes an isotropic system with free electrons. This is certainly not the case in crystals as a crystal implies a band structure but it might be a good approximation in the proximity of a band edge when replacing the free electron mass by an effective mass m^*. This approximation, however, is not difficult to overcome. One can replace $\varepsilon_\mathbf{p}$ by the true band energy of the crystal. The size of Fröhlich polarons is assumed to be large whereas that of Holstein polarons is assumed to be small. But this is not derived from the different expressions for the Hamiltonians (2.1) and (2.2). It is due to different treatment of the Hamiltonians like, e.g., the treatment within Holstein's *small polaron model*.

Indeed, the *Fröhlich model* is designed for large polarons since the perturbation (LO phonons) is present over a large spatial range (small phonon wavevector). This, however, is to be checked for consistency, because the larger the electron-phonon interaction the smaller the polaron. On the other hand, the *Holstein model* describes small polarons. [29] However, large polarons are also possible with the Holstein Hamiltonian. This is very obvious since both Hamiltonians differ only in the form of the electron-phonon interaction (apart from the

here irrelevant difference in the electron-energy dispersion). While the Fröhlich Hamiltonian is represented in **k**-space and the interaction term assumes a special dependence on the phonon wavevector, the Holstein Hamiltonian is written in real space and does not assume a particular form for the coupling constants g. Therefore, the Holstein Hamiltonian may be regarded as a general form of the Fröhlich Hamiltonian in a different representation.

In conclusion, it depends on the treatment but not on the formal Hamiltonian whether the description of polarons allows for small and/or large polarons. The above considerations are of particular importance to this work because the first part of this thesis is based upon the Holstein Hamiltonian but goes beyond Holstein's *small polaron model.*

2.4 Holstein Hamiltonian and Polaron Sizes

Since it is clarified that the form of a Hamiltonian does not influence the size of the polaron directly, what does? The governing parameters for the polaron size are the material parameters which enter the Hamiltonian. For the Holstein Hamiltonian, these are the transfer integrals ε_{MN}, the phonon energies $\hbar\omega_{\mathbf{Q}}$, and the electron-phonon coupling constants $g_{MM}^{\mathbf{Q}}$. It is therefore interesting to study the formation and motion of polarons as a function of these parameters. If treated correctly, one identifies different sizes of polarons and different transport mechanisms like band transport and thermally induced hopping. From the above discussion it is clear that the use of the more general Holstein Hamiltonian (2.1) is more appropriate for the general description of polarons.

An extended version of (2.1) should also be presented here. It additionally includes the non-local electron-phonon interaction $g_{MN}^{\mathbf{Q}}$ (with $M \neq N$) and is known as Holstein-Peierls Hamiltonian

$$H = \sum_{MN} a_M^\dagger \left[\varepsilon_{MN} + \sum_{\mathbf{Q}} \hbar\omega_{\mathbf{Q}} g_{MN}^{\mathbf{Q}} \left(b_{\mathbf{Q}}^\dagger + b_{-\mathbf{Q}} \right) \right] a_N + \sum_{\mathbf{Q}} \hbar\omega_{\mathbf{Q}} \left(b_{\mathbf{Q}}^\dagger b_{\mathbf{Q}} + \frac{1}{2} \right). \qquad (2.3)$$

The Holstein-Peierls Hamiltonian is an extension to both the Holstein Hamiltonian and the Fröhlich Hamiltonian.

2.4.1 Large Polarons

In the limiting case of vanishing electron-phonon interaction $g \to 0$ the Hamiltonian (2.3) reduces to non-interacting particles and phonons. In this trivial case the particles are delocalized Bloch particles (waves) which can be described by a tight-binding band structure. The motion of these bare (undressed) particles in the crystal can be characterized by an effective mass derived from the band structure at the band edge or the band velocity.

Switching on the interaction with the vibrational degrees of freedom, the bare particles get dressed by phonons and become quasiparticles called polarons. The dressing can be rationalized with an increased effective mass, i.e., the charge carriers have to carry the phonon cloud as well which always accompanies the carrier. This effective mass m^* is already increased for zero temperature because of zero point vibrational effects. With rising temperature one has an even stronger effect since much more phonons are available that couple to the particle with a certain strength g. From the simple Drude formula [52]

$$\mu = \frac{\tau e_0}{m^*} \tag{2.4}$$

it is clear that an increasing effective mass hampers the charge transport. Assuming that the coupling is not too high and that the system has high purity and crystallinity one can retain the picture of band transport with a slightly increased mass (heavy electrons), or in other words with a slightly reduced bandwidth. This polaronic effect is known as band narrowing. A smaller bandwidth reduces the size of the charge carrier as well. The delocalized Bloch particle becomes a large polaron for small electron-phonon coupling.

2.4.2 Small Polarons

With larger values for the electron-phonon interaction g the band narrowing is stronger which has also a strong impact on the localization and on the transport mechanism. The mean free path reduces. In particular for the naphthalene case, it can be estimated that the mean free path of the charge carriers for temperatures above 150 K is only about one lattice constant. [23] Therefore the concept of band transport is no longer valid for such localized states as also seen in the experiments, where the mobility along c^* direction in ultrapure naphthalene crystals is constant between 100 K and 300 K (see Fig. 2.1). This is a striking discrepancy between the experimentally measured mobilities on the one hand and the picture of polarons as heavy electrons moving in a polaron band on the other. The reason for this is that coherent band transport is not the only contribution to the currents in the measurements.

This gets obvious for strong electron-phonon interaction which implies strong phonon scattering of the carriers. The reduced mean free path of the carriers and the strong coupling gives rise to thermally activated carrier transport which is characterized by increasing mobility with increasing temperature T. This thermal activation is often assumed to follow the Boltzmann law according to $e^{-\frac{E_p}{kT}}$, where E_p is the polaron binding energy (see Marcus theory [46, 47]). Here it is studied if such a temperature dependence holds also for low and medium temperatures.

Chapter 3

Theory I. Polarons

3.1 Derivation of the Hamiltonian

The starting point for the modeling is a Bloch-Hamiltonian of non-interacting Fermions[1] in second quantization which is given in a site representation as

$$H_f = \sum_{M,N} \varepsilon_{MN} a_M^\dagger a_N, \tag{3.1}$$

where the quantities ε_{MN} are the matrix elements of the electronic coupling between states M and N. For the representation of H_f in Eq. (3.1), a basis set is chosen which is derived from localized states $\Phi_M(\mathbf{x})$. In the case of one site per unit cell these states may be identified with Wannier functions [52] located at position $\mathbf{R}_M$, i.e. $\Phi_M(\mathbf{x}) = \Phi(\mathbf{x} - \mathbf{R}_M)$. As seen in a later section, these functions have close similarity to molecular orbitals, the position of which are defined as the center of gravity of the orbitals. $\mathbf{R}_M$ typically corresponds to lattice vectors or if there are more than one molecules per unit cell also to fractional lattice vectors. In this case one may also keep the picture of localized molecular orbitals as sites in mind.

In order to keep the derivation within reasonable complexity one assumes only one orbital per molecule. The index M can then also be used to numerate the molecules. The elements of the matrix ε are defined as

$$\varepsilon_{MN} = \int d^3\mathbf{x} \Phi_M^*(\mathbf{x}) \left(-\frac{\hbar^2}{2m} \Delta_\mathbf{x} + V_{eff}(\mathbf{x}) \right) \Phi_N(\mathbf{x}). \tag{3.2}$$

Thereby, the crystal Hamiltonian H_{cryst} in the parenthesis consists of the kinetic energy and an effective potential $V_{eff}(\mathbf{x})$. The effect of the electron-electron interaction such as Hartree and exchange and correlation terms are effectively taken into account in the potential $V_{eff}(\mathbf{x})$. The single particle wavefunctions and the effective potential depend on the geometry of the system.

---

[1]Explicit electron-electron interaction is not considered here since it is not the scope of the present work.

In general, the matrix ε is not diagonal since the overlap of the wavefunctions at adjacent sites gives rise to off-diagonal elements as well. This overlap is known as electronic coupling, and the corresponding off-diagonal matrix elements $(M \neq N)$ are denoted electron transfer integrals. Eq. (3.2) serves also for the definition of the so-called on-site energies which are the diagonal elements $(M = N)$.

The transfer integrals depend parametrically on the position of each atom $\mathbf{R}_{ks}$, where k indicates the unit cell $(k = 1, \ldots, N_\Omega)$ and s runs over the atomic basis with $\mathbf{R}_{ks} = \mathbf{R}_k + \tau_s$ giving the position of the atom (k, s).[2] This is formally written as $V_{eff}(\mathbf{x}; \{\mathbf{R}_{ks}\})$.[3] One can determine the material parameters ε_{MN} at a given set of atom positions $\{\mathbf{R}_{ks}\}$ by means of *ab initio* methods and obtain the fermionic Hamiltonian $H_f = \sum_{M,N} \varepsilon_{MN}(\{\mathbf{R}_{ks}\}) a_M^\dagger a_N$ with its parametric dependence on the geometry. In crystalline structures, where $\{\mathbf{R}_k\}$ underly a certain translational symmetry, $\varepsilon_{MN}(\{\mathbf{R}_{ks}^0\})$ implies the band structure at the equilibrium coordinates given by $\{\mathbf{R}_{ks}^0\}$.

The changes in the transfer integrals with respect to the nuclear positions can be expanded in a Taylor series about the equilibrium positions. One can anticipate fast convergence and write

$$
\begin{aligned}
H_f &= \sum_{M,N} \left[\varepsilon_{MN}(\{\mathbf{R}_{ks}^0\}) + \sum_{ks} (\mathbf{R}_{ks} - \mathbf{R}_{ks}^0) \nabla_{\mathbf{R}_{ks}} \varepsilon_{MN}(\{\mathbf{R}_{ks}\}) \Big|_{\mathbf{R}_{ks} = \mathbf{R}_{ks}^0} \right] a_M^\dagger a_N \\
&\equiv \sum_{M,N} \left[\varepsilon_{MN}^0 + \varepsilon_{MN}^1 \right] a_M^\dagger a_N.
\end{aligned}
\tag{3.3}
$$

Thereby, the first order changes are written as

$$
\varepsilon_{MN}^1 = \sum_{ks} \mathbf{u}_{ks} \mathbf{C}_{MN}^{ks},
\tag{3.4}
$$

where the displacement coordinate $\mathbf{u}_{ks} = \mathbf{R}_{ks} - \mathbf{R}_{ks}^0$ and the definition

$$
\mathbf{C}_{MN}^{ks} = \nabla_{\mathbf{R}_{ks}} \int d^3\mathbf{x} \, \Phi_M^*(\mathbf{x}) H_{cryst}(\mathbf{x}; \{\mathbf{R}\}) \Phi_N(\mathbf{x})
\tag{3.5}
$$

have been introduced. In the case of crystals one can further introduce a mode expansion for the displacement coordinate with mode index λ and wavevector $\mathbf{q}$

$$
\mathbf{u}_{ks} = \frac{1}{\sqrt{M_s}} \sum_{\mathbf{q}\lambda} X_\lambda(\mathbf{q}) e^{i\mathbf{q}\mathbf{R}_k} \mathbf{e}_s^\lambda(\mathbf{q}),
\tag{3.6}
$$

where $\mathbf{e}_s^\lambda(\mathbf{q})$ is identified with the polarization vector of the mode λ of atom s. Hereby, X_λ is

---

[2]The vectors $\mathbf{R}_{ks}$ only coincide with the $\mathbf{R}_M$ if one uses atomic orbitals. In general the number of atoms is larger than the number of orbitals.

[3]Since in this work the transfer integrals ε_{MN} will not be computed according to Eq. (3.2), the actual shapes of $V_{eff}(\mathbf{x})$ and $\Phi_N(\mathbf{x})$ are not specified.

the normal mode coordinate and M_s denotes the mass of the atom s. The back transformation is given (with the number of unit cells N_Ω) by

$$X_\lambda(\mathbf{q}) = \frac{1}{N_\Omega} \sum_{ks} \sqrt{M_s} \mathbf{u}_{ks} e^{-i\mathbf{q}\mathbf{R}_k} \mathbf{e}_s^{\lambda*}(\mathbf{q}), \tag{3.7}$$

which can be verified using the norm of $\mathbf{e}_s^\lambda(\mathbf{q})$. The polarization vectors are eigenvectors of the dynamical matrix and fulfill the relation

$$\mathbf{e}_s^{\lambda*}(\mathbf{q}) = \mathbf{e}_s^\lambda(-\mathbf{q}) \tag{3.8}$$

which also implies that

$$X_\lambda(\mathbf{q}) = X_\lambda^*(-\mathbf{q}). \tag{3.9}$$

It is immediately obvious that for $\mathbf{q} = 0$ the polarization vectors and the normal mode coordinates X are real. Some general symmetries for the matrix elements $\mathbf{C}_{MN}^{ks}$ are

$$\left(\mathbf{C}_{MN}^{ks}\right)^* = \mathbf{C}_{NM}^{ks}$$
$$\mathbf{C}_{M+i\ N+i}^{k+i\ s} = \mathbf{C}_{MN}^{ks}, \tag{3.10}$$

the latter of which represents the translational symmetry. For real wavefunctions the quantities $\mathbf{C}_{MN}^{ks}$ become real and symmetric.

In order to derive the Holstein-Peierls Hamiltonian (2.3), one uses a mixed representation with phonons being developed into normal modes $(\lambda, \mathbf{q})$ and electrons being represented in real space (M, N). Annihilation and creation operators for the phonons are introduced through the quantization of the normal mode coordinate

$$X_\lambda(\mathbf{q}) = \left(\frac{\hbar}{2\omega_\lambda(\mathbf{q})N_\Omega}\right)^{1/2} \left[b_\lambda^\dagger(\mathbf{q}) + b_\lambda(-\mathbf{q})\right]. \tag{3.11}$$

Inserting Eqs. (3.6) and (3.11) into Eq. (3.4), one obtains

$$\varepsilon_{MN}^1 = \sum_{\mathbf{q}\lambda} \hbar\omega_\lambda(\mathbf{q})g_{MN}^\lambda(\mathbf{q}) \left[b_\lambda^\dagger(\mathbf{q}) + b_\lambda(-\mathbf{q})\right]. \tag{3.12}$$

Here, the electron-phonon coupling constants $g_{MN}^\lambda(\mathbf{q})$ are introduced as

$$g_{MN}^\lambda(\mathbf{q}) = \frac{1}{\sqrt{2\omega_\lambda^3(\mathbf{q})\hbar}} \sum_{ks} e^{i\mathbf{q}\mathbf{R}_k} \frac{1}{\sqrt{GM_s}} \mathbf{C}_{MN}^{ks} \mathbf{e}_s^\lambda(\mathbf{q}), \tag{3.13}$$

which fulfill certain symmetries that originate from the symmetries in (3.8) and (3.10)

$$g_{M\,N}^{\lambda}(\mathbf{q}) = \left[g_{N\,M}^{\lambda}(-\mathbf{q})\right]^{*}$$
$$g_{M+i\,N+i}^{\lambda}(\mathbf{q}) = e^{i\mathbf{q}\mathbf{R}_i}g_{MN}^{\lambda}(\mathbf{q}). \tag{3.14}$$

These symmetries also ensure the hermiticity of ε_{MN}^{1} and, hence, the Hamiltonian H_f from Eq. (3.3). In the case of real wavefunctions, the first line in Eq. (3.14) reduces to

$$g_{MN}^{\lambda}(\mathbf{q}) = g_{NM}^{\lambda}(\mathbf{q}). \tag{3.15}$$

Collecting the results from Eqs. (3.3) and (3.12) the fermionic Hamiltonian reads

$$H_f = \sum_{MN} a_M^{\dagger} \left[\varepsilon_{MN}^0 + \sum_{\mathbf{q}\lambda} \hbar\omega_{\lambda}(\mathbf{q})g_{MN}^{\lambda}(\mathbf{q})\left[b_{\lambda}^{\dagger}(\mathbf{q}) + b_{\lambda}(-\mathbf{q})\right]\right] a_N. \tag{3.16}$$

In the following, an index $\mathbf{Q} \equiv (\mathbf{q},\lambda)$ is defined as a short hand notation, and the total Hamiltonian H, which constitutes of H_f supplemented by a pure phononic part $H_{ph} = \sum_{\mathbf{Q}} \hbar\omega_{\mathbf{Q}}\left(b_{\mathbf{Q}}^{\dagger}b_{\mathbf{Q}} + \frac{1}{2}\right)$ which describes the elastic energy of the strain field $\mathbf{u}_{ks}$, becomes

$$H = H_{el} + H_{el-ph} + H_{ph}$$
$$= \sum_{MN} a_M^{\dagger} \left[\varepsilon_{MN} + \sum_{\mathbf{Q}} \hbar\omega_{\mathbf{Q}}g_{MN}^{\mathbf{Q}}\left(b_{\mathbf{Q}}^{\dagger} + b_{-\mathbf{Q}}\right)\right] a_N + \sum_{\mathbf{Q}} \hbar\omega_{\mathbf{Q}}\left(b_{\mathbf{Q}}^{\dagger}b_{\mathbf{Q}} + \frac{1}{2}\right). \tag{3.17}$$

For convenience the superscript 0 at the transfer integrals ε_{MN}^0, which denotes the electronic coupling for the ground state geometry, has been dropped. This Hamiltonian is known as Holstein-Peierls Hamiltonian (see Eq. (2.3)). It includes local electron-phonon coupling $g_{MM}^{\mathbf{Q}}$ according to the Holstein Hamiltonian (see Eq. (2.1)) and additional non-local coupling of electrons and phonons $g_{MN}^{\mathbf{Q}}$.

For the computation of the material parameters $g_{MN}^{\mathbf{Q}}$, Eq. (3.13) can be used in principle. However, one can write the coupling constants in a different way

$$g_{MN}^{\lambda}(\mathbf{q}) = \frac{\partial \varepsilon_{MN}}{\partial X_{\lambda}(\mathbf{q})} \frac{1}{\sqrt{2\omega_{\lambda}^3(\mathbf{q})\hbar N_{\Omega}}}, \tag{3.18}$$

which suggests a direct access to these parameters from *ab initio* computations since the transfer integrals ε_{MN} can be computed depending on the actual nuclear positions, as mentioned on page 14. Therefore the representation based on the normal mode coordinate of the phonons in Eq. (3.18) allows for a direct determination from an accordingly deformed lattice.

3.2 Polaron Transformation

In general, one is interested in finding the eigenenergies and eigenfunctions of the Holstein-Peierls Hamiltonian (3.17), which is a highly non-trivial problem. The complexity arises from the coupling part ($\propto g$) which prevents one from diagonalizing H. [30] However, an approximate diagonalization can be carried out which is described in the following. Hereby, I follow the derivation in Ref. [25].

One performs a canonical transformation

$$\widetilde{H} = e^S H e^{S^\dagger} \tag{3.19}$$

into the polaron picture, where

$$S = \sum_{MN} C_{MN} a_M^\dagger a_N \tag{3.20}$$

and

$$C_{MN} = \sum_{\mathbf{Q}} g_{MN}^{\mathbf{Q}} \left(b_{\mathbf{Q}}^\dagger - b_{-\mathbf{Q}} \right). \tag{3.21}$$

This transformation is also denoted as Lang-Firsov transformation [53]. In accordance to the discussion in Sec. 2.4, the transformation (3.19) is called polaron transformation throughout this thesis. The relation

$$1 = e^{-S} e^S = e^{S^\dagger} e^S \tag{3.22}$$

proves that the polaron transformation is a unitary transformation and the eigenvalues of H and $\widetilde{H}$ are the same. The transformation directly acts on the operators for electrons and phonons in H and the polaron Hamiltonian (3.19) reads

$$\widetilde{H} = \sum_{MN} \widetilde{a}_M^\dagger \left[\varepsilon_{MN} + \sum_{\mathbf{Q}} \hbar \omega_{\mathbf{Q}} g_{MN}^{\mathbf{Q}} \left(\widetilde{b}_{\mathbf{Q}}^\dagger + \widetilde{b}_{-\mathbf{Q}} \right) \right] \widetilde{a}_N + \sum_{\mathbf{Q}} \hbar \omega_{\mathbf{Q}} \left[\widetilde{b}_{\mathbf{Q}}^\dagger \widetilde{b}_{\mathbf{Q}} + \frac{1}{2} \right]. \tag{3.23}$$

The polaron Hamiltonian has the same form as H, however, the operators have changed according to

$$\begin{aligned}
a_M^\dagger \to \widetilde{a}_M^\dagger = e^S a_M^\dagger e^{S^\dagger}, \quad & a_N \to \widetilde{a}_N = e^S a_N e^{S^\dagger}, \\
b_Q^\dagger \to \widetilde{b}_Q^\dagger = e^S b_Q^\dagger e^{S^\dagger}, \quad & b_Q \to \widetilde{b}_Q = e^S b_Q e^{S^\dagger}.
\end{aligned} \tag{3.24}$$

The operators $\widetilde{a}^\dagger$ and $\widetilde{a}$ are polaron operators which, according to Eq. (3.24), are functions of basic phonon and electron operators.

In order to evaluate $\widetilde{H}$ in (3.23) one uses the Baker-Campbell-Hausdorff formula, which

is written here for an arbitrary quantity X:

$$\widetilde{X} \equiv e^S X e^{-S} = X + \frac{1}{1!}[S, X] + \frac{1}{2!}[S, [S, X]] + ... \equiv \sum_{m=0}^{\infty} \frac{1}{m!}[S, X]_m. \tag{3.25}$$

Below, I employ a matrix notation with vectors a (components a_M), matrices C (matrix elements C_{MN}), and a matrix-vector product Ca according to $\sum_N C_{MN} a_N$. It can be shown by mathematical induction that

$$
\begin{aligned}
[S, a]_m &= (-C)^m a & \left[S, a^\dagger\right]_m &= a^\dagger C^m \\
[S, b_{\mathbf{Q}}]_m &= a^\dagger [C, b_{\mathbf{Q}}]_m a & \left[S, b_{\mathbf{Q}}^\dagger\right]_m &= a^\dagger \left[C, b_{\mathbf{Q}}^\dagger\right]_m a
\end{aligned}
\tag{3.26}
$$

which results in expressions for the transformed operators

$$
\begin{aligned}
\widetilde{a} &= e^{-C} a, & \widetilde{a}^\dagger &= a^\dagger e^C, \\
\widetilde{b}_{\mathbf{Q}} &= b_{\mathbf{Q}} + a^\dagger D_{\mathbf{Q}} a, & \widetilde{b}_{\mathbf{Q}}^\dagger &= b_{\mathbf{Q}}^\dagger + a^\dagger D_{\mathbf{Q}}^\dagger a,
\end{aligned}
\tag{3.27}
$$

with

$$D_{\mathbf{Q}} = e^C b_{\mathbf{Q}} e^{-C} - b_{\mathbf{Q}}. \tag{3.28}$$

Note that e^C denotes the matrix exponential $\sum_{m=0}^{\infty} \frac{C^m}{m!}$, where C^m is a matrix product according to the notation used. The form of the polaron operators $\widetilde{a}^\dagger$ and $\widetilde{a}$ in (3.27) represent formally the relation between the bare particles and the polarons through the polarization, which is expressed in the connection of the electron operators $a^\dagger$ and a and the phonon operators via C. This connection essentially models the dressing aspect of the polaron concept as discussed in Chap. 2. The non-perturbative character of the inclusion of the electron-phonon interaction is evident from the factors e^{-C} and e^C, which takes all orders of the coupling constants g into account. By inserting the equations (3.27) into the expression (3.23) for $\widetilde{H}$, one can carry the transformation matrices over to the matrix elements, where the definitions

$$
\begin{aligned}
\hat{g}^{\mathbf{Q}} &= e^C g^{\mathbf{Q}} e^{-C}, \\
\hat{\varepsilon} &= e^C \varepsilon e^{-C},
\end{aligned}
\tag{3.29}
$$

are used. One proceeds with the assumption $\left[g^{\mathbf{Q}'}, g^{\mathbf{Q}}\right] = 0$, which is exact for purely local electron-phonon coupling but which constitutes an approximation if additional nonlocal contributions are considered. This approximation allows to proceed in an analytical way. [25] It implies that

$$D_{\mathbf{Q}} = -g^{\mathbf{Q}}, \qquad D_{\mathbf{Q}}^\dagger = -g^{-\mathbf{Q}}. \tag{3.30}$$

As a result, one obtains

$$\widetilde{H} = a^\dagger \hat{\varepsilon} a + \sum_{\mathbf{Q}} \hbar \omega_{\mathbf{Q}} \left(b_{\mathbf{Q}}^\dagger b_{\mathbf{Q}} + \frac{1}{2} \right) - \sum_{\mathbf{Q}} \hbar \omega_{\mathbf{Q}} \left(a^\dagger \hat{g}^{\mathbf{Q}} a \right) \left(a^\dagger \hat{g}^{-\mathbf{Q}} a \right). \tag{3.31}$$

In consistency to the neglect of electron-electron interaction from the very beginning, the replacement $a_M^\dagger a_N a_R^\dagger a_S \to a_M^\dagger a_S \delta_{NR}$ is made which directly leads to the final expression for the polaron Hamiltonian

$$\widetilde{H} = a^\dagger \hat{E} a + \sum_{\mathbf{Q}} \hbar \omega_{\mathbf{Q}} \left[b_{\mathbf{Q}}^\dagger b_{\mathbf{Q}} + \frac{1}{2} \right], \tag{3.32}$$

where $\hat{E} \equiv e^C E e^{-C}$ is a short hand notation for $\hat{E}_{MN} = \sum_{RS} (e^C)_{MR} E_{RS} (e^{-C})_{SN}$ using the definition

$$E_{MN} = \varepsilon_{MN} - \Delta_{MN} \tag{3.33}$$

of the reduced transfer integrals with the so-called polaron shift

$$\Delta_{MN} = \sum_{\mathbf{Q}} \sum_{K} \hbar \omega_{\mathbf{Q}} g_{MK}^{\mathbf{Q}} g_{KN}^{-\mathbf{Q}}. \tag{3.34}$$

3.3 Polaronic Eigenvalues

The influence of the lattice vibrations on the original Hamiltonian H in Eq. (3.17) is obvious from the appearance of the phonon operators b and $b^\dagger$. This translates to the transformed Hamiltonian $\widetilde{H}$, since the quantity $\hat{E}$ still contains phonon operators. If one is interested in the modifications of the electronic energies ε_{MN} which are induced by the vibrations, one may compute the eigenenergies of the polarons by tracing up $\widetilde{H}$ over the phononic degrees of freedom

$$\langle \widetilde{H} \rangle_{Ph} = a^\dagger \langle \hat{E} \rangle_{Ph} a + \sum_{\mathbf{Q}} \hbar \omega_{\mathbf{Q}} \left[\langle b_{\mathbf{Q}}^\dagger b_{\mathbf{Q}} \rangle_{Ph} + \frac{1}{2} \right]. \tag{3.35}$$

It is clear that a meaningful result for such an influence of the phonons on ε_{MN} cannot be obtained with the original Hamiltonian H because the linear electron-phonon interaction g would vanish after the trace. With the Hamiltonian $\widetilde{H}$, however, this is possible and the result includes all orders of the coupling constants g.

The calculation of the expectation value of the operator $\hat{E}$ in phonon space can again be performed by means of the Baker-Campbell-Hausdorff theorem (3.25). One finally obtains

[25]

$$\langle \widetilde{E} \rangle_{Ph} = \sum_{m=0}^{\infty} \left(-\frac{1}{2} \right)^m \frac{1}{m!} \sum_{\mathbf{Q}_m \cdots \mathbf{Q}_1} (1 + 2N_{\mathbf{Q}_1}) \cdots (1 + 2N_{\mathbf{Q}_m}) \times$$
$$\times \left[g^{\mathbf{Q}_1}, \left[g^{-\mathbf{Q}_1}, \ldots, \left[g^{\mathbf{Q}_m}, \left[g^{-\mathbf{Q}_m}, E \right] \right] \cdots \right] \right], \tag{3.36}$$

where the phonon occupation number $N_{\mathbf{Q}} = \left(e^{\frac{\hbar \omega_{\mathbf{Q}}}{k_B T}} - 1 \right)^{-1}$ is defined according to the Bose-Einstein statistics. This is where the temperature enters the formalism and allows for the description of the T-dependence of the bandwidth and the effective mass.

The expression (3.36) could be evaluated exactly if only local electron-phonon interaction was included. In the present case taking additional non-local coupling into account, the complicated commutators can in principle be evaluated numerically until convergence. For simplicity, however, only the largest terms from the commutators are included here to obtain an analytical expression, i.e., one assumes that $\langle \hat{E}_{MM} \rangle_{Ph}$ depends only on E_{KK}, and $\langle \hat{E}_{MN} \rangle_{Ph}$ depends on E_{KK} and E_{MN}. It follows that the off-diagonal matrix elements $\langle \hat{E}_{MN} \rangle$ can be collected [44] to an exponential sum resulting in

$$\widetilde{\varepsilon}_{MN} \equiv \langle \hat{E}_{MN} \rangle_{Ph} = E_{MN} \exp \left[-\frac{1}{2} \sum_{\mathbf{Q}} (1 + 2N_{\mathbf{Q}}) \, G_{MN}^{\mathbf{Q}} \right] \tag{3.37}$$

with the effective electron-phonon coupling

$$G_{MN}^{\mathbf{Q}} = |g_{MM}^{\mathbf{Q}} - g_{NN}^{\mathbf{Q}}|^2 + \sum_{K \neq M} |g_{MK}^{\mathbf{Q}}|^2 + \sum_{K \neq N} |g_{KN}^{\mathbf{Q}}|^2. \tag{3.38}$$

For the diagonal elements one simply obtains $\langle \hat{E}_{MM} \rangle_{Ph} = E_{MM}$.

Before I come to the discussion of the above results in the next section, the respective result from Eq. (3.36) for purely local electron-phonon coupling $g_{MN}^{\mathbf{Q}} \to \delta_{MN} g_{MM}^{\mathbf{Q}}$ is given. In this case the off-diagonal elements of the polaron shift Δ_{MN} vanish and the quantities E_{MN} reduce to ε_{MN}. The effective coupling $G_{MN}^{\mathbf{Q}}$ is reduced to the first term in Eq. (3.38) and one obtains

$$\widetilde{\varepsilon}_{MN} = \varepsilon_{MN} \exp \left[-\frac{1}{2} \sum_{\mathbf{Q}} (1 + 2N_{\mathbf{Q}}) \, |g_{MM}^{\mathbf{Q}} - g_{NN}^{\mathbf{Q}}|^2 \right]. \tag{3.39}$$

3.4   Discussion

A brief discussion is included to explain what makes the polaronic energies being different from electronic energies. First, the bare quantities ε_{MN} are shifted by Δ_{MN} according to

Eq. (3.33). For the on-site energies ε_{MM}, the polaron shift Δ_{MM} is positive and may be interpreted as polaron binding energy E_p. The reason for this shift is that the linear coupling of the lattice and electronic degrees of freedom leads to a lowering of the electronic levels by a quadratic shift in the electron-phonon coupling constants g. In terms of physics, the coupling leads to an additional binding energy, i.e. an energy gain due to the binding of the charge carriers to the phonons. The modifications of the off-diagonal elements ε_{MN} is interpreted as a deformation of the bandstructure. Second, the shifted off-diagonal quantities E_{MN} are additionally renormalized by the exponential factor $e^{-\frac{1}{2}\sum_{\mathbf{Q}}(1+2N_{\mathbf{Q}})G_{MN}^{\mathbf{Q}}}$ according to Eq. (3.37). From Eq. (3.38) it follows that the exponent is always negative since the phonon numbers $N_{\mathbf{Q}}$ and effective coupling constants $G^{\mathbf{Q}}$ are always positive which results in a reduction of the electronic coupling matrix elements. Therefore the bandwidth, which is derived from the electronic coupling, is also reduced. This effect is known as band narrowing. The polaron bandwidth is therefore smaller than the electron bandwidth.

Equation (3.38) shows that there are two contributions to the effective coupling constant $G_{MN}^{\mathbf{Q}}$, a first one arising from local electron-phonon coupling and a second one from non-local electron-phonon coupling. According to the Taylor series expansion in Eq. (3.3) and its relation to the coupling constants g in Eq. (3.12), the local contribution $|g_{MM}^{\mathbf{Q}} - g_{NN}^{\mathbf{Q}}|^2$ describes the dynamical mismatch of the changes in the electronic on-site energies expressed by $\varepsilon_{MM}^1 - \varepsilon_{NN}^1$,[4] which is induced by a lattice distortion due to the phonon $\mathbf{Q}$. This contribution is different from zero only if the on-site energies are shifted differently. There would be no influence on the transfer integral ε_{MN} in the case of an equal shift of both on-site energies ($\varepsilon_{MM}^1 = \varepsilon_{NN}^1$). As a consequence of this dynamical mismatch of the on-site energies, the original transfer integral ε_{MN} or the transfer rate $\frac{\varepsilon_{MN}}{\hbar}$ is reduced. The second contribution, $\sum_{K \neq M} |g_{MK}^{\mathbf{Q}}|^2 + \sum_{K \neq N} |g_{KN}^{\mathbf{Q}}|^2$, from nonlocal electron-phonon coupling arises from the changes in the transfer integrals ε_{KN}^1 and ε_{MK}^1 to all neighbors.

It is observed that the band narrowing already occurs for zero temperature due to zero point vibrational effects. For $T = 0$ K no phonons are present ($N_{\mathbf{Q}} = 0$) and Eq. (3.37) reduces to

$$\langle \hat{E}_{MN} \rangle_{Ph} = E_{MN} \exp\left[-\frac{1}{2} \sum_{\mathbf{Q}} G_{MN}^{\mathbf{Q}} \right]. \tag{3.40}$$

For elevated T the dressing of the charged particle by phonons increases ($N_{\mathbf{Q}} \neq 0$) and results in a temperature-driven bandwidth reduction.

Using the concept of an effective mass [52], the discussed band narrowing is equal to a mass enhancement with the inverse renormalization factor. The increased polaron mass may be interpreted as an enhancement due to the coupling to the motion of the heavy atoms

---

[4]The quantities ε_{MM}^1 were introduced in Eq. (3.3).

(lattice polarization).

3.5   Numerical Treatment

After the discussion of the general features, I specify the above formulas to a case that allows a straightforward numerical evaluation of Eq. (3.37). In order to evaluate Eq. (3.37), the **q**-dependence of the electron-phonon interaction as well as the dispersion of the phonon frequency $\omega_{\mathbf{Q}}$ is required. However, it would be a too formidable task to determine all the parameters along with their full **q** dependence. A simplified approach towards evaluation of Eq. (3.37) is the replacement of the general phonon dispersion in $g^{\mathbf{Q}}$ by a standard relation [25, 32, 33]

$$g_{MN}^{\mathbf{Q}} \rightarrow \frac{1}{2} \frac{g_{MN}^{\lambda}}{\sqrt{N_\Omega}} \left(e^{i\mathbf{q}\mathbf{R}_M} + e^{i\mathbf{q}\mathbf{R}_N} \right), \tag{3.41}$$

and set $\omega_{\mathbf{Q}} = \omega_\lambda$, thus neglecting the energy dispersion accordingly, which also results in $N_{\mathbf{Q}} = N_\lambda$. Note that there is a connection between the new quantities g_{MN}^{λ} and the coupling constants $g_{MN}^{\lambda}(\mathbf{q})$ defined in Eq. (3.18) through $g_{MN}^{\lambda}(0) = \frac{1}{\sqrt{N_\Omega}} g_{MN}^{\lambda}$, which establishes the relation to the coupling constants at the Γ point. This will be of importance later on when these quantities are calculated within an *ab initio* framework.

By replacing (3.41) in (3.38), the sum over the phonon wavevector in (3.37) can be carried out. With the definition

$$G_{\lambda MN} = \sum_{\mathbf{q}} G_{MN}^{\mathbf{Q}}, \tag{3.42}$$

one obtains

$$G_\lambda \equiv G_{\lambda MN} = 2 \left(g_{MM}^{\lambda} \right)^2 + \sum_{K \neq M} \left(g_{MK}^{\lambda} \right)^2, \tag{3.43}$$

where the spatial indices at $G_{\lambda MN}$ have been dropped since it is independent of spatial coordinates (due to the sum over all neighbors K and the assumption of equal on-site coupling constants $g_{MM}^{\lambda} = g_{NN}^{\lambda}$). Equation (3.37) reads finally

$$\widetilde{\varepsilon}_{MN} = E_{MN} e^{-\frac{1}{2} \sum_\lambda (1+2N_\lambda) G_\lambda}. \tag{3.44}$$

In the case of purely local electron-phonon coupling as present in the Holstein Hamiltonian, Eq. (3.44) reads

$$\widetilde{\varepsilon}_{MN} = \varepsilon_{MN} e^{-\sum_\lambda (1+2N_\lambda)(g_{MM}^{\lambda})^2}. \tag{3.45}$$

Chapter 4

Theory II. Charge Transport

4.1 Basic Derivation

The polaron concept as introduced in Chap. 2 is extensively used to describe transport properties in organic crystals which highlights its importance for studies of the carrier mobilities here as well. Thereby, the size is an important property to characterize polarons in semiconducting OMCs since Holstein's small-polaron theory, or extensions inspired by it, are valid for small polarons only. [29] More precisely, they are restricted to the narrow-band limit where the electronic coupling between neighboring molecules is sufficiently small and the electron-phonon coupling plays a dominant role. In the last chapter I introduced the formal description of polarons and derived basic features like polaron binding and band narrowing. In this chapter, a novel theory for the polaron mobility is derived, which is qualitatively different to the theories based on Holstein's small-polaron model because it describes polarons of arbitrary sizes. Consequently, the temperature range for its validity is also extended with respect to Holstein's description (see Fig. 1.1).

4.1.1 Kubo Formula

The conductivity σ of a system exposed to an electric field $\mathbf{E}$ is defined as its current response $\mathbf{J}$ according to[1]

$$J_\alpha(\omega) = \sum_\beta \sigma_{\alpha\beta}(\omega) E_\beta(\omega). \tag{4.1}$$

Within the Kubo formalism of linear response theory the dc-conductivity at a given temperature T is obtained in the zero-frequency limit

$$\sigma_{\alpha\beta}^{dc} = \frac{1}{2k_B T} \lim_{\omega \to 0} \int_{-\infty}^{\infty} dt \, e^{i\omega t} \langle j_\alpha(t) j_\beta(0) \rangle_H \tag{4.2}$$

---

[1]Greek indices denote Cartesian components.

with k_B being Boltzmann's constant. [30] A material specific quantity that is directly accessible in time-of-flight experiments [22, 54, 55] is the charge carrier mobility $\mu = \frac{\sigma}{e_0 N_c}$, where e_0 is the elementary charge and N_c is the number of charge carriers. This quantity is an intrinsic measure for the carrier velocity at a given value of $\mathbf{E}$. Accordingly, it is usually given in units of $\frac{cm^2}{Vs}$. The Kubo formula for the dc-mobility reads

$$\mu_{\alpha\beta} = \frac{1}{N_c e_0} \frac{1}{2k_B T} \int_{-\infty}^{\infty} dt \, \langle j_\alpha(t) j_\beta(0) \rangle_H. \tag{4.3}$$

In order to evaluate Eq. (4.3), the current-current correlation function $\langle j_\alpha(t) j_\beta(0) \rangle_H$ has to be known for all times t.

The thermal average over the current-current correlation function is performed using the standard quantum-statistical average $\langle A \rangle_H = \mathrm{Tr} \left(e^{-\frac{H}{k_B T}} A \right) \Big/ \mathrm{Tr} \left(e^{-\frac{H}{k_B T}} \right)$ over the grand canonical ensemble at temperature T along with the time evolution

$$\langle j_\alpha(t) j_\beta(0) \rangle_H = \langle e^{\frac{i}{\hbar} H t} j_\alpha e^{-\frac{i}{\hbar} H t} j_\beta \rangle_H, \tag{4.4}$$

where $\mathbf{j}(0) \equiv \mathbf{j}$ is the current operator at $t = 0$, and the Hamiltonian of the system is assumed to be the Holstein Hamiltonian (2.1). The derivation is performed neglecting the nonlocal electron-phonon interaction as present in the Holstein-Peierls Hamiltonian (2.3) for simplicity. With the Hamiltonian (2.1) and the polarization operator $\mathbf{P} = e_0 \sum_M \mathbf{R}_M a_M^\dagger a_M$ ($\mathbf{R}_M$ is the position vector pointing to site M as discussed in the beginning of Sec. 3.1), the current operator in (4.4) is given as

$$j_\alpha = \frac{dP_\alpha}{dt} = \frac{1}{i\hbar} [P_\alpha, H] \tag{4.5}$$

and reads

$$j_\alpha = \frac{e_0}{i\hbar} \sum_{MN} (R_{M\alpha} - R_{N\alpha}) \varepsilon_{MN} a_M^\dagger a_N. \tag{4.6}$$

In order to evaluate the correlation function (4.4) analytically, H should be diagonal. However, the Hamiltonian (2.1) cannot be diagonalized exactly [30] due to the interaction of particles and phonons as discussed in the previous chapter and, thus, inhibits a direct evaluation of the thermal average for the current-current correlation function. Consequently, one has to proceed with an approximate diagonalization of H. One idea is to find a hierarchy of energies in the spirit of perturbation theory and neglect small terms. Such a method requires *a priori* assumptions about coupling strengths and, therefore, cannot be of general validity but gives results for limiting cases, e.g., the strong-coupling regime (large g). In this case the electron-phonon interaction is assumed being stronger than the electronic coupling and the latter quantity is treated as a perturbation. Alternatively, one considers the weak coupling regime for small g. Such considerations, however, are not necessary after the polaron

transformation as will be demonstrated in the next section.

4.1.2 Polaron Transformation

In order to proceed with the evaluation of the correlation function (4.4), I perform the polaron transformation (3.19) with $S = \sum_{MQ} g^{\mathbf{Q}}_{MM} a^{\dagger}_M a_M (b^{\dagger}_{\mathbf{Q}} - b_{-\mathbf{Q}})$ to get into the polaron picture. This is analogous to Eqs. (3.19)-(3.21) but restricted to local electron-phonon coupling in consistence to the Hamiltonian H of Eq. (2.1). It results in the polaron Hamiltonian

$$\widetilde{H} = \sum_{MN} a^{\dagger}_M \hat{E}_{MN} a_N + \sum_{\mathbf{Q}} \hbar\omega_{\mathbf{Q}} \left(b^{\dagger}_{\mathbf{Q}} b_{\mathbf{Q}} + \frac{1}{2} \right), \qquad (4.7)$$

which has been discussed in Sec. 3.2. It was found that $\hat{E}_{MN} = \sum_{RS} (e^C)_{MR} E_{RS} (e^{-C})_{SN}$ still contains phonon operators through the quantities C_{MN} (cf. Eq. (3.21)) which, for purely local electron-phonon coupling reduce to diagonal elements $C_M = \sum_{\mathbf{Q}} g^{\mathbf{Q}}_{MM} \left(b^{\dagger}_{\mathbf{Q}} - b_{-\mathbf{Q}} \right)$. In this case one can further simplify $\hat{E}_{MN}$ which reads then $\hat{E}_{MN} = e^{C_M} \varepsilon_{MN} e^{-C_N}$. The polaron transformation is also made for the current operators $\widetilde{j}_{\alpha} \equiv e^S j_{\alpha} e^{S^{\dagger}}$, and with the definition $R_{MN\alpha} \equiv R_{M\alpha} - R_{N\alpha}$ one obtains

$$\widetilde{j}_{\alpha} = \frac{e_0}{i\hbar} \sum_{MN} e^{C_M} R_{MN\alpha} \varepsilon_{MN} e^{-C_N} a^{\dagger}_M a_N. \qquad (4.8)$$

While the polaron transformation does not exactly diagonalize the Holstein Hamiltonian H, because electron and phonon operators are still coupled in the first term of the transformed Hamiltonian (4.7), the two contributions in (4.7) can be regarded as a polaronic and a phononic one, which indicates a better route towards decoupling. The advantage of the separation between polarons and phonons over the original separation between electrons and phonons in H is obvious. The properties of the polarons, like their temperature dependent energy structure $\widetilde{\varepsilon}_{MN} \equiv \langle \hat{E}_{MN} \rangle$, bandwidth, mass, and size have been derived in Sec. 3.3 and discussed in Sec. 3.4. A separation between polarons (of arbitrary mass/size) and phonons in $\widetilde{H}$ is possible without being restricted to either weak-coupling or strong-coupling regime if the renormalized polaron energy structure is taken into account. Strictly speaking, I introduce the polarons as in previous work [30, 44] by replacing $\hat{E}_{MN}$ by their expectation values $\hat{E}_{MN} \to \widetilde{\varepsilon}_{MN}$ and obtain the approximate polaron Hamiltonian

$$\widetilde{H} = \sum_{MN} a^{\dagger}_M \widetilde{\varepsilon}_{MN} a_N + \sum_{\mathbf{Q}} \hbar\omega_{\mathbf{Q}} \left(b^{\dagger}_{\mathbf{Q}} b_{\mathbf{Q}} + \frac{1}{2} \right) \qquad (4.9)$$

which is used henceforth.

The great merit of the polaron transformation is seen in the identity

$$\langle j_\alpha(t) j_\beta(0) \rangle_H = \langle e^S j_\alpha(t) e^{S^\dagger} e^S j_\beta(0) e^{S^\dagger} \rangle_{\widetilde{H}} = \langle e^{\frac{i}{\hbar}\widetilde{H}t} \widetilde{j}_\alpha e^{-\frac{i}{\hbar}\widetilde{H}t} \widetilde{j}_\beta \rangle_{\widetilde{H}}. \tag{4.10}$$

because the approximate diagonalized $\widetilde{H}$, which includes the polaron effects, can be used for time evolution and thermal average instead of an approximate diagonalized H. In combination with the exact expression (4.8) for the current operators $\widetilde{\mathbf{j}}$ the approximate diagonalization of $\widetilde{H}$ on top of the polaron transformation is a very general way to account for arbitrary electron-phonon coupling strength and has been used previously. [25]

4.1.3 Time Evolution

I proceed by inserting Eq. (4.8) into Eq. (4.10) and obtain

$$\langle j_\alpha(t) j_\beta(0) \rangle_H$$
$$= \left(\frac{e_0}{i\hbar}\right)^2 \sum_{KLMN} \langle e^{i\widetilde{H}t/\hbar} e^{C_K} R_{KL\alpha}\varepsilon_{KL} e^{-C_L} a_K^\dagger a_L e^{-i\widetilde{H}t/\hbar} e^{C_M} R_{MN\beta}\varepsilon_{MN} e^{-C_N} a_M^\dagger a_N \rangle_{\widetilde{H}}. \tag{4.11}$$

The decoupling of electron and phonon operators in (4.9) has another big advantage which is the simplified evaluation of the time evolution of operators such as

$$e^{\frac{i}{\hbar}\widetilde{H}t} e^{C_K} e^{-\frac{i}{\hbar}\widetilde{H}t} = e^{C_K(t)}, \tag{4.12}$$

where $C_K(t)$ is obtained as

$$C_K(t) = \sum_{\mathbf{Q}} g_{KK}^{\mathbf{Q}} B_{\mathbf{Q}}(t), \tag{4.13}$$

and

$$B_{\mathbf{Q}}(t) = b_{\mathbf{Q}}^\dagger e^{i\omega_{\mathbf{Q}}t} - b_{-\mathbf{Q}} e^{-i\omega_{\mathbf{Q}}t} \tag{4.14}$$

is a time dependent linear combination of phonon operators. In this way, Eq. (4.11) is transformed into

$$\langle j_\alpha(t) j_\beta(0) \rangle_H$$
$$= \left(\frac{e_0}{i\hbar}\right)^2 \sum_{KLMN} \langle e^{C_K(t)} R_{KL\alpha}\varepsilon_{KL} e^{-C_L(t)} e^{i\widetilde{H}t/\hbar} a_K^\dagger a_L e^{-i\widetilde{H}t/\hbar} e^{C_M} R_{MN\beta}\varepsilon_{MN} e^{-C_N} a_M^\dagger a_N \rangle_{\widetilde{H}}. \tag{4.15}$$

The next step involves the evaluation of the time evolution of the electron operators $e^{\frac{it}{\hbar}\widetilde{H}} a_K^\dagger e^{-\frac{it}{\hbar}\widetilde{H}}$. This time evolution of the electron operators could be easily computed if the Hamiltonian $\widetilde{H}$ would be diagonal also in the operators a and $a^\dagger$, i.e., if the off-diagonal elements $\widetilde{\varepsilon}_{MN}$ would vanish. According to Eq. (3.39), this is the case for high enough

temperatures because of the narrowing of the band. In this case one could simply set

$$\widetilde{H} \to \widetilde{H}' = \sum_M \widetilde{\varepsilon}_{MM} a_M^\dagger a_M + \sum_{\mathbf{Q}} \hbar\omega_{\mathbf{Q}} \left(b_{\mathbf{Q}}^\dagger b_{\mathbf{Q}} + \frac{1}{2} \right). \tag{4.16}$$

In the general case, however, Eq. (4.16) is an approximation since the bandwidth is finite also for polarons. This amounts to the so-called narrow-band approximation (NBA) which has been used by other authors in the past. [29, 33, 44] For strong electron-phonon coupling the NBA gives good results for elevated temperatures but fails in the $T \to 0$ limit. Since the NBA is not used here, its features will be discussed in a later section in detail (see Sec. 4.3.1). In fact this approximation is not necessary and can be dropped. Alternatively, I demonstrate another route to evaluate Eq. (4.15) which avoids the narrow-band approximation. The central goal is to take the full bandwidth into account which vastly extends the validity range of the final result.

The exact diagonalization of the polaronic part of the Hamiltonian $\widetilde{H}$ from Eq. (4.9) is performed in reciprocal space. If one introduces $\mathbf{k}$-space electron creation operators $a_{\mathbf{k}}^\dagger$, one can substitute

$$a_M^\dagger = \sqrt{\frac{1}{N_\Omega}} \sum_{\mathbf{k}} e^{i\mathbf{k}\mathbf{R}_M} a_{\mathbf{k}}^\dagger, \tag{4.17}$$

where the sum runs over all wavevectors in the Brillouin zone and N_Ω is the number of unit cells. With the polaron energies in reciprocal space

$$\widetilde{\varepsilon}(\mathbf{k}) = \sum_N \widetilde{\varepsilon}_{0N} e^{-i\mathbf{k}\mathbf{R}_N} \tag{4.18}$$

it follows that the polaron Hamiltonian (4.9) becomes diagonal in this representation

$$\widetilde{H} = \sum_{\mathbf{k}} \widetilde{\varepsilon}(\mathbf{k}) a_{\mathbf{k}}^\dagger a_{\mathbf{k}} + \sum_{\mathbf{Q}} \hbar\omega_{\mathbf{Q}} \left(b_{\mathbf{Q}}^\dagger b_{\mathbf{Q}} + \frac{1}{2} \right). \tag{4.19}$$

As a consequence, the time evolution of the electron operators is then easily computed with the polaron band energy $\widetilde{\varepsilon}(\mathbf{k})$

$$e^{\frac{it}{\hbar}\widetilde{H}} a_{\mathbf{k}}^\dagger e^{-\frac{it}{\hbar}\widetilde{H}} = a_{\mathbf{k}}^\dagger e^{\frac{it}{\hbar}\widetilde{\varepsilon}(\mathbf{k})} \tag{4.20}$$

and Eq. (4.15) takes the form

$$
\begin{aligned}
\langle j_\alpha(t) j_\beta(0) \rangle_H = {} & -\left(\frac{e_0}{\hbar}\right)^2 \sum_{KLMN} \frac{1}{N_\Omega^2} \sum_{\mathbf{k}_1 \mathbf{k}_2 \mathbf{k}_3 \mathbf{k}_4} e^{i\mathbf{k}_1 \mathbf{R}_K} e^{-i\mathbf{k}_2 \mathbf{R}_L} e^{i\mathbf{k}_3 \mathbf{R}_M} e^{-i\mathbf{k}_4 \mathbf{R}_N} \\
& \times e^{\frac{it}{\hbar}\widetilde{\varepsilon}(\mathbf{k}_1)} e^{-\frac{it}{\hbar}\widetilde{\varepsilon}(\mathbf{k}_2)} \left\langle a_{\mathbf{k}_1}^\dagger a_{\mathbf{k}_2} a_{\mathbf{k}_3}^\dagger a_{\mathbf{k}_4} \right\rangle_{\widetilde{H}} \\
& \times \left\langle e^{C_K(t)} R_{KL\alpha} \varepsilon_{KL} e^{-C_L(t)} e^{C_M} R_{MN\beta} \varepsilon_{MN} e^{-C_N} \right\rangle_{\widetilde{H}}.
\end{aligned}
\tag{4.21}
$$

4.1.4   Thermal Averages

Another great advantage of the decoupling of polarons and phonons in the approximate polaron Hamiltonian $\widetilde{H}$ is that electron and phonon operators are fully separated in the correlation function (4.21). For the electron part, one can now calculate the thermal average immediately according to Wick's theorem

$$
\left\langle a_{\mathbf{k}_1}^\dagger a_{\mathbf{k}_2} a_{\mathbf{k}_3}^\dagger a_{\mathbf{k}_4} \right\rangle_{\widetilde{H}} = \delta_{\mathbf{k}_1}^{\mathbf{k}_2} \delta_{\mathbf{k}_3}^{\mathbf{k}_4} n_{\mathbf{k}_1} n_{\mathbf{k}_3} + \delta_{\mathbf{k}_1}^{\mathbf{k}_4} \delta_{\mathbf{k}_3}^{\mathbf{k}_2} n_{\mathbf{k}_1} (1 - n_{\mathbf{k}_2})
\tag{4.22}
$$

where the Fermi-Dirac distribution

$$
n_{\mathbf{k}} = \left(\exp\left[\frac{\widetilde{\varepsilon}(\mathbf{k}) - \zeta}{k_B T} \right] + 1 \right)^{-1}
\tag{4.23}
$$

with the chemical potential $\zeta = \zeta(T, N_c)$ has been introduced. Note that the polaron energies appear in $n_{\mathbf{k}}$.

The two terms on the rhs of (4.22) are not of equal importance. The n^2 term describes density correlations and usually does not contribute to the current. In any case it is much smaller than the $n(1 - n)$ term if one considers low concentration as in the present work. If the n^2 term is neglected henceforth one obtains

$$
\begin{aligned}
\langle j_\alpha(t) j_\beta(0) \rangle_H = {} & -\left(\frac{e_0}{\hbar}\right)^2 \sum_{KLMN} \frac{1}{N_\Omega^2} \sum_{\mathbf{k}_1 \mathbf{k}_2} e^{i\mathbf{k}_1 (\mathbf{R}_K - \mathbf{R}_N)} e^{i\mathbf{k}_2 (\mathbf{R}_M - \mathbf{R}_L)} e^{\frac{it}{\hbar}[\widetilde{\varepsilon}(\mathbf{k}_1) - \widetilde{\varepsilon}(\mathbf{k}_2)]} \\
& \times n_{\mathbf{k}_1} (1 - n_{\mathbf{k}_2}) R_{KL\alpha} \varepsilon_{KL} R_{MN\beta} \varepsilon_{MN} \left\langle e^{C_K(t)} e^{-C_L(t)} e^{C_M} e^{-C_N} \right\rangle_{\widetilde{H}}.
\end{aligned}
\tag{4.24}
$$

There is still the average over the phonon degrees of freedom to evaluate which is much more complicated. The major steps are given in the following. First consider the product $e^{C_K(t)} e^{-C_L(t)}$ which can be written as

$$
\begin{aligned}
e^{C_K(t)} e^{-C_L(t)} = {} & \sum_{l=0}^{\infty} \frac{1}{l!} \sum_{\mathbf{Q}_1 \ldots \mathbf{Q}_l} (g_{KK}^{\mathbf{Q}_1} - g_{LL}^{\mathbf{Q}_1})(g_{KK}^{\mathbf{Q}_2} - g_{LL}^{\mathbf{Q}_2}) \ldots (g_{KK}^{\mathbf{Q}_l} - g_{LL}^{\mathbf{Q}_l}) \\
& \times B_{\mathbf{Q}_1}(t) B_{\mathbf{Q}_2}(t) \ldots B_{\mathbf{Q}_l}(t),
\end{aligned}
\tag{4.25}
$$

where the phonon operators $B_{\mathbf{Q}}(t)$ are defined in Eq. (4.14). A product of such operators

appears in Eq. (4.24) together with an analogous product from $e^{C_M(0)}e^{-C_N(0)}$, which leads directly to the expectation value of products of phonon operators of the type

$$R_{lj} = \left\langle B_{\mathbf{Q}_1}(t)B_{\mathbf{Q}_2}(t)\dots B_{\mathbf{Q}_l}(t)B_{\mathbf{Q}'_1}(0)B_{\mathbf{Q}'_2}(0)\dots B_{\mathbf{Q}'_j}(0)\right\rangle_{\widetilde{H}}. \tag{4.26}$$

Since $B_{\mathbf{Q}}$ is linear in the basic phonon operators $b_{\mathbf{Q}}^\dagger$ and $b_{-\mathbf{Q}}$, this average vanishes for products with odd numbers of $B_{\mathbf{Q}}$ operators. For even numbers of such operators, the average is computed using Wick's theorem calculating all pairwise contractions. Thereby, it is possible to contract operators at different times which is

$$\left\langle B_{\mathbf{Q}_1}(t)B_{\mathbf{Q}'_1}(0)\right\rangle_{\widetilde{H}} = -\delta_{\mathbf{Q}_1,-\mathbf{Q}'_1}\Phi_{\mathbf{Q}_1}(t) \tag{4.27}$$

or of same time, which reads

$$\left\langle B_{\mathbf{Q}_1}(t)B_{\mathbf{Q}_2}(t)\right\rangle_{\widetilde{H}} = -\delta_{\mathbf{Q}_1,-\mathbf{Q}_2}\Phi_{\mathbf{Q}_1}(0)$$
$$\left\langle B_{\mathbf{Q}'_1}(0)B_{\mathbf{Q}'_2}(0)\right\rangle_{\widetilde{H}} = -\delta_{\mathbf{Q}'_1,-\mathbf{Q}'_2}\Phi_{\mathbf{Q}'_1}(0). \tag{4.28}$$

The auxiliary function $\Phi_{\mathbf{Q}}(t)$ is defined with the phonon frequency $\omega_{\mathbf{Q}}$ and the occupation number $N_{\mathbf{Q}}$ according to

$$\Phi_{\mathbf{Q}}(t) = N_{\mathbf{Q}}e^{i\omega_{\mathbf{Q}}t} + (1+N_{\mathbf{Q}})e^{-i\omega_{\mathbf{Q}}t}. \tag{4.29}$$

Let r be the number of pairwise averages of $B_{\mathbf{Q}}$ operators at different times and $0 \leq r \leq \min\{l,j\}$, the first possible contraction of Eq. (4.26) reads

$$\left\langle B_{\mathbf{Q}_1}(t)B_{\mathbf{Q}'_1}(0)\right\rangle_{\widetilde{H}}\left\langle B_{\mathbf{Q}_2}(t)B_{\mathbf{Q}'_2}(0)\right\rangle_{\widetilde{H}}\dots\left\langle B_{\mathbf{Q}_r}(t)B_{\mathbf{Q}'_r}(0)\right\rangle_{\widetilde{H}}$$
$$\times \left\langle B_{\mathbf{Q}_{r+1}}(t)B_{\mathbf{Q}_{r+2}}(t)\right\rangle_{\widetilde{H}}\dots\left\langle B_{\mathbf{Q}_{l-1}}(t)B_{\mathbf{Q}_l}(t)\right\rangle_{\widetilde{H}} \tag{4.30}$$
$$\times \left\langle B_{\mathbf{Q}'_{r+1}}(0)B_{\mathbf{Q}'_{r+2}}(0)\right\rangle_{\widetilde{H}}\dots\left\langle B_{\mathbf{Q}'_{j-1}}(0)B_{\mathbf{Q}'_j}(0)\right\rangle_{\widetilde{H}}.$$

Such a complete contraction is only non-zero if $l-r$ and $j-r$ are even. It can be evaluated to

$$P^r_{l,j} = \left(-\delta_{\mathbf{Q}_1,-\mathbf{Q}'_1}\Phi_{\mathbf{Q}_1}(t)\right)\left(-\delta_{\mathbf{Q}_2,-\mathbf{Q}'_2}\Phi_{\mathbf{Q}_2}(t)\right)\cdots\left(-\delta_{\mathbf{Q}_r,-\mathbf{Q}'_r}\Phi_{\mathbf{Q}_r}(t)\right)$$
$$\times \left(-\delta_{\mathbf{Q}_{r+1},-\mathbf{Q}_{r+2}}\Phi_{\mathbf{Q}_{r+1}}(0)\right)\left(-\delta_{\mathbf{Q}_{r+3},-\mathbf{Q}_{r+4}}\Phi_{\mathbf{Q}_{r+3}}(0)\right)\cdots\left(-\delta_{\mathbf{Q}_{l-1},-\mathbf{Q}_l}\Phi_{\mathbf{Q}_{l-1}}(0)\right)$$
$$\times \left(-\delta_{\mathbf{Q}'_{r+1},-\mathbf{Q}'_{r+2}}\Phi_{\mathbf{Q}'_{r+1}}(0)\right)\left(-\delta_{\mathbf{Q}'_{r+3},-\mathbf{Q}'_{r+4}}\Phi_{\mathbf{Q}'_{r+3}}(0)\right)\cdots\left(-\delta_{\mathbf{Q}'_{j-1},-\mathbf{Q}'_j}\Phi_{\mathbf{Q}'_{j-1}}(0)\right). \tag{4.31}$$

One observes that in (4.25) the summation indices $\mathbf{Q}_i$ can be interchanged which gives an expression equivalent to a permutation of $B_{\mathbf{Q}}(t)$ operators. Hence, the evaluation of the

average in (4.26) is a combinatorial problem and one finally obtains the expression

$$R_{l,j} = \sum_{\substack{r=0 \\ (l-r)\,even \\ (j-r)\,even}}^{min(l,j)} \frac{l!\,j!}{r!\,2^{(l-r)/2}\left(\frac{l-r}{2}\right)!\,2^{(j-r)/2}\left(\frac{j-r}{2}\right)!}P_{l,j}^r \qquad (4.32)$$

for the full contraction of (4.26). Putting this together with (4.25), the phonon average in (4.24) is given by

$$\left\langle e^{C_K(t)}e^{-C_L(t)}e^{C_M}e^{-C_N}\right\rangle_{\widetilde{H}} = \sum_{\substack{l,j=0 \\ (l+j)\,even}}^{\infty} \frac{1}{l!\,j!} \sum_{\substack{\{\mathbf{Q}_l\} \\ \{\mathbf{Q}'_j\}}} \prod_{i=1}^{l}(g_{KK}^{\mathbf{Q}_i}-g_{LL}^{\mathbf{Q}_i})\prod_{k=1}^{j}(g_{MM}^{\mathbf{Q}'_k}-g_{NN}^{\mathbf{Q}'_k})R_{l,j}, \quad (4.33)$$

and after some regrouping of terms one finds

$$\left\langle e^{C_K(t)}e^{-C_L(t)}e^{C_M}e^{-C_N}\right\rangle_{\widetilde{H}} = \exp\left[-\frac{1}{2}\sum_{\mathbf{Q}}\Phi_{\mathbf{Q}}(0)G_{KLKL}^{\mathbf{Q}}\right]\exp\left[-\frac{1}{2}\sum_{\mathbf{Q}}\Phi_{\mathbf{Q}}(0)G_{MNMN}^{\mathbf{Q}}\right]$$

$$\times \exp\left[-\sum_{\mathbf{Q}}\Phi_{\mathbf{Q}}(t)G_{KLMN}^{\mathbf{Q}}\right]$$

$$(4.34)$$

with some effective electron-phonon coupling constant squared $G_{KLMN}^{\mathbf{Q}}$ which are defined as

$$G_{KLMN}^{\mathbf{Q}} = \left(g_{KK}^{\mathbf{Q}} - g_{LL}^{\mathbf{Q}}\right)\left(g_{MM}^{-\mathbf{Q}} - g_{NN}^{-\mathbf{Q}}\right). \qquad (4.35)$$

Note that the first two exponential factors in Eq. (4.34) are of equal quality. Since $\Phi_{\mathbf{Q}}(0) = 1 + 2N_{\mathbf{Q}}$ and $G_{KLKL}^{\mathbf{Q}} = |g_{KK}^{\mathbf{Q}} - g_{LL}^{\mathbf{Q}}|^2$, they give rise to the bandwidth narrowing known already from Eq. (3.39) and reduce the mobility. In contrast, the third exponential factor can amplify the mobility and explicitly describes phonon absorption and emission events as will be demonstrated later in this thesis. Inserting Eq. (4.34) into Eq. (4.24) and using the polaronic $\widetilde{\varepsilon}$ from Eq. (3.39), one finds

$$\langle j_\alpha(t)j_\beta(0)\rangle_H = -\left(\frac{e_0}{\hbar}\right)^2 \sum_{KLMN} R_{KL\alpha}\widetilde{\varepsilon}_{KL}R_{MN\beta}\widetilde{\varepsilon}_{MN}e^{-\sum_{\mathbf{Q}}\Phi_{\mathbf{Q}}(t)G_{KLMN}^{\mathbf{Q}}}$$

$$\times \frac{1}{N_\Omega^2}\sum_{\mathbf{k}_1\mathbf{k}_2} n_{\mathbf{k}_1}(1-n_{\mathbf{k}_2})e^{i\mathbf{k}_1(\mathbf{R}_K-\mathbf{R}_N)}e^{i\mathbf{k}_2(\mathbf{R}_M-\mathbf{R}_L)}e^{\frac{it}{\hbar}[\widetilde{\varepsilon}(\mathbf{k}_1)-\widetilde{\varepsilon}(\mathbf{k}_2)]}. \qquad (4.36)$$

Finally, shifting indices according to $L \to K + L$ and $N \to M + N$ and $M \to K + M$ results in an expression which, as a result of the translation symmetry, no longer depends on the spatial index K. Subsequent summation over K gives a prefactor N_Ω. With Eq. (4.3) and

$\mathbf{R}_L \equiv \mathbf{R}_{0L}$ and $\widetilde{\varepsilon}_L \equiv \widetilde{\varepsilon}_{0L}$, one finally obtains

$$
\begin{aligned}
\mu_{\alpha\beta} = & -\frac{1}{e_0 N_c\, 2k_B T} \left(\frac{e_0}{\hbar}\right)^2 \sum_{LMN} R_{L\alpha}\widetilde{\varepsilon}_L R_{N\beta}\widetilde{\varepsilon}_N \\
& \times \frac{1}{N_\Omega} \sum_{\mathbf{k}_1 \mathbf{k}_2} e^{-i\mathbf{k}_1(\mathbf{R}_M+\mathbf{R}_N)} e^{i\mathbf{k}_2(\mathbf{R}_M-\mathbf{R}_L)} n_{\mathbf{k}_1}(1-n_{\mathbf{k}_2}) \\
& \times \int_{-\infty}^{\infty} dt\, e^{\frac{it}{\hbar}[\widetilde{\varepsilon}(\mathbf{k}_1)-\widetilde{\varepsilon}(\mathbf{k}_2)]} e^{-\left[\sum_{\mathbf{Q}} \Phi_{\mathbf{Q}}(t) G_{0L0N}^{\mathbf{Q}} e^{-i\mathbf{Q}\mathbf{R}_M}\right]}
\end{aligned}
\tag{4.37}
$$

which is the primary result for the carrier mobility of the present derivation.[2] It includes coherent band transport and incoherent hopping as will be demonstrated in the following section. Importantly, the general form of Eq. (4.37) allows for the application to arbitrary phonon dispersion $\omega_{\mathbf{Q}}$ and arbitrary matrix elements $g_{MM}^{\mathbf{Q}}$ of the electron-phonon coupling.

4.2 Mobility Contributions

4.2.1 Coherent Band Transport

I proceed in order to extract the essential physics and discuss Eq. (4.37) in terms of contributing scattering events. This is most intuitive if the zeroth order of electron-phonon interaction $(G^{\mathbf{Q}} = 0)$ is split off in the third line of Eq. (4.37):

$$
e^{-\sum_{\mathbf{Q}} \Phi_{\mathbf{Q}}(t) G_{0L0N}^{\mathbf{Q}} e^{-i\mathbf{Q}\mathbf{R}_M}} = 1 + \left(e^{-\sum_{\mathbf{Q}} \Phi_{\mathbf{Q}}(t) G_{0L0N}^{\mathbf{Q}} e^{-i\mathbf{Q}\mathbf{R}_M}} - 1\right).
\tag{4.38}
$$

In terms of physics, I separate coherent transport (no phonon-scattering) from incoherent transport (scattering by phonons). Accordingly, one obtains

$$
\mu_{\alpha\beta} = \mu_{\alpha\beta}^{(coh)} + \mu_{\alpha\beta}^{(inc)},
\tag{4.39}
$$

where the coherent part reads

$$
\begin{aligned}
\mu_{\alpha\beta}^{(coh)} = & -\frac{e_0}{2N_c k_B T \hbar^2} \sum_{LMN} R_{L\alpha}\widetilde{\varepsilon}_L R_{N\beta}\widetilde{\varepsilon}_N \\
& \times \frac{1}{N_\Omega} \sum_{\mathbf{k}_1 \mathbf{k}_2} e^{-i\mathbf{k}_1(\mathbf{R}_M+\mathbf{R}_N)} e^{i\mathbf{k}_2(\mathbf{R}_M-\mathbf{R}_L)} \\
& \times n_{\mathbf{k}_1}(1-n_{\mathbf{k}_2}) \int_{-\infty}^{\infty} dt\, e^{\frac{it}{\hbar}[\widetilde{\varepsilon}(\mathbf{k}_1)-\widetilde{\varepsilon}(\mathbf{k}_2)]}.
\end{aligned}
\tag{4.40}
$$

This mobility expression can be interpreted in terms of contributing scattering events from some initial states $\mathbf{k}_1$ into final states $\mathbf{k}_2$. The sum over $\mathbf{k}_1$ and $\mathbf{k}_2$ in (4.40) includes all such events according to the probability $n_{\mathbf{k}_1}$ that an initial state is occupied times the probability

---

[2]The shorthand notation for the scalar product $\mathbf{Q}\mathbf{R}_M$ is to be understood as $\mathbf{q}\mathbf{R}_M$.
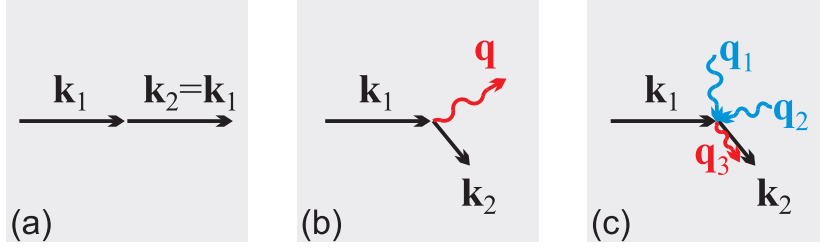
Figure 4.1: Typical coherent (a) and incoherent (b) and (c) processes involved in carrier transport. In (c) a third order process (one emitted and two absorbed phonons) with a resulting phonon wavevector $\mathbf{q} = \mathbf{q}_1 + \mathbf{q}_2 - \mathbf{q}_3$ is displayed

$(1 - n_{\mathbf{k}_2})$ of the final state being empty (Pauli blocking factor). From the time integration in Eq. (4.40) it gets obvious that the energy of the initial polaron $\widetilde{\varepsilon}(\mathbf{k}_1)$ has to match the energy of the final polaron $\widetilde{\varepsilon}(\mathbf{k}_2)$ (energy conservation). Moreover, considering the real space sum over the index M which only occurs in the exponentials gives a Kronecker delta in the wavevectors of initial and scattered polaron $\delta_{\mathbf{k}_1,\mathbf{k}_2}$ (momentum conservation).

Such a (maybe trivial) scattering event, where initial and final wavevectors coincide is depicted in Fig. 4.1 (a). The momentum conservation in the polaron wavevectors in $\mu^{(coh)}$ reflects the coherence aspect of band transport, i.e., the moving particle does not loose its phase coherence and its momentum relaxation length is infinite. From the momentum conservation it follows that $\widetilde{\varepsilon}(\mathbf{k}_1) = \widetilde{\varepsilon}(\mathbf{k}_2)$ is immediately fulfilled and one observes that the mobility $\mu^{(coh)}$ becomes infinite, as expected for coherent transport without any scattering mechanism. In real crystals, the mean free path (or the coherence time) can be reduced by other scattering mechanism beyond the model (impurities, disorder, electron-electron scattering ...). Such processes may be accounted for by the introduction of a disorder parameter τ similarly to previous work. [44] Therefore, I introduce a constant limiting scattering time and replace technically

$$\int dt \rightarrow \int dt \, e^{-\left(\frac{t}{\tau}\right)^2}. \tag{4.41}$$

More complicated expressions for the scattering time such as a $\mathbf{k}$ dependent form are avoided here since these scattering mechanisms are not in the focus of the present work. The Gaussian broadening limits the coherence time to τ. The corresponding energy $\frac{\hbar}{\tau}$ can be regarded as a static disorder parameter which mimics different on-site energies for example.

The resulting mobility can be written as

$$\mu^{(coh)}_{\alpha\beta} = \frac{\sqrt{\pi} e_0 \tau}{2 N_c k_B T} \sum_{\mathbf{k}_1} n_{\mathbf{k}_1}(1 - n_{\mathbf{k}_1}) \widetilde{v}_\alpha(\mathbf{k}_1) \widetilde{v}_\beta(\mathbf{k}_1) \tag{4.42}$$

where I have introduced the polaron band velocity

$$\widetilde{v}_\alpha(\mathbf{k}) = \frac{1}{\hbar}\frac{\partial\widetilde{\varepsilon}(\mathbf{k})}{\partial k_\alpha}.$$

(4.43)

The fact that the band velocity appears explicitly in Eq. (4.42) is a result of the underlying coherence character of this transport contribution. The tilde in (4.43) is reminiscence to its polaronic nature and therefore temperature dependence because it is affected by the band narrowing of Eq. (3.39).

Apart from the tildes, Eq. (4.42) is a well known expression that may also be derived from the Boltzmann transport equation [56]. However, an essential difference is that the expression (4.42) is now generalized to polarons. In Sec. 4.3.4 the limit of small electron-phonon coupling is discussed, where the polarons reduce to the bare particles and the expression from the Boltzmann equation is recovered.[3] Finally, I give another form of the result for the coherent part of the mobility. If the squared velocity $\widetilde{v}_\alpha^2(\mathbf{k})$ is written as $\widetilde{v}_\alpha^2\left[\widetilde{\varepsilon}(\mathbf{k})\right]$ one can further introduce the polaron density of states

$$D(\widetilde{\varepsilon}) = \sum_k \delta\left[\widetilde{\varepsilon} - \widetilde{\varepsilon}(\mathbf{k})\right]$$

(4.44)

and write the diagonal elements of the mobility tensor as

$$\mu_\alpha^{(coh)} = \frac{\sqrt{\pi}e_0\tau}{2N_ck_BT}\int_0^\infty d\widetilde{\varepsilon}\, D\left(\widetilde{\varepsilon}\right) n_{\widetilde{\varepsilon}}(1-n_{\widetilde{\varepsilon}})\widetilde{v}_\alpha^2(\widetilde{\varepsilon}).$$

(4.45)

Again, Eq. (4.45) is also similar to a well known textbook formula [57] with the generalization of all quantities (DOS, energy, occupation, velocity) from electrons to polarons.

4.2.2 Incoherent Processes

The remaining contribution to the total mobility comes from incoherent scattering events and reads

$$\begin{aligned}
\mu_{\alpha\beta}^{(inc)} = &-\frac{1}{e_0N_c\,2k_BT}\left(\frac{e_0}{\hbar}\right)^2\sum_{LMN}R_{L\alpha}\widetilde{\varepsilon}_L R_{N\beta}\widetilde{\varepsilon}_N\\
&\times\frac{1}{N_\Omega}\sum_{\mathbf{k}_1\mathbf{k}_2}e^{-i\mathbf{k}_1(\mathbf{R}_M+\mathbf{R}_N)}e^{i\mathbf{k}_2(\mathbf{R}_M-\mathbf{R}_L)}n_{\mathbf{k}_1}(1-n_{\mathbf{k}_2})\\
&\times\int_{-\infty}^\infty dt\, e^{\frac{it}{\hbar}[\widetilde{\varepsilon}(\mathbf{k}_1)-\widetilde{\varepsilon}(\mathbf{k}_2)]}\left(e^{-\left[\sum_\mathbf{Q}\Phi_\mathbf{Q}(t)G_{0L0N}^\mathbf{Q}e^{-i\mathbf{QR}_M}\right]}-1\right).
\end{aligned}$$

(4.46)

Similarly to the preceding paragraph, I briefly discuss the scattering events that contribute to the incoherent part of the mobility. First, consider in Eq. (4.46) the real space sum over M. Here, the index occurs also in the third line of Eq. (4.46). Therefore, the momentum

---

[3]An additional factor of $\frac{\sqrt{\pi}}{2}$ appears here due to the definition of τ as the width of a Gaussian function.

conservation now includes phonon wavevectors and reads $\delta_{\mathbf{k}_1+\mathbf{q},\mathbf{k}_2}$. Hereby, $\mathbf{q}$ is the sum of all phonon vectors which contribute in the scattering process. According to the exponential sum in the third line of (4.46), this may involve any number of phonons, because all orders of electron-phonon interaction contribute. In Fig. 4.1 such incoherent processes are depicted in (b) and (c). Only in the first order (Fig. 4.1 (b)) does $\mathbf{q}$ represent the wavevector of a single scattered phonon. In Fig. 4.1 (c) a third order process ($n = 3$) is depicted as well. Also, the energy conservation is somewhat more complicated compared to the coherent mobility. The energy difference of initial and final polaron is no longer zero as for the coherent part but must account for the phonon energies of created and annihilated vibrations. This is taken care of automatically in (4.46) through the time integration. Finally, the weight of such a scattering event is influenced by the occupation numbers of particles $n_{\mathbf{k}_1}(1 - n_{\mathbf{k}_2})$ as was observed similarly for the coherent contribution. Such incoherent scattering processes are to be regarded as stochastic processes since the phonon fluctuations are statistically independent. In this way the phase coherence of the particles is destroyed in each scattering event.

If there is no electron-phonon coupling at all, the incoherent contribution completely vanishes. In contrast thereto, a non-zero electron-phonon interaction influences the incoherent contribution through two counteracting effects. Of course, the increasing polaron mass with increasing g tends to reduce the mobility. On the other hand, the stronger the electron-phonon coupling the stronger can temperature promote charge transport.

Expression (4.46) can be simplified if one assumes that the scatterers are dispersionless optical phonons, i.e., $\omega_{\mathbf{Q}} \to \omega_\lambda$, $N_{\mathbf{Q}} \to N_\lambda$, which implies that $\Phi_{\mathbf{Q}}(t) \to \Phi_\lambda(t)$, where

$$\Phi_\lambda(t) = N_\lambda e^{i\omega_\lambda t} + (1 + N_\lambda)e^{-i\omega_\lambda t}, \tag{4.47}$$

and if one, accordingly, sets

$$g_{MM}^{\mathbf{Q}} = \frac{g_\lambda}{\sqrt{N_\Omega}} e^{i\mathbf{q}\mathbf{R}_M}. \tag{4.48}$$

As a result one obtains

$$
\begin{aligned}
\mu_{\alpha\beta}^{(inc)} = &-\frac{1}{e_0 N_c \, 2k_B T} \left(\frac{e_0}{\hbar}\right)^2 \sum_{LMN} R_{L\alpha}\widetilde{\varepsilon}_L R_{N\beta}\widetilde{\varepsilon}_N \\
&\times \frac{1}{N_\Omega} \sum_{\mathbf{k}_1\mathbf{k}_2} e^{-i\mathbf{k}_1(\mathbf{R}_M+\mathbf{R}_N)} e^{i\mathbf{k}_2(\mathbf{R}_M-\mathbf{R}_L)} n_{\mathbf{k}_1}(1 - n_{\mathbf{k}_2}) \\
&\times \int_{-\infty}^{\infty} dt\, e^{\frac{it}{\hbar}[\widetilde{\varepsilon}(\mathbf{k}_1)-\widetilde{\varepsilon}(\mathbf{k}_2)]} \left(e^{-\left[\delta_0^M-\delta_L^M-\delta_{-N}^M+\delta_{L-N}^M\right]\sum_\lambda \Phi_\lambda(t)g_\lambda^2} - 1\right).
\end{aligned}
\tag{4.49}
$$

In order to further simplify this expression, I concentrate on the most important terms in Eq. (4.49). These terms are identified from the minimization of $\left[\delta_0^M - \delta_L^M - \delta_{-N}^M + \delta_{L-N}^M\right]$

in the last exponential in (4.49). The leading terms are obtained for $L = M$ and $-N = M$. It is confirmed numerically that contributions from all other terms are minor. Taking only the leading terms into account one finds

$$
\mu_{\alpha\beta}^{(inc)} = \frac{e_0}{N_c \hbar^2 \, 2k_B T} \sum_L R_{L\alpha} R_{L\beta} \widetilde{\varepsilon}_L^2 \frac{1}{N_\Omega} \sum_{\mathbf{k}_1 \mathbf{k}_2} n_{\mathbf{k}_1} (1 - n_{\mathbf{k}_2})
$$
$$
\times \int_{-\infty}^{\infty} dt \, e^{\frac{it}{\hbar}[\widetilde{\varepsilon}(\mathbf{k}_1) - \widetilde{\varepsilon}(\mathbf{k}_2)]} \left(e^{2 \sum_\lambda \Phi_\lambda(t) g_\lambda^2} - 1 \right).
\tag{4.50}
$$

At this point, one observes that the anisotropy in Eq. (4.50) results solely from the prefactor

$$
\widetilde{V}_{\alpha\beta}^{pol} = \left(\frac{1}{\hbar} \right)^2 \sum_L R_{L\alpha} R_{L\beta} \widetilde{\varepsilon}_L^2
\tag{4.51}
$$

which is of dimension velocity squared. It sums up all possible hoppings to neighbors in different directions in real space. In contrast to the coherent contribution (4.42), where the introduction of the band velocity (4.43) was possible, reflecting the delocalization aspect of coherent transport, here the quantity $\widetilde{V}_{\alpha\beta}^{pol}$ reflects the localization aspect of incoherent transport. This quantity can be looked upon as a measure for the polaron hopping in real space since it is dominated by the nearest neighbor transfer rates.

For consistency, again the time integral in Eq. (4.50) is replaced according to Eq. (4.41) introducing the same collision time τ from impurity scattering as a disorder parameter and one obtains

$$
\mu_{\alpha\beta}^{(inc)} = \frac{e_0}{N_c \, 2k_B T} \widetilde{V}_{\alpha\beta}^{pol} \frac{1}{N_\Omega} \sum_{\mathbf{k}_1 \mathbf{k}_2} n_{\mathbf{k}_1} (1 - n_{\mathbf{k}_2})
$$
$$
\times \int_{-\infty}^{\infty} dt \, e^{\frac{it}{\hbar}[\widetilde{\varepsilon}(\mathbf{k}_1) - \widetilde{\varepsilon}(\mathbf{k}_2)]} \left(e^{2 \sum_\lambda \Phi_\lambda(t) g_\lambda^2} - 1 \right) e^{-\left(\frac{t}{\tau}\right)^2}.
\tag{4.52}
$$

4.3 Limiting Cases

In the preceding part of this chapter I have evaluated the mobility from the Kubo formula (Eq. (4.3)) and obtained an analytical expression (Eq. (4.37)) which includes coherent and incoherent contributions for arbitrary values of the electron-phonon coupling strength and arbitrary bandwidth. The mobility in Eq. (4.37) is a generalization of Holstein's small-polaron model because it can also describe the motion of large polarons (small g) and covers even the case of Bloch waves ($g = 0$). This was possible because the narrow-band approximation was avoided and, instead, I incorporated the full bandwidth by means of a mixed real-space and reciprocal-space representation. Both contributing transport modes, coherent and incoherent, coexist and have been split for separate discussions in Sec. 4.2. The simplified expressions are given by Eqs. (4.42) and (4.52), respectively. This section aims at illustrating the theory in its limiting cases and compares the results to the narrow-band theory.

4.3.1 Narrow-Band Approximation

The NBA can be obtained from the most general result Eq. (4.37) by setting $\widetilde{\varepsilon}(\mathbf{k}_1) = \widetilde{\varepsilon}(\mathbf{k}_2)$ for all wavevectors and assuming, accordingly, a constant distribution function $n_{\mathbf{k}} \to c \equiv N_c/N_\Omega$ as well

$$\mu_{\alpha\beta} = -\frac{1}{e_0 N_c} \frac{1}{2k_B T} \left(\frac{e_0}{\hbar}\right)^2 \sum_{LMN} R_{L\alpha} \widetilde{\varepsilon}_L R_{N\beta} \widetilde{\varepsilon}_N$$

$$\times \frac{1}{N_\Omega} \sum_{\mathbf{k}_1 \mathbf{k}_2} e^{-i\mathbf{k}_1(\mathbf{R}_M + \mathbf{R}_N)} e^{i\mathbf{k}_2(\mathbf{R}_M - \mathbf{R}_L)} c(1 - c) \qquad (4.53)$$

$$\times \int_{-\infty}^{\infty} dt\, e^{-\left[\sum_{\mathbf{Q}} \Phi_{\mathbf{Q}}(t) G_{0L0N}^{\mathbf{Q}} e^{-i\mathbf{Q}\mathbf{R}_M}\right]}.$$

Since the wavevectors $\mathbf{k}_1$ and $\mathbf{k}_2$ only appear in the phase factors, the sums are readily performed and with Eqs. (4.41), (4.48), and (4.51) and one finally obtains

$$\mu_{\alpha\beta}^{(NBA)} = \frac{e_0(1 - c)}{2k_B T} \widetilde{V}_{\alpha\beta}^{pol} \int_{-\infty}^{\infty} dt\, e^{2\sum_\lambda \Phi_\lambda(t) g_\lambda^2} e^{-\left(\frac{t}{\tau}\right)^2}. \qquad (4.54)$$

This result is the narrow-band result as derived previously for the case of local electron-phonon coupling. [30, 44] In Ref. [44] also the generalization to nonlocal electron-phonon interaction within the NBA according to Fig. 1.1 has been successfully derived. In this case one must replace

$$\varepsilon_L^2 \to (\varepsilon_L - \Delta_L)^2 + \frac{1}{2} \sum_\lambda \left(\hbar\omega_\lambda g_L^\lambda\right)^2 \Phi_\lambda(t) \qquad (4.55)$$

in $\widetilde{V}_{\alpha\beta}^{pol}$ which, in this case, cannot be written as a prefactor to the time integral like in (4.54) but appears under the integral since $\Phi_\lambda(t)$ is a time dependent function. The polaron shift $\Delta_L \equiv \Delta_{0L}$ has been defined in Eq. (3.34).

Here I proceed with the discussion of the mobility in (4.54) which includes only local electron-phonon coupling. The narrow-band theory is compared to the general theory for the full bandwidth. Equation (4.54) may also be split into a coherent and incoherent part using the separation $e^{2\sum_\lambda \Phi_\lambda(t) g_\lambda^2} = 1 + \left(e^{2\sum_\lambda \Phi_\lambda(t) g_\lambda^2} - 1\right)$, in the spirit of Eq. (4.38). This is similar to Holstein's original idea of a mobility summation $\mu = \mu^{(1)} + \mu^{(2)}$ reflecting coherent tunneling and hopping motion, respectively. [29] Such a resolution also occurs in later theoretical work. [22, 37, 58] However, in view of the assumed localized nature of the polarons it had not been considered that $\mu^{(1)}$ should be related to the band conduction as obtained from the Boltzmann equation. This is not surprising since the resulting formulas and numerical results for $\mu^{(1)}$ differ strongly from the coherent mobility $\mu^{(coh)}$, Eq. (4.42), of the present theory that goes beyond the narrow-band limit (see also Chap. 5 for numerical studies). Consequently, the characteristics of the contribution $\mu^{(1)}$ from such localized quasiparticles in the narrow-

band theory appear quite strange. One common flaw is the presence of a low-temperature singularity T^{-1} which does not occur in band transport (see Sec. 4.3.2). This demonstrates that narrow-band theories are not valid at lower T, as previously discussed by Kenkre [34].

There are two main differences between the present theory and the narrow-band theory. First, in the present approach, there are additional scattering channels (inelastic scattering, i.e., $\widetilde{\varepsilon}(\mathbf{k}_1) \neq \widetilde{\varepsilon}(\mathbf{k}_2)$) compared to the narrow-band theory which only take elastic scattering into account, where the energy difference for initial and final polaron states is always zero, $\widetilde{\varepsilon}(\mathbf{k}_1) = \widetilde{\varepsilon}(\mathbf{k}_2)$. Second, the channels which were already included in the narrow-band theory are now much better described since the actual state energy $\widetilde{\varepsilon}$ has become a relevant quantity and is incorporated properly. The NBA partially neglects the energy dispersion which immediately leads to the incorrect matching of initial and final state energies in the narrow-band theory.

It is clear that for high enough temperatures the above replacements, which have been introduced to arrive at the narrow-band result, become exact and the full theory coincides with the narrow-band theory. In contrast, for low and medium temperatures one observes strong improvements over the NBA. This will be further discussed below and accompanied by numerical studies in Chap. 5.

4.3.2 Low Temperatures

In order to calculate the $T \to 0$ limit of the coherent contribution (4.42) in the full theory, I make use of the low-temperature limit of $n_{\mathbf{k}}(1 - n_{\mathbf{k}})$ which can be traced back to the energy derivative of the occupation number according to $n_{\mathbf{k}}(1 - n_{\mathbf{k}}) = -k_B T \frac{\partial n_{\widetilde{\varepsilon}(\mathbf{k})}}{\partial \widetilde{\varepsilon}(\mathbf{k})}$. The derivative of the Fermi-Dirac distribution at zero temperature (step function) leads to the limit $\lim_{T \to 0} \frac{\partial n_{\widetilde{\varepsilon}(\mathbf{k})}}{\partial \widetilde{\varepsilon}(\mathbf{k})} = \delta[\widetilde{\varepsilon}(\mathbf{k}) - \zeta]$. From a physical point of view, this means that only the polarons from within a thermal layer of width $\propto k_B T$ at the chemical potential ζ contribute to the current. As a consequence, this $k_B T$ term exactly cancels the prefactor $\frac{1}{k_B T}$ in Eq. (4.42) resulting in a finite carrier mobility for $T = 0$ K. Importantly, this is a major improvement over the NBA which involves a replacement $n_{\mathbf{k}}(1 - n_{\mathbf{k}}) \to c(1 - c)$ and results in a $\frac{1}{k_B T}$ divergence. Therefore, the correct inclusion of the Fermi-Dirac statistics in the present theory is essential for the removal of this unphysical singularity.

In the special case of an isotropic system with a parabolic band structure one obtains the low-T limit as

$$\mu^{(coh)} = \frac{\sqrt{\pi} e_0 \tau}{2 m_{pol}^*}, \tag{4.56}$$

which resembles the Drude expression for the mobility but generalized to polarons as charge

carriers. The polaron effective mass is given by

$$m^*_{pol} = m^*_{el/hole} e^{\sum_\lambda g_\lambda^2}. \tag{4.57}$$

This mass is increased compared to the bare electron/hole mass due to the coupling to the phonons. As discussed in Sec. 3.4, the occurring exponential factor is the inverse of the factor which occurs for the bandwidth in the $T \to 0$ limit (see, e.g., Eq. (3.40)).

The low-T regime of the incoherent mobility $\mu^{(inc)}$ from Eq. (4.52) is analyzed for a single scatterer λ of frequency ω_λ in the limit of a small phonon occupation number ($N_\lambda \ll 1$). Assuming ultrapure crystals where static disorder is much smaller than phonon induced dynamic disorder, i.e. $1/\tau \ll \omega_\lambda$, one finds the largest term

$$\mu^{(inc)} \propto g_\lambda^2 \frac{N_\lambda}{T} \approx \frac{g_\lambda^2}{T} e^{-\frac{\hbar\omega_\lambda}{k_B T}}. \tag{4.58}$$

Basically, this result describes an activation law with the phonon energy as a relevant energy barrier. The process behind this leading term is a phonon absorption process, which elevates the polaron above the Fermi energy. The frequency of occurrence of such an event is proportional to N_λ, the number of available phonons, and the activation law should rather be regarded as a probability than a real barrier. Finally, the $T \to 0$ limit of Eq. (4.58) is obtained as

$$\mu^{(inc)} \to 0, \tag{4.59}$$

i.e., the incoherent mobility vanishes.

4.3.3 High Temperatures

The effective polaron mass increases with rising temperature which is a direct consequence of the band narrowing. Accordingly, in the $T \to \infty$ limit, the coherent mobility behaves like

$$\mu^{(coh)} \to 0. \tag{4.60}$$

For the remaining incoherent contribution, the distribution function for polarons in Eq. (4.52) becomes constant, $n_\mathbf{k} \to c$, if the temperature is high enough that the bandwidth becomes much smaller than $k_B T$. If the bandwidth is also smaller than all relevant phonon energies, the narrow-band limit applies and one can set $\widetilde{\varepsilon}(\mathbf{k}_1) = \widetilde{\varepsilon}(\mathbf{k}_2)$ in Eq. (4.52) and obtains

$$\mu^{(inc)}_{\alpha\beta} \to \frac{e_0(1-c)}{2k_B T} \widetilde{V}^{pol}_{\alpha\beta} \int_{-\infty}^{\infty} dt \left(e^{2\sum_\lambda \Phi_\lambda(t) g_\lambda^2} - 1 \right) e^{-\left(\frac{t}{\tau}\right)^2}. \tag{4.61}$$

For sufficiently large temperatures ($2N_\lambda g_\lambda^2 > 1$), the -1 term in the parenthesis is negligibly small and the right hand side of Eq. (4.61) equals the narrow-band result from Eq. (4.54).

In fact, Eq. (4.61) corresponds to the hopping term $\mu^{(2)}$ in Holstein's original narrow-band theory (see the discussion of Eq. (4.54) in Sec. 4.3.1). The final result for the high-T limit,

$$\mu^{(inc)} \propto T^{-3/2} e^{-\frac{E_p}{k_B T}}, \tag{4.62}$$

where $E_p = \frac{1}{2} g_\lambda^2 \hbar \omega_\lambda$ is the polaron binding energy, is obtained as in Ref. [44]. Since the coherent contribution $\mu^{(coh)}$ vanishes for high T, it follows that this activation law also holds for the total mobility μ in the present theory.

This result is discussed briefly. The temperature dependence found in Eq. (4.62) is the same as in the classical Marcus theory for electron transfer [46, 47]. In the Marcus theory, the polaron binding energy E_p is regarded a barrier for the charge carrier between two states of localization on different sites (initial and final states for the charge transfer process). Note that beyond the maximum of $\mu(T)$ in Eq. (4.62) ($k_B T > \frac{2}{3} E_p$), the mobility is a decreasing function of T, while for lower temperatures ($k_B T < \frac{2}{3} E_p$) one finds an activation behavior giving larger μ for larger T.

Comparing the high-T limit in Eq. (4.62) to the low-T limit of the incoherent hopping contribution in Eq. (4.58), there are differences in the T dependence of the prefactor as well as in the activation energy in the exponential. While at low T the leading term arises from a single phonon scattering event ($\propto g_\lambda^2$) and is directly related to the number of available phonons N_λ, the high-T limit is caused by the electron-phonon coupling in all orders (since the coupling constant g_λ appears in the exponent in (4.62)) and is not easily related to phonon occupation numbers.

4.3.4   Small Electron-Phonon Coupling

As an important limiting case, the present theory covers the bare electron limit if one reduces the electron-phonon coupling $g \to 0$ and hence retains the bare electronic band velocity

$$\widetilde{v}_\alpha(\mathbf{k}) \to v_\alpha(\mathbf{k}) = \frac{1}{\hbar} \frac{\partial \varepsilon(\mathbf{k})}{\partial k_\alpha}. \tag{4.63}$$

Accordingly, Eqs. (4.42) and (4.45) reduce to

$$\mu_{\alpha\beta}^{(coh)} = \frac{\sqrt{\pi} e_0 \tau}{2 N_c k_B T} \sum_{\mathbf{k}_1} n_{\mathbf{k}_1} (1 - n_{\mathbf{k}_1}) v_\alpha(\mathbf{k}_1) v_\beta(\mathbf{k}_1) \tag{4.64}$$

and

$$\mu_\alpha^{(coh)} = \frac{\sqrt{\pi} e_0 \tau}{2 N_c k_B T} \int_0^\infty d\varepsilon \, D(\varepsilon) \, n_\varepsilon (1 - n_\varepsilon) v_\alpha^2(\varepsilon), \tag{4.65}$$

respectively, where $D(\varepsilon)$ is the ordinary (bare electronic) DOS and $n_{\mathbf{k}}$ and n_ε are taken at the bare electronic structure.

Incoherent transport only contributes for finite electron-phonon interaction ($g \neq 0$). In this case, the electron-phonon coupling in the term $\left(e^{2\sum_\lambda \Phi_\lambda(t)g_\lambda^2} - 1\right)$ of Eq. (4.52) enables scattering and thus provides transport channels involving the creation or removal of phonons. For small g one can replace $\left(e^{2\sum_\lambda \Phi_\lambda(t)g_\lambda^2} - 1\right) \rightarrow 2\sum_\lambda \Phi_\lambda(t)g_\lambda^2$ in Eq. (4.52) and the time integration, in the limit $\tau \rightarrow \infty$, gives rise to delta functions in the energies which, for a single scatterer, reads

$$
\begin{aligned}
&\frac{1}{\hbar} \int_{-\infty}^{\infty} dt \left\{ N_\lambda e^{\frac{it}{\hbar}\left(\widetilde{\varepsilon}_{\mathbf{k}_1} - \widetilde{\varepsilon}_{\mathbf{k}_2} + \hbar\omega_\lambda\right)} + (1 + N_\lambda)\, e^{\frac{it}{\hbar}\left(\widetilde{\varepsilon}_{\mathbf{k}_1} - \widetilde{\varepsilon}_{\mathbf{k}_2} - \hbar\omega_\lambda\right)} \right\} \\
&= N_\lambda \delta(\widetilde{\varepsilon}_{\mathbf{k}_1} - \widetilde{\varepsilon}_{\mathbf{k}_2} + \hbar\omega_\lambda) + (1 + N_\lambda)\, \delta\left(\widetilde{\varepsilon}_{\mathbf{k}_1} - \widetilde{\varepsilon}_{\mathbf{k}_2} - \hbar\omega_\lambda\right).
\end{aligned}
\tag{4.66}
$$

From this equation one directly identifies both phonon absorption ($\propto N_\lambda$) and emission ($\propto 1 + N_\lambda$) processes with the respective energies $\pm\hbar\omega_\lambda$ that govern the incoherent mobility in the limit of small electron-phonon interaction.

Chapter 5

Numerical Model Simulations

5.1 Comparison of New Approach to Narrow-Band Theory

The present theory as derived in Chap. 4 is further discussed and illustrated by a numerical study for a model crystal. The discussion covers the comparison to the narrow-band theory as well as an analysis of new features. First I specify the model crystal to which both theories are applied. Consider, for simplicity, an orthorhombic crystal with lattice constants $a = 4$ Å, $b = 5$ Å, and $c = 7$ Å and one molecule per unit cell. Only nearest neighbor interactions with $\varepsilon_a = 100$ meV, $\varepsilon_b = 50$ meV, and $\varepsilon_c = 20$ meV are taken into account which lead to a tight-binding band energy of $\varepsilon(\mathbf{k}) = -2\varepsilon_a \cos(\mathbf{k}\mathbf{a}) - 2\varepsilon_b \cos(\mathbf{k}\mathbf{b}) - 2\varepsilon_c \cos(\mathbf{k}\mathbf{c})$. The electron-phonon interaction is modeled by a dispersionless optical mode according to the Einstein model which is characterized by a phonon energy of $\hbar\omega = 10$ meV and a coupling strength of $g = 1$. In order to calculate the mobility contributions in Eqs. (4.42) and (4.52), one has to specify the static disorder which is expressed in the energy $\hbar/\tau = 0.1$ meV, which is a low value representing ultrapure crystals.

5.1.1 Coherent Transport

Temperature Dependence It is instructive to visualize the coherent part of the mobility first. The temperature dependence of $\mu^{(coh)}$ is plotted in Fig. 5.1. It shows a strong decrease with rising T, which reflects strong band narrowing effects for the assumed coupling. Importantly, there is a pronounced difference between the present theory (solid lines) and the narrow-band theory (dashed lines) for low temperatures (see Fig. 5.1 (b)). The values in the present theory are finite in the $T \rightarrow 0$ limit in contrast to the narrow-band theory which suffers from a $1/T$ divergence. The removal of the $1/T$ singularity in the present theory, as discussed in Sec. 4.3.2, is achieved by the correct description of the quantum statistics of the carriers and is a great strength of the theory. For elevated temperatures the mobilities of the full and narrow-band theory approach each other and give identical curves at high T
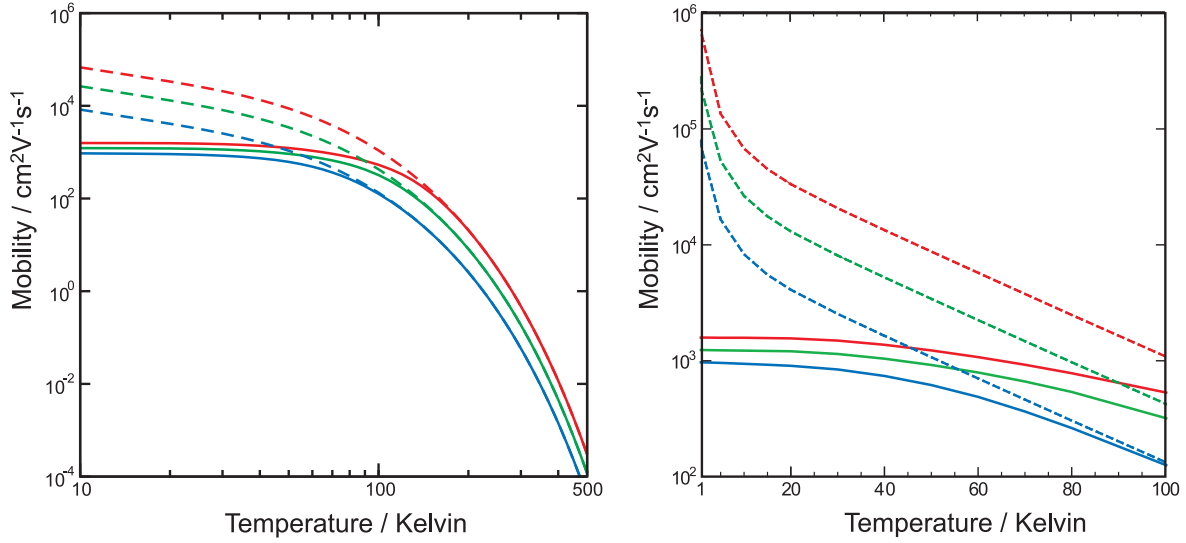
Figure 5.1: Band mobility $\mu^{(coh)}$ from model system along directions a (red), b (green), and c (blue). Solid lines represent the present approach. Dashed lines are obtained within the NBA. Left: logarithmic T scale. Right: linear T scale.

indicating that the NBA is a good approximation for high T (see also Sec. 4.3.1).

For low temperatures, the mobilities from the present theory approach constant values, which are visible as plateaus in Fig. 5.1. The length of the plateaus depends mainly on the phonon energy of the scatterer and its relation to $k_B T$. It is noteworthy that the temperature dependence, apart from the low-T plateau, is decreasing exponentially. This reflects the narrowing aspect of band transport. The strong decrease with rising temperature indicates a possible sharp transition from mainly coherent to predominantly incoherent carrier motion.

A mobility decrease is also observed experimentally in some cases, and it is often concluded that band transport is observed. However, the T-dependence of all measured mobilities, e.g., Fig. 2.1 for naphthalene but also for inorganic crystals (like Ge, Si, GaAs, etc.) [59–61], never follow an exponentially diminishing behavior as in Fig. 5.1 but obey a less strong decreasing $T^{-\gamma}$ power-law. In Sec. 5.1.3 the reader will see that such a measured power-law decrease can be explained if additional incoherent transport processes are included.

Wide-Band–Narrow-Band Transition   The validity range of the NBA for coherent transport can be estimated from Fig. 5.1 (a). Only if the temperature exceeds a threshold temperature both theories give identical results. From Fig. 5.1 (b) one can conclude that the NBA does not hold for smaller T. This figure shows this region more closely and demonstrates the failure of the NBA for low T. The mobilities from the narrow-band theory diverge in this limit independent of the strength of electron-phonon interaction. The removal of the singularity is a key result of the present theory (see Sec. 4.3.2).

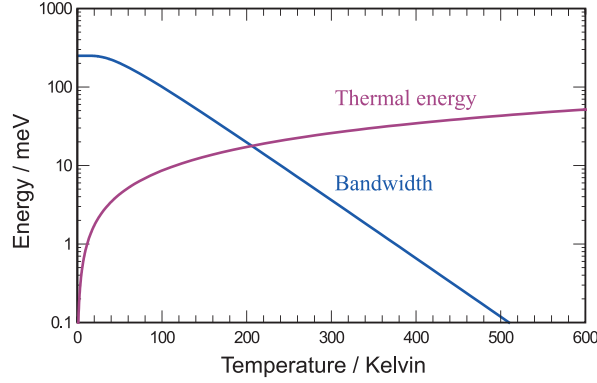The low-T and high-T regimes are seperated by a threshold temperature T_c. One can

Figure 5.2: Temperature dependent bandwidth of the model crystal vs. thermal energy $k_B T$.

identify from Fig. 5.1 that this threshold temperature is somewhat below 200 K. The particular value depends on material parameters like the strength of the electron-phonon interaction. There is also a dependence on the direction observable in Fig. 5.1, a refined discussion of which is given at the end of this section. Given a value of $T_c = 200$ K, one can compare the polaron bandwidth below and above this temperature. For $T > T_c$ the polaron bandwidth can be regarded small and the narrow-band approximation holds, while this is not the case for lower temperatures. Figure 5.2 shows the temperature dependent bandwidth of the model crystal as calculated from Eq. (3.45). Note that the bare hole bandwidth of 680 meV is strongly reduced already at $T = 0$ K to 250 meV due to zero point fluctuations. At $T = 200$ K the bandwidth is further reduced to 20 meV. It follows that, for $\mu^{(coh)}$ in this model crystal the NBA is a good approximation if the polaron bandwidth is smaller than 20 meV. Although the bare electron bandwidth is on the order of 1 eV and is hence much larger than $k_B T$, E_p, or $\hbar\omega$ in the computations, the polaron bandwidth is small enough to justify the narrow-band approximation. The question arises to which of the above quantities the polaron bandwidth has to be compared for a formal definition of T_c?

From the discussion in Sec. 4.3.2 it gets obvious that the thermal smearing of the polaron energies in the low-T limit is expressed in the term $n_{\mathbf{k}}(1 - n_{\mathbf{k}})$. Already for temperatures slightly above absolute zero one can replace $n_{\mathbf{k}}(1 - n_{\mathbf{k}}) \to n_{\mathbf{k}} \approx e^{-\frac{\tilde{\varepsilon}(\mathbf{k}) - \zeta}{k_B T}}$ because of the low carrier concentration of $c = 10^{-8}$. With further increasing T, $e^{-\frac{\tilde{\varepsilon}(\mathbf{k}) - \zeta}{k_B T}}$ approaches the constant c if the polaron bandwidth B_{pol} is smaller than $k_B T$, which is the case where the NBA holds. Thereby, the transition temperature T_c may be defined as

$$k_B T_c = B_{pol}(T_c) \tag{5.1}$$

This corresponds nicely to the crossing of the curves in Fig. 5.2.

A refined discussion of this effect takes the effective *directional* bandwidth into account,
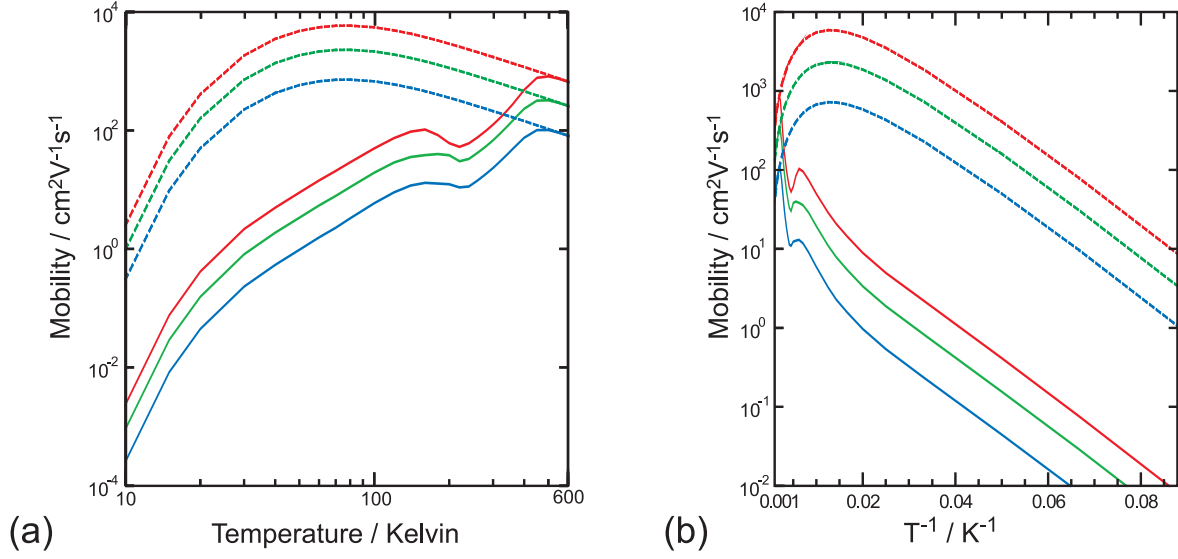
Figure 5.3: Hopping mobility $\mu^{(inc)}$ for model crystal along directions a (red), b (green), and c (blue). Solid lines represent the present approach. Dashed lines are from narrow-band approximation.

which (according to a one-dimensional tight-binding expression) may be defined as $B^x_{pol} = 4\widetilde{\varepsilon}_x$, where x denotes the Cartesian direction. The definition of T^x_c, is given implicitly as the temperature for which

$$k_B T^x_c = B^x_{pol}(T^x_c) \tag{5.2}$$

holds. Since B^x_{pol} depends linearly on the transfer integral ε_x, the transition temperature for the c direction (lowest transfer integral) is below the transition temperature for the b direction. It follows that $T^c_c < T^b_c < T^a_c < T_c$. This is also observed in the simulations.

5.1.2   Incoherent Transport

Temperature Dependence   Figure 5.3 shows the hopping contribution $\mu^{(inc)}$ to the total mobility for both narrow-band theory and new approach. The curves behave very differently unless the temperature exceeds 500 K. For low T, an increase of the mobilities with rising temperature is observed in both theories. However, the new theory gives values that are three orders of magnitude below the values from the narrow-band approach.

A plot of the mobility against the inverse temperature (see Fig. 5.3 (b)) reveals the activation aspect of the incoherent transport with a Boltzmann factor $e^{-\frac{E}{k_B T}}$. This finding is expected from the discussion in Sec. 4.3.2 and corresponds to Eq. (4.58). The activation energy E, as obtained from a fit of Eq. (4.58) to the low-T region of the plot in Fig. 5.3 (b), equals the phonon energy $\hbar\omega$ of the coupling mode. Note that this barrier for the low-T hopping is not the polaron binding energy E_p from Eq. (4.62). Rather it is the phonon energy $\hbar\omega$ because a phonon absorption process is needed to move the charge. This becomes clear since the final state energy $\widetilde{\varepsilon}_2$ (for empty states) is larger than the initial state energy

$\widetilde{\varepsilon}_1$ (for occupied states).

Another impression from Fig. 5.3 is that the curves in the new approach exhibit much more fine structure than the narrow-band theory. I shall discuss the main features of the present theory. The increase of the mobilities at low T is interrupted by a temperature interval between $T_1 = 150$ K and $T_2 = 500$ K where a dip in the curves is observed. A hint on the mechanism is given by the relevant temperatures T_1 and T_2. T_1 is somewhat below the threshold temperature T_c, which is relevant for the coherent part of the transport, and T_2 is well above T_c. According to the comparison to the results from the narrow-band theory, T_2 is the temperature above which the NBA gets exact. The width of the polaron band should therefore not only be compared to the thermal energy $k_B T$ as in the definition of T_c in Eq. (5.1) but also to other characteristic energies such as the phonon energy $\hbar\omega$ or the disorder energy $\hbar/\tau$.

Formally, one can define a temperature T_ω at which the bandwidth is reduced to the phonon energy, i.e., $B_{pol}(T_\omega) = \hbar\omega$, and which may be related to the observed temperature T_1. Whether the temperature is below or above T_ω is strongly relevant for the scattering channels contributing to the mobility. For $T < T_\omega$ the bandwidth is larger than $\hbar\omega$ and, hence, phonon absorption and emission processes are possible because the phonon energy can be compensated by the energy difference of initial and final states $|\widetilde{\varepsilon}_1 - \widetilde{\varepsilon}_2| \leq B_{pol}$. On the other hand, for $T > T_\omega$ creation or annihilation of a single phonon during a scattering process is not possible since the energy difference $|\widetilde{\varepsilon}_1 - \widetilde{\varepsilon}_2|$ cannot exceed the reduced bandwidth $(B_{pol}(T_\omega) < \hbar\omega)$. An increase of the temperatures across T_ω therefore closes such transport channels and only elastic processes $(\widetilde{\varepsilon}_1 - \widetilde{\varepsilon}_2 = 0)$ remain possible, e.g., the simultaneous creation and annihilation of phonons (two-phonon process) with the same energy. In the absence of the inelastic scattering channel, the mobility is reduced which causes the observed dip between T_1 and T_2. T_1 can therefore be related to T_ω.

The second characteristic temperature $T_2 = 500$ K is also derived from the polaron band narrowing. Beyond this value the NBA is a good approximation for $\mu^{(inc)}$ as seen in Fig. 5.3. This temperature for the incoherent mobility is much larger than $T_c = 200$ K for the coherent contribution. Why is this?

According to Fig. 5.2, the characteristic temperature of 500 K corresponds to a reduced bandwidth of 0.1 meV which is the same value as $\hbar/\tau$ assumed for the purity of the crystal. In order to understand this, one has to consider the open transport channels at such large T. These are are only elastic ones $(\widetilde{\varepsilon}_1 = \widetilde{\varepsilon}_2)$ because the bandwidth is much smaller than $\hbar\omega$, i.e., only those processes contribute, where the sum of all contributing phonon energies is zero. As a consequence, initial and final states have to match in energy within the assumed broadening, i.e., $|\widetilde{\varepsilon}_1 - \widetilde{\varepsilon}_2| < \hbar/\tau$. For a large bandwidth this condition is rarely fulfilled since initial and
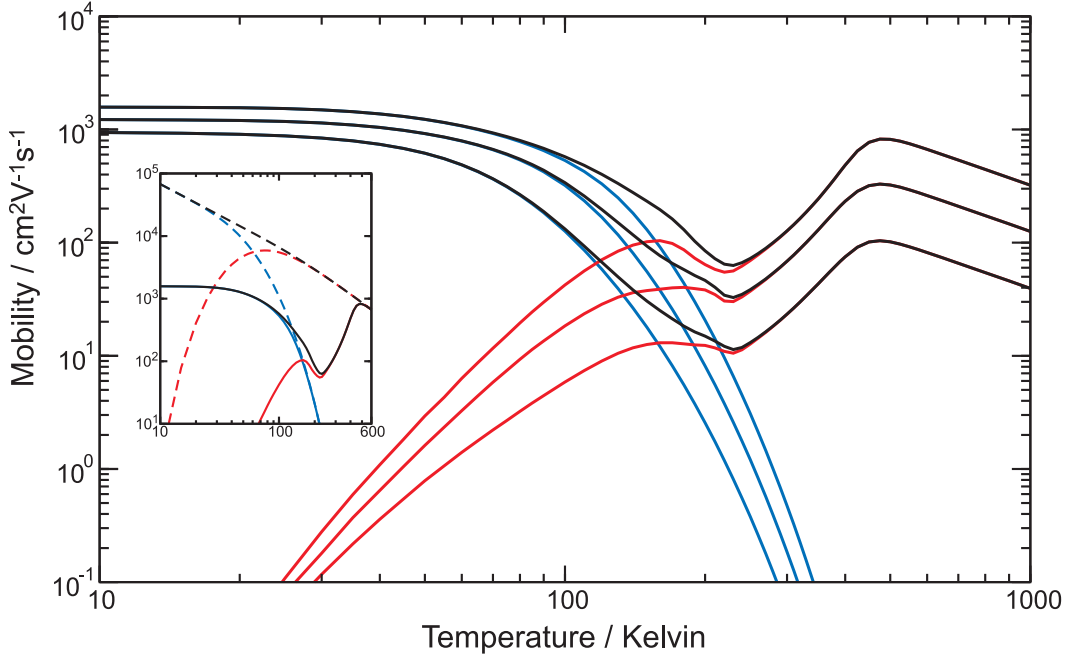
Figure 5.4: Hopping mobility (red), band mobility (blue) and total mobility (black) of model crystal. Different directions are plotted a, b, and c in order of decreasing mobility. Inset: Solid lines represent the present approach. Dashed lines are narrow-band approximation. Only a axis plotted.

final states are distributed over the whole band. In contrast, for bandwidths $B_{pol} < \hbar/\tau$, the difference $\Delta\widetilde{\varepsilon} = \widetilde{\varepsilon}_1 - \widetilde{\varepsilon}_2$ is always within $\hbar/\tau$ of the relevant mode energy (zero). In conclusion, the spectral width of the scattering cross section at $\Delta\widetilde{\varepsilon} = 0$, which is given by the disorder parameter τ and corresponds to an energy $\hbar/\tau$, determines the narrow-band limit of the incoherent contribution to the mobility.

A similar dip in the mobility has been observed previously in literature. The description was based upon the Boltzmann equation which is perturbative in the electron-phonon coupling g. [36] The explanation of the authors is based on a band occupation effect (with a constant bandwidth) giving rise to longer scattering times in average which change the otherwise decreasing temperature dependence of the band mobility. This is only partly related to the above analysis, because the important band narrowing was not included in Ref. [36] and also the hopping motion is not covered by the Boltzmann equation.

5.1.3 Total Mobility

The sum of coherent and incoherent mobilities gives the total mobility (cf. Eq. (4.39)). A detailed plot for the model crystal is depicted in Fig. 5.4. In general, the total mobility in the new approach is reduced compared to the narrow-band theory (see inset of Fig. 5.4). The reason is that the energy of the electronic levels is taken care of more precisely within the present theory. This results in a proper treatment of the energy conservation in the
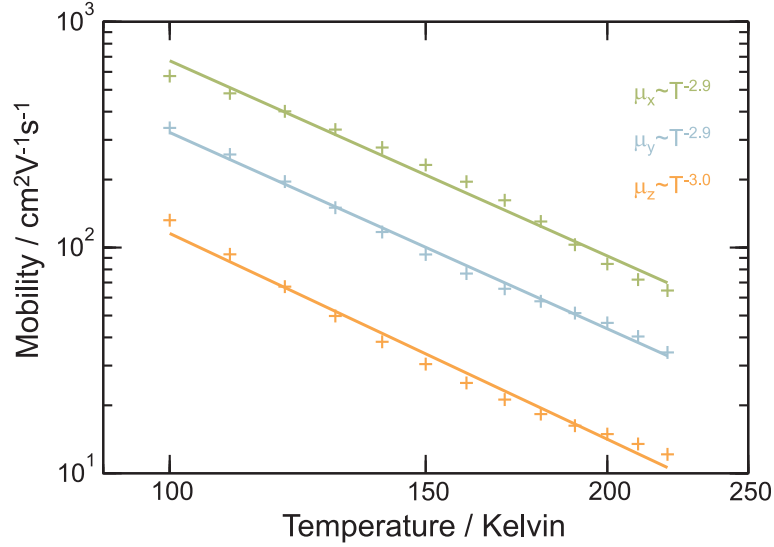
Figure 5.5: Total mobility (crosses) of model crystal along a, b, and c direction. Solid lines are $T^{-\gamma}$ power-law fits to the mobilities.

contributing scattering events. As a consequence, events for which the energy conservation is not fulfilled no longer contribute to the current and, hence, to the mobility.

For low temperatures, finite values are obtained since the dominating coherent contribution yields finite results in the $T \to 0$ limit. For high temperatures, i.e., $T > \max\{T_c, T_2\}$ the total mobility in the new approach equals the values from the narrow-band approximation. The intermediate temperature interval is of considerable importance since temperatures around and below room temperature are easily accessible by experiment. Hence, experimentally measured mobilities often cover temperatures between 100 K and room temperature. For such temperatures one often observes a power-law dependence of the mobility in ultrapure crystals. In order to investigate the new theory for such a characteristic, I plotted the mobility for temperatures between 100 K and 220 K in Fig. 5.5.

It is obvious that the mobilities exhibit a $T^{-\gamma}$ power-law dependence for temperatures in this domain. The exponents γ are very similar among the directions between 2.9 and 3.0 and only small deviations from the power-law curvature are observed. Similar exponents were observed for hole mobilities in naphthalene (cf. Fig. 2.1) which shows that the model crystal is close to a real system. The power-law behavior was not present separately for either the band mobility (black in Fig. 5.4) nor the hopping mobility (blue in Fig. 5.4) but only for the sum of both contributions. Additionally, the temperature range where the power-law dependence is observed exactly coincides with the transition temperature from band to hopping transport (see Fig. 5.4). Both facts lead me directly to the conclusion that this power-law dependence is a direct consequence of the interplay of both mechanisms and cannot be attributed to either contribution separately. It follows that the exponent γ results
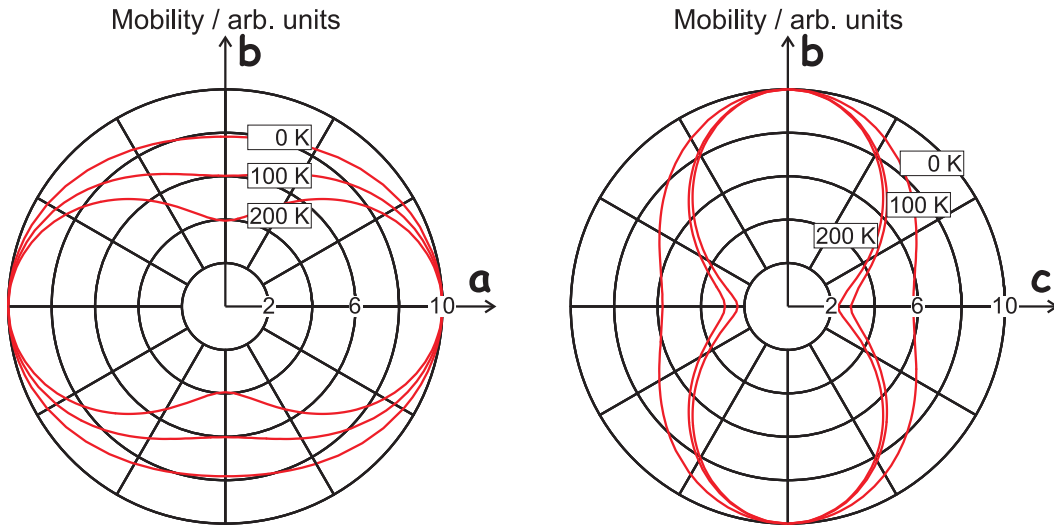
Figure 5.6: Direction dependence of the band mobility in the ab-plane (left) and bc (right). In both graphs, the maximum in-plane mobility is normalized to 10 for each temperature.

from the relative magnitude of each of the contributions. This is studied in more detail in Sec. 5.3.

5.2   Mobility Anisotropy

Coherent Transport   Another important effect that can be observed is the change in the mobility anisotropy with increasing temperatures. For high T, such a temperature dependent anisotropy has been discussed in literature theoretically [33, 44] and has been observed experimentally [20]. Also at low T, such an effect is now described in the present theory due to the improved description of the coherent transport. In order to illustrate the effect, I plotted the coherent mobility versus direction in polar plots in Fig. 5.6. The figure shows the mobility anisotropy with rising temperature from 0 K to 200 K within the ab plane (left) and within the bc plane (right).

For lowest T, there is a direction dependence for both planes (see curves for $T = 0$ K) which is expressed in the oval shape in the polar plots. Increasing the temperature to 100 K or even 200 K gives rise to a strong deformation of the oval form, i.e., the mobility anisotropy $\left(\frac{\mu_a}{\mu_b} \text{ or } \frac{\mu_b}{\mu_c}\right)$ gets stronger with higher T. Beyond 200 K there are only minor residual changes in the anisotropy, i.e., the curves at 200 K can be regarded as the high-T limit. What is probed with this analysis are the details of the band structure. Due to the low carrier concentration of $N_c/N_\Omega = 10^{-8}$, the carriers occupy for low T only the lowest states near the band edge. Only these carriers contribute to the current and hence to the mobility. Close to the band edge, the **k**-dispersion is parabolic in a very good approximation and the effective

mass m_x^* ($x \in \{a, b, c\}$) is calculated from the tensor [52]

$$\left[m_{el/hole}^{*-1} \right]_{ij} = \pm \frac{1}{\hbar^2} \frac{\partial^2 \varepsilon(\mathbf{k})}{\partial k_i \partial k_j}. \tag{5.3}$$

From a nearest neighbor tight binding expression ($\varepsilon(k) = -2\varepsilon_x \cos(kx)$) one concludes that $(m_x^*)^{-1} \propto \varepsilon_x$. Consequently, following Eq. (2.4), the mobility anisotropy behaves like $\varepsilon_a/\varepsilon_b/\varepsilon_c$ for the various directions.[1] In contrast, for high T, where the polaron bandwidth is reduced, the carriers from the entire band contribute equally to the current because the width of the thermal smearing in $n_\mathbf{k}$ is larger than the polaron bandwidth, i.e., $k_B T > B_{pol}$, and the thermal average over the band velocity squared in Eq. (4.42) is proportional to the transfer integral squared (see definition of band velocity in Eq. (4.43)). Consequently, the mobility anisotropy is changed to $\varepsilon_a^2/\varepsilon_b^2/\varepsilon_c^2$, which is the same prefactor as for the incoherent mobility in Eq. (4.51). For the ab plane for example, this amounts to an additional factor with rising temperature of $\frac{\varepsilon_a}{\varepsilon_b} = \frac{100 \text{ meV}}{50 \text{ meV}} = 2$. This factor is visible in the left part of Fig. 5.6, where the anisotropy change is obtained from the reduction of μ_b relative to μ_a.

From the above discussion it is clear that the narrow-band theory, which neglects the details of the band structure at this point ($B_{pol} = 0$), is not able to describe this transition and the change in the anisotropy in the low-T region of Fig. 5.1.

One can also observe that the change in the mobility anisotropy occurs at different temperatures for the two planes depicted in Fig. 5.6. At 100 K it is not yet reached for the b direction but already for the c direction. Referring back to the discussion of the temperature dependence in Sec. 5.1.1, this is in accordance to the direction dependence of T_c, which describes the threshold temperature of the narrow-band transition.

The discussed change in the anisotropy does not influence the principle axes of the mobility tensor. These axes are unchanged for the model crystal since all off-diagonal tensor elements vanish. However, for a system with lower symmetry, e.g. monoclinic crystals as treated in a later chapter, this is not necessarily the case. Rather, one might expect a temperature dependent rotation of the tensor axes.

Role of Electron-Phonon Interaction Such a transition from linear to quadratic dependence of the mobility on the electronic coupling strength ε is not restricted to systems with large electron-phonon coupling nor is it caused by this coupling. Such a transition would also be observable for an inorganic narrow-band semiconductor with vanishing electron-phonon interaction for high enough T. However, in praxi, many inorganic semiconductors have bare bandwidths which exceed 1 eV. This makes the transition not visible for realistic tempera-

---

[1]The additional dependence on the lattice constants $a^2/b^2/c^2$, which is temperature independent, is not relevant in this discussion.
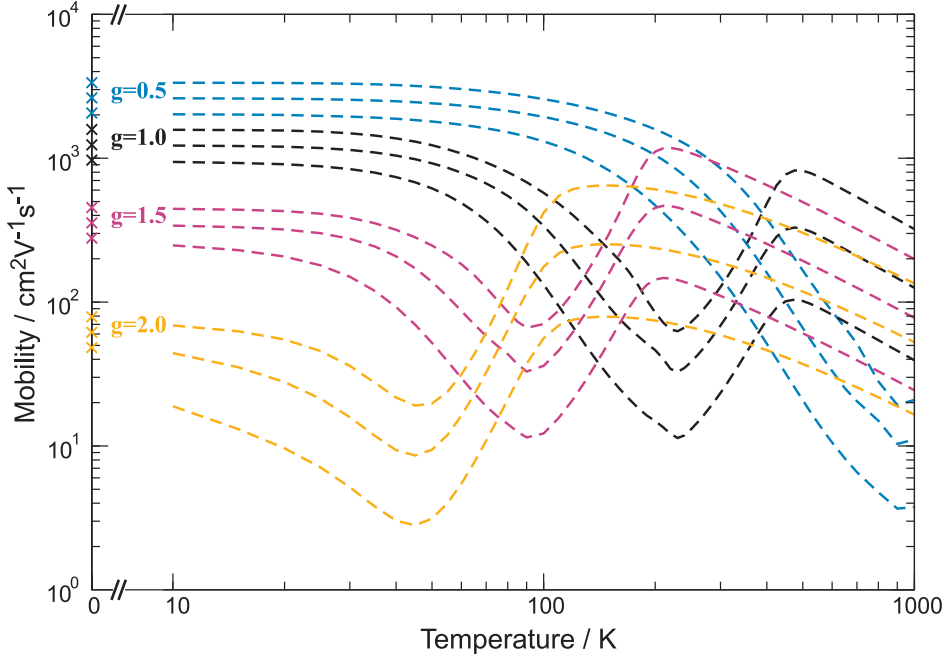
Figure 5.7: Total mobilities along the three Cartesian directions for each of the used coupling strengths g of electron-phonon interaction. The $T \to 0$ limit is indicated with crosses.

tures. The importance of the strong electron-phonon interaction in organic materials is to reduce the effective bandwidth to the order of $k_B T$ (see Fig. 5.2) and, therefore, to shift this transition into the observable temperature regime.

5.3   Variation of Electron-Phonon Coupling Strength

In order to further illustrate the strength of the present theory, I present and discuss some simulations with modified material parameters. This demonstrates the whole spectrum that is covered by the theory. In particular, the influence of the electron-phonon coupling is studied by keeping ε fixed and varying g. Assuming a high-purity and high-crystallinity sample ($\hbar/\tau$ =0.1 meV) one can simulate the limit of strong chemically bonded inorganic crystals for $g \leq 0.5$. Most of the technological relevant semiconductors behave like such small coupling crystals. The organic single crystals have intermediate values of approximately $g = 1$. [25] The other limit with very strong carrier-phonon interaction $g \geq 2$ may simulate even softer materials. Besides differences in the coupling parameters the different materials can be expected to differ also in their purity/crystallinity. This can be taken into account with the relaxation time τ, however, since the goal is to see the influence of the electron-phonon interaction and not of the purity, τ is kept fix. Figure 5.7 shows the total mobilities from Eq. (4.37) for optical modes with $g \in \{0.5, 1.0, 1.5, 2.0\}$. For each value of g three curves are plotted for the three principle axes of the mobility tensor.

Similarities One observes that the temperature dependence of the curves are isotropic apart from the above-discussed effect at low T. This holds for each of the values of g shown in Fig. 5.7. For low temperatures, the mobilities decrease, adopt a minimum, and increase again with rising T. As seen previously in Fig. 5.4, the minimum corresponds to a temperature directly above the band transport-to-hopping transition which is observed for all g, though at different T. A mobility maximum is reached for higher T, while for very high T the mobilities decrease again. The local maximum corresponds to the narrow-band transition temperature. Note that for all values of g such a behavior is observed. Only for the lowest coupling constants g is the latter part of the general characteristic (maximum) not seen in Fig. 5.7 since the necessary temperature exceeds the temperature range of the plot. Such large temperatures may be of academic use only. Importantly, however, one can conclude that the qualitative behavior of the mobility curves is independent of the strength of electron-phonon coupling.

Differences The total mobilities for the low-T limit differ since the zero point vibration effects are stronger with larger g. These effects give rise to polaron binding and mass enhancement according to Eq. (4.57) and reduce the coherent contribution. In contrast to the strong variation with g for low T, which reaches a factor of about 42 between $g = 0.5$ and $g = 2$, the variation of the room temperature mobilities across different values of g is much weaker. Similarly, also the values of the maxima of the mobility curves vary only by a factor of 2. This may be discussed by help of the analysis of the relative contributions of both coherent and incoherent mobility. The reduction of the band mobility $\mu^{(coh)}$ for increased electron-phonon coupling g has been discussed above. The dependence of the hopping contribution $\mu^{(inc)}$ on g is more complicated. At low T it is found being proportional to g^2 (cf. Eq. (4.58)), while at high T it seems not to depend strongly on g as seen in the comparison of the mobility maxima in Fig. 5.7. If $\mu^{(inc)}$ does not depend on g or even increases with g and $\mu^{(coh)}$ is strongly reduced for larger g, the increasing electron-phonon coupling shifts the relative contribution of both parts towards $\mu^{(inc)}$. Consequently, for larger g the band-transport-to-hopping transition is observed at lower temperatures in Fig. 5.7.

Importantly, also the parameter γ for the temperature dependence $T^{-\gamma}$ below the mobility dips in Fig. 5.7 is changed as a consequence of the reduced coherent contribution for larger g. One finds that γ is lowered with stronger electron-phonon interaction. For $g = 1.0$ the average over the three directions yields $\gamma = 2.9$ (see also Fig. 5.5). For $g = 1.5$ one obtains $\gamma = 2.4$ (for 50 K $< T <$ 90 K), and for $g = 2.0$ one obtains $\gamma = 1.5$ (for 20 K $< T <$ 40 K). In agreement with this tendency, the exponent γ is raised for smaller electron-phonon coupling. For $g = 0.5$ one obtains $\gamma = 3.6$ in average (for 300 K $< T <$ 800 K). This is qualitatively

different to a previous finding in the high-T limit, where stronger electron-phonon interaction (e.g. due to additional phonon modes) leads to a larger exponents. [44] Here it is a direct consequence of the relative magnitudes of $\mu^{(coh)}$ and $\mu^{(inc)}$.

Silbey and Munn stated it was not clear why *"the smallest mobilities tend to show an activated behavior, intermediate ones [a] weak temperature dependence ..., and larger ones a more rapid decrease like T^{-n} with $n = 2.5 - 3$"* [32], as observed in Ref. [62]. An answer is evident from the findings in this section. The stronger the electron-phonon interaction, the more $\mu^{(inc)}$ dominates over $\mu^{(coh)}$ and γ is reduced. For even larger g and, hence, stronger thermal disorder this would lead to an activation behavior which may be described exclusively with the incoherent mobility alone. A similar effect might also be expected for stronger static disorder.

Experimentally Accessible Temperatures Figure 5.7 displays the carrier mobilities over a large temperature range which allows for the analysis of the overall T dependence. Such a large temperature interval, however, is very often not observable in experimental measurements. For organic molecular crystals typical temperature windows for mobility measurements are between 100 K and 300 K but often the published curves do not even reach below 200 K. With such a limited experimentally observable temperature range, the results are very difficult to interprete. For instance, it would be difficult to recognize that the mobilities of crystals with different scattering strength g obey the same general behavior but only for different temperatures, as discussed previously in this section. For the $g = 0.5$ curves (blue in Fig. 5.7) one would clearly anticipate band transport while for the $g = 2.0$ curves (orange in Fig. 5.7) similar behavior (decreasing $\mu(T)$) is observed above 100 K but the reason is very different. On the other hand for the curves with $g = 1.5$ and $g = 1.0$, a thermally activated transport mechanism would be assumed from increasing $\mu(T)$ curves. These considerations give a hint how difficult a correct interpretation of the mobility curves may be, when only a limited temperature interval can be observed properly.

Chapter 6

Ab initio Studies of Charge Transport in Crystalline Structures

6.1 Computational Methods

6.1.1 Total Energy Calculations and Structural Relaxation

In order to determine the total energies of the crystals under study and their minimum with respect to the atomic coordinates, I employ the density functional theory (DFT) code VASP. [63, 64] The projector augmented wave (PAW) method [65] is used for the description of the electron-ion interaction. These methods are also applied to the studied gas-phase molecules. The wavefunctions in the interstitial region between the atomic cores are smooth and can be expanded into plane waves using a basis set up to a cutoff energy of 37 Ry. This value has been proven previously to give converged results for a variety of organic molecules. [66–68] It is carefully checked that the stress tensor is converged with respect to the energy cutoff. For test purposes the cutoff has been increased to 66 Ry where only small changes in the lattice constants were observed as one might expect for soft matter. The changes are of only minor importance.

In order to simulate the gas phase, i.e., a single molecule, within the above framework the supercell approach is used. Thereby the molecule is placed in an orthorhombic supercell and oriented perpendicular to the cell axes. In order to model the gas phase accurately, artificial interactions with neighboring cells have to be avoided. This is achieved when the distance between the molecules is large enough. Since the size of the supercell determines the vacuum region between a molecule and its images, a rather large cell of dimension $24 \times 22 \times 18$ Å^3 is used. For such large cells the dispersion of the energy levels in the (rather small) Brillouin zone is negligible and the **k**-space integration can be restricted to the Γ point. For crystalline phases larger Brillouin zones are encountered and a regular grid according to the Monkhorst-Pack scheme [69] is used for **k**-space sampling.

The geometry optimization for molecular and crystalline structures is conducted by help of a conjugate gradient algorithm minimizing the Hellmann-Feynman forces. Thereby, residual forces are relaxed below a very small value of 0.1 meV/Å.

6.1.2 Treatment of Exchange and Correlation

In order to compare the molecular and crystal properties in general, one has to model both the intramolecular and intermolecular interactions with equally high accuracy. This puts a high demand on the approximation of the exchange-correlation (XC) functional in DFT. Currently, there is no functional that meets this condition at acceptable computational costs. Many density functionals have been developed in the past years each of which has its own characteristics. Here, I apply the local density approximation (LDA), the generalized gradient approximation (GGA), and a semiempirical van der Waals corrected GGA (GGA+vdW).

For the LDA calculations, the parameterization of Perdew and Zunger is used. [70] For the GGA calculations, the PW91 functional [71] is employed in order to estimate the influence of the density gradient contributions to the XC energy which are not present in LDA. Improvements over LDA have been demonstrated for the simulation of strong hydrogen bonds [67, 72] and a variety of quantities such as cohesive energies. [73] However, it is also known that the GGA approach shows deficiencies for van der Waals (vdW) bonded systems like graphite, [74, 75] which is much better described in LDA. In particular for interacting molecules, the semi-local approximations for XC (such as GGA) fail to correctly account for the long-range attraction by vdW forces. Even if the impact on the intramolecular geometry or the electronic structure is weak, this directly affects the structure and energy of condensed systems in the computations. It was shown that a semiempirical correction to GGA can simulate this part of the correlation energy from strongly corrugated charge density profiles. [74–76] This GGA+vdW approach is based on additional nonlocal interaction from atom-atom potentials which vanish for small distances like the covalent bonding distance. GGA+vdW is tested for the durene crystals as an exemplary study of its performance for the molecular crystals.

6.1.3 Vibrational Properties

The determination of vibrations is based on the harmonic approximation of the total energy with respect to the deviation from the ground state geometry. This approach is justified since anharmonic effects such as the temperature dependence of the elastic constants are not of interest here. Without explicit symmetry considerations, each nuclear coordinate is displaced along each positive and negative Cartesian direction by a length δ. In the spirit of the adiabatic approximation, repelling forces are calculated as Hellmann-Feynman forces

linearly in δ. The resulting force constant matrix is derived from a central difference scheme in accordance with the harmonic approximation. This yields a generalized eigenvalue problem of dimension 3N (N number of atoms per unit cell). As a solution one obtains 3N eigenvectors representing intermolecular and/or intramolecular vibrations and 3N eigenvalues representing the corresponding frequencies at the Γ point. Note that, for the crystalline case both the intramolecular and intermolecular vibrations result from a single force constant matrix.

The displacement parameter δ is optimized to ensure harmonic motion on the one hand and to minimize numerical inaccuracies on the other hand for both the gas phase and the crystal phase. An important criterion for the quality of the simulations is the characteristics of the acoustic phonons at the Γ point, which are lattice translations with zero frequencies. The deviation from zero, which has been used as a target quantity for the determination of δ, is approximately 1 cm^{-1}. The resulting value of $\delta = 0.05$ Å is in accordance with earlier findings for other molecular systems. [77] In the case of modes which are numerically degenerate, the symmetry of the vibrations has been properly accounted for by means of an additional symmetrization procedure.

The calculated phonon modes and frequencies are also important ingredients for the calculation of the electron-phonon coupling parameters in Sec. 6.1.5.

6.1.4 Electronic Structure

Among the most important quantities of the electronic structure of organic molecular crystals are the bandwidths of the valence and conduction bands. These quantities or, in the language of the tight-binding theory [52], the corresponding transfer integrals are highly relevant measures for the charge-carrier mobility and contain information about its directional dependences as well as overall values. [25, 44] Another important quantity that can be obtained from band structure calculations is the fundamental band gap (also known as the transport gap). Additionally, the optical gap, which differs from the transport gap due to excitonic effects, is of interest for absorption spectra.

The fundamental band gap E_g is defined as [78]

$$E_g = IP - EA, \tag{6.1}$$

where the ionization potential IP and the electron affinity EA are the changes in the total energy upon electron removal or electron addition, respectively,

$$IP = E(N-1) - E(N), \tag{6.2}$$

$$EA = E(N) - E(N+1). \tag{6.3}$$

Figure 6.1: Illustration of the fitting procedure. The KS band structure (here for a durene crystal for example) in black is fitted by the tight binding band energy in red. See text for details.
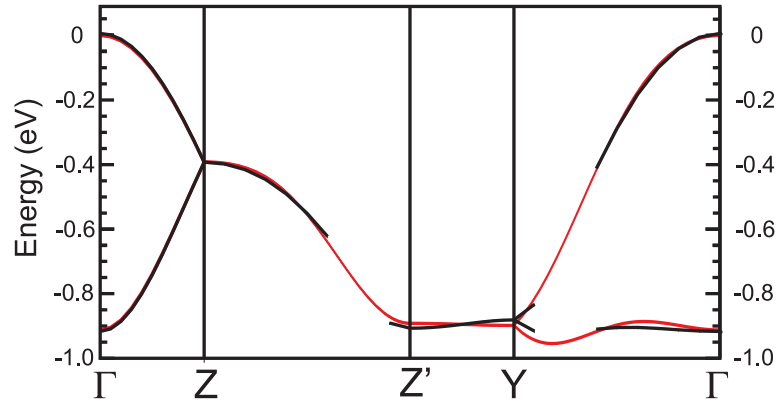
Here, $E(N)$ denotes the total energy of the N-electron system. This approach is called the "delta self-consistent field" (ΔSCF) scheme because it is based on three self-consistent calculations of electronic ground states. The ΔSCF approach works very well for single-particle and two-particle excitation energies of localized electronic systems, such as molecules. [66, 68]

It is important to stress that the quantity E_g as defined in Eq. (6.1) is not directly related to any single-particle eigenvalue of the Kohn-Sham (KS) equations [79, 80] because ground-state DFT calculations do not take into account quasiparticle effects. Nonetheless, for simplicity, the KS eigenvalues are often used for the discussion of the electronic structure of the systems under study. The energetic difference between the KS eigenvalues of the highest occupied molecular orbital (HOMO) and the lowest unoccupied molecular orbital (LUMO) defines the fundamental KS gap E_g^{KS}, which is usually smaller than the gap defined by Eq. (6.1). For crystalline solids, the KS eigenvalues are frequently used to discuss the band structure, motivated by the *a posteriori* observation that the energy dispersion of the individual KS bands is often more or less in agreement with experimental measurements. Here, the KS bands are used to estimate the bare electronic bandwidths in the crystals under study.

6.1.5   Material Parameters for Transport Theory

For the computational studies of transport properties, the analytical expressions in Secs. 3 and 4 are supplemented by the material parameters for the studied crystals. These material parameters are obtained from *first principles* DFT calculations. The computational part is performed using the Vienna ab-initio Simulation Package (VASP) [63, 64] code, the specifics of which have been described previously.

From the Kohn-Sham band structure one obtains the transfer integrals with the following procedure. The KS band structure is fitted by a tight binding expression to extract a set of transfer integrals which best reproduces the band structure. If there are two molecules per

unit cell, the tight binding expression for the energies of the two resulting bands reads

$$\varepsilon_{\pm}(\mathbf{k}) = M(\mathbf{k}) \pm S(\mathbf{k}) \tag{6.4}$$

where $M(\mathbf{k}) = \frac{1}{2}\left(F_{11}(\mathbf{k}) + F_{22}(\mathbf{k})\right)$ is the mean energy of the bands $\frac{1}{2}\left(\varepsilon_{+}(\mathbf{k}) + \varepsilon_{-}(\mathbf{k})\right)$ and $S(\mathbf{k}) = \sqrt{\left(\frac{F_{11}(\mathbf{k})-F_{22}(\mathbf{k})}{2}\right)^2 + |F_{12}(\mathbf{k})|^2}$ is the half splitting between the two bands. Thereby, the definition of the auxiliary function F_{ij} according to

$$F_{ij} = \sum_{\mathbf{R}} e^{i\mathbf{k}\mathbf{R}} \varepsilon_{ij}(\mathbf{R}) \tag{6.5}$$

is used and $\varepsilon_{ij}(\mathbf{R})$ is the transfer integral between orbitals i and j $(i, j \in \{1,2\})$ which belong, in general, to different unit cells (denoted by the difference vector $\mathbf{R}$ which is a Bravais vector in this case).[1] The sum in Eq. (6.5) runs over a set of nearest unit cells according to the observation that with increasing distance the transfer integrals diminish rapidly. The accuracy of the fit can therefore be increased if more neighbors are taken into consideration. One has to find the balance between complexity of the fit function with many neighbors and the required accuracy of the transfer integrals. The fit itself is performed on a regular mesh of grid points in the Brillouin zone. The complexity of the fit function is reduced by taking all symmetry operations into account.

In order to illustrate this procedure I plotted such a fit in Fig. 6.1. This example shows a part of the durene valence band structure (see Sec. 6.3.4 for the discussion of the electronic structure of durene) in black along with the fit function in red. Gaps in the KS bands in Fig. 6.1 are due to the removal of a second set of bands (see Fig. 6.2), which appear only slightly lower in energy. In order to identify both set of bands in Fig. 6.2, the orbitals have been investigated at each point in the Brillouin zone which, in most cases, coincide nicely in shape with the molecular orbitals. Accordingly, colored lines (red and blue) indicate bands derived from the HOMO and HOMO-1 of the durene molecule, respectively. There are a few points where both sets (red and blue) interact which cannot be described by a single orbital per site in the tight binding theory. Such crossing points, where the band deviates from the tight binding expression due to interaction with another band, are excluded from the fit procedure. With the fit procedure one obtains the values $\varepsilon_{ij}(\mathbf{R})$ representing the electronic structure of the geometric ground state.

Changes in the band structure occur for deformed lattices, e.g., when lattice vibrations are taken into account (deformation potential mechanism). According to Eq. (3.3) these

---

[1] The notation is changed here from the original ε_{MN} to $\varepsilon_{ij}(\mathbf{R})$ because the original quantities ε_{MN} have translational symmetry and depend only (i) on the difference vector $\mathbf{R}$ associated with the two unit cells to which the orbitals M and N belong and (ii) on the molecule indices i and j which label the molecules within a given unit cell.
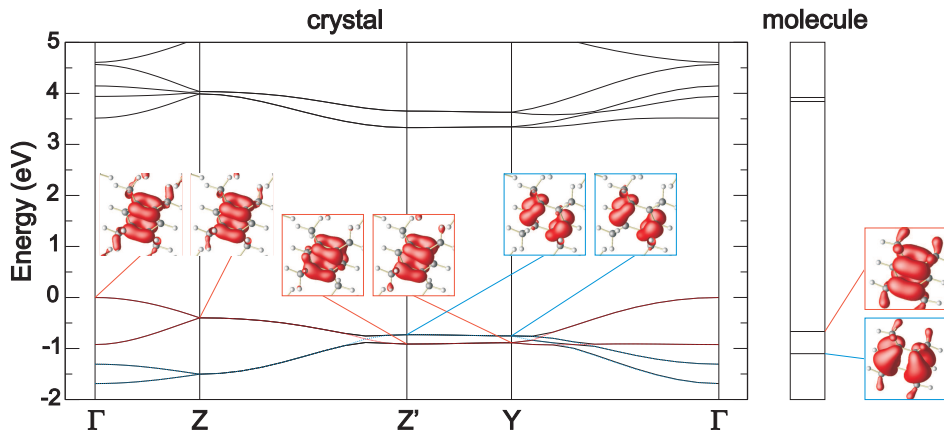
Figure 6.2: Selection of a pair of bands (red) which are derived from the molecular HOMO in the case of durene.

deformations modify the transfer integrals which is rationalized with the electron-phonon coupling. The coupling constants g_λ can therefore be obtained from the electronic structure of distorted lattices when the phonon eigenvector $\mathbf{e}_s^\lambda$ (see Eq. (3.6)) is used as a distortion. More precisely, the linear changes with the amplitude is measured and g_λ is obtained from Eq. (3.18). Again the fit function is simplified by symmetry operations. However, it is important to consider the symmetry of the mode which is not always equivalent to the symmetry of the crystal (A_g modes for durene) but can be lower (e.g. B_g modes, cf. Tab. 6.3).

6.2   Naphthalene

6.2.1   Introduction

After having discussed the features of the present theory in application to a model crystal in Chap. 5, I come back to the naphthalene crystal (see Fig. 2.2) which, as stated in Sec. 2.2, is an illuminating prototypical example for studies of the two transport mechanisms in OMCs. Its transport properties are very well characterized experimentally including electron and hole mobilities in various directions. High mobilities at low T and power-law-like T-dependencies have been interpreted as clear indications for band transport. [21] On the other hand, the temperature independence of the electron mobility in c^*-direction at high T can only be explained by hopping theories where thermally activated processes are considered. In order to address the question of the transport mechanism and the temperature dependence of the carrier mobility, the novel transport theory which has been developed in Chap. 4 is applied to the description of the carrier mobilities in naphthalene. This allows for the examination of its performance in the description of mobilities from a direct comparison to high quality measurements.

6.2.2 Charge Transport

It has been shown previously that the *electron* mobilities in naphthalene for elevated temperature (at least for the c^* direction) strongly depend on the inclusion of nonlocal electron-phonon interaction [31], which is not included in the derivation in Chap. 4. The influence of nonlocal interaction on the *hole* mobilities is not so strong and, therefore, I focus on the simulation of the positively charged carriers. The inclusion of nonlocal electron-phonon coupling in an effective coupling constant as in Eq. (3.44) can partially account for the influence of this type of coupling and has been taken into account in the simulation of the hole mobilities.

All necessary material parameters have been determined by *ab initio* calculations (see Table III in Ref. [25]). From this reference I use the values of $a = 7.68$ Å, $b = 5.76$ Å, $c = 8.35$ Å, and $\beta = 125.7°$ for the monoclinic lattice, the three intermolecular phonons as scatterers, as calculated at the Γ point, with energies $\hbar\omega_\lambda = 10.7$, 14.2, and 17.4 meV, and effective coupling constants $\frac{G_\lambda}{2} = 0.36$, 0.32, and 0.16, respectively. These effective coupling constants take also nonlocal electron-phonon interaction into account. In principle, besides the intermolecular optical modes also the acoustic modes and all intramolecular modes have to be included. According to Eq. (3.41) and the accompanying discussion (i.e. the treatment of the **q** dependence of the electron-phonon coupling which is modeled using the coupling constants at Γ) one has $G_{acoustic} = 0$, which is the reason for the neglection of the acoustic modes as in previous literature [31]. The remaining intramolecular modes have larger phonon energies and, hence, smaller coupling constants, which may be expressed as $G_\lambda \propto \omega_\lambda^{-3}$ (see Eq. (3.18)). This reduces their influence on the absolute value of the mobility. In addition thereto, due to the very low occupation numbers, their effect on the temperature dependence of the mobility can be neglected.

The transfer integrals $\varepsilon_{ij}(\mathbf{R})$ amount to $\varepsilon_a = -29$, $\varepsilon_b = -59$, $\varepsilon_c = 4$, and $\varepsilon_{ac} = 6$ meV for the directions $\pm\boldsymbol{a}$, $\pm\boldsymbol{b}$, $\pm\boldsymbol{c}$, and $\pm(\boldsymbol{a}+\boldsymbol{c})$, respectively for equivalent molecules ($i = j$), and to $\varepsilon_{ab} = 17$ and $\varepsilon_{abc} = -24$ meV for the directions $\pm(\boldsymbol{a}/2\pm\boldsymbol{b}/2)$ and $\pm(\boldsymbol{a}/2\pm\boldsymbol{b}/2+\boldsymbol{c})$, respectively for inequivalent molecules ($i \neq j$). In accordance with previous calculations [31], I choose a small static disorder $\hbar/\tau = 0.1$ meV for ultrapure crystals and assume a low carrier concentration of $N_c/N_\Omega = 10^{-8}$.

The numerical results are plotted in Fig. 6.3 in comparison to experimental data [20] together with the mobilities as obtained within the NBA. All graphs show hole mobilities along the crystallographic directions a, b, and c^* (perpendicular to a and b). The ab plane is the herringbone stacking plane of the naphthalene crystal.

For low temperatures, an important observation is that the mobilities are finite in the low-T limit within the present theory, whereas the NBA suffers from a $\frac{1}{T}$ divergence. Moreover,
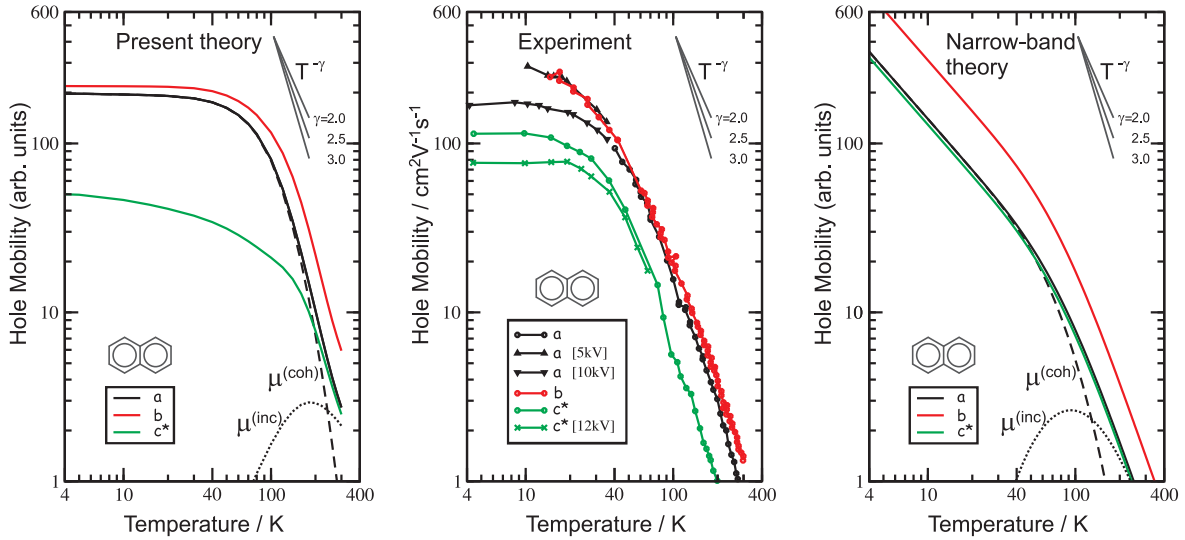
Figure 6.3: Anisotropy and temperature dependence of naphthalene hole mobilities in the new approach (4.37) (left) and within the narrow-band approximation [31] (right) compared to experimental data [20] (middle). Lines in the experimental data are guides to the eye. In a and c^* direction, the upper experimental curve corresponds best to the low-field limit (see text). Theoretical mobilities are decomposed with respect to coherent (dashed line) and incoherent (dotted line) contributions for the a direction.

the mobilities for low temperatures exhibit a plateau-like behavior, which is also seen in the experimental curves. This constitutes a strong improvement of the matching of simulated and measured mobilities. For high temperatures the calculated mobilities in the present theory exhibit the same temperature dependence as found in the experiments. They are best represented by a $T^{-\gamma}$ power law with γ of 3.3, 3.1, and 2.7 in a, b, and c^* direction, respectively. This is close to the values obtained in the measurements, where power-law fits yield exponents of $\gamma = 2.9$, 2.5, and 2.8, respectively.

Comparing the direction dependence of the theoretical and experimental mobilities, it is found that the correct ordering is obtained for both the present theory and the narrow band theory. In general, the highest hole mobilities in naphthalene are observed within the herringbone plane (ab plane). This is in accordance to the picture of strongest overlap of molecular orbitals in herringbone-stacked systems, which will be discussed in more detail in Sec. 6.3 for the case of durene crystals. However, one observes that the present theory and the narrow-band theory disagree quantitatively on the mobility anisotropy. While the present theory predicts a rather isotropic in-plane mobility $\mu_a \approx \mu_b$ and a significant lower mobility in c^* direction for low T, the narrow-band theory obtains very similar results for μ_a and μ_{c^*} independent of the temperature. From the experimental curves in Fig. 6.3 it is evident that the present theory performs much better also for the anisotropy, because the experiments find very similar mobilities in a and b direction as well. Note that the calculated mobilities in a direction should be compared to the upper black experimental curve at low T where

hot-carrier effects (lower μ for higher fields [45]) are reduced. For the same reason the upper green curve represents best the low-field limit for μ_{c*} in the computations.[2] The anisotropy ratio $\frac{\mu_a}{\mu_{c*}}$ for the low-T limit of the present theory is 4 and better matches to a value $\frac{\mu_a}{\mu_{c*}} = 3$ in the experiments than the narrow-band result for which basically no anisotropy is obtained ($\frac{\mu_a}{\mu_{c*}} = 1$).

Although the novel theory improves the description of the temperature dependence and the mobility anisotropy, the agreement between the new approach and the experiment is not perfect. The length of the above-discussed plateau is somewhat overestimated, which might be due to the treatment of acoustic phonons ($G_{acoustic} = 0$) since the length of the plateau is related to possible scatterers with lower phonon energies than for the three optical modes taken into account. A study on acoustic phonons has not been considered during this thesis because the role of these phonons has not yet been established in literature. [22] The reason might be that the description of the $\mathbf{q}$ dependence of the electron-phonon coupling of acoustic phonons is considerably more difficult. With rising temperature, the theoretical values of μ_a deviate stronger from μ_b and come closer to the values for μ_{c*}. This is a result in accordance to the narrow-band limit and can be understood from the comparison to the curves from the narrow-band theory. In experiment the deviation between μ_a and μ_b for higher T is less strong, though present as well.

In order to investigate the transport mechanism, a resolution of the mobility according to $\mu = \mu^{(coh)} + \mu^{(inc)}$ has been plotted in Fig. 6.3 for the a direction. It shows that band transport dominates at low T but is strongly reduced at high T. In particular at room temperature, band transport is found to contribute only 4% (narrow-band theory) or 22% (present theory) to the total mobility.

In summary, the present theory is not only applicable to model studies but can be successfully applied to the prototypical naphthalene crystal as well. It was found that it gives a significantly improved description of the hole mobilities in naphthalene for low and medium temperatures. This is observed for both the temperature dependence and the mobility anisotropy. For high T, the anisotropy of the previous narrow-band mobilities is recovered.

6.3 Durene

6.3.1 Introduction

The durene molecule is derived from the benzene molecule by substitution of four hydrogen atoms with four methyl groups. According to the IUPAC nomenclature its chemical name

---

[2]Unfortunately some data points for highest mobilities at 4 K were not reported but the existence of a small plateau is evident from all the data in the reference.
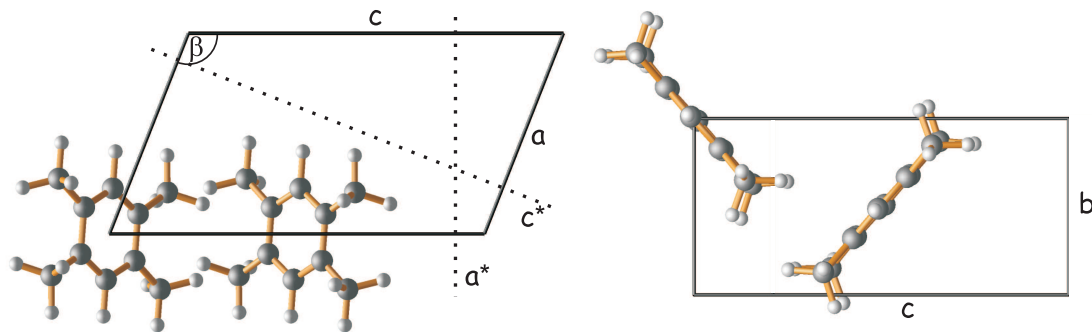
Figure 6.4: Durene in monoclinic crystal structure. The lattice vectors $\boldsymbol{a}$, $\boldsymbol{b}$, and $\boldsymbol{c}$ define the unit cell and β is the monoclinic angle. Top view along monoclinic b direction (left) and side view along $\boldsymbol{a}^*$ (right).

is 1,2,4,5-tetramethylbenzene. Durene exhibits D_{2h} point group symmetry. The crystalline phase of durene belongs to the space group $P2_1/c$ (C_{2h}^5) with two molecules in a monoclinic unit cell. The structure is depicted in Fig. 6.4.

The crystal structure is known from x-ray and neutron diffraction studies. [81, 82] Recently, inelastic neutron scattering (INS) experiments have been performed by Plazanet *et al.*, and a comparison with computed spectra has been made. [83] Early studies of the vibrational properties of durene crystals were carried out applying Raman spectroscopy. [84, 85] In a very recent study, INS, Raman, and infrared (IR) spectra have been recorded. [86]

Durene crystallizes in a herring-bone geometry like naphthalene. Although quite high carrier mobilities have been reported for durene long ago [39] it has remained relatively unattended by the organic electronics community. The confirmation of the reported high mobilities [87] was motivation enough to study this system theoretically. An additional advantage of durene in an *ab initio* study is the smallness of the molecules and the elementary cell which reduces the computational effort. There was only a single theoretical work about durene in literature by Plazanet *et al.* which aimed at the simulation of measured INS spectra. [83] A full characterization from a relaxed geometry, however, was missing. Consequently, such a characterization of the theoretical ground state geometry, vibrational properties as well as the electronic bandstructure is conducted prior to a study on charge transport.

The study on durene is presented as follows. Basic geometric properties can be found in Sec. 6.3.2. Therein, an analysis of three exchange-correlation functionals for the structural properties provides the basis for subsequent studies on durene and other OMCs. An investigation on vibrational properties follows in Sec. 6.3.3. Section 6.3.4 contains the study on electronic properties which focuses on the evolution of the band structure, i.e., the structure/property relationship is examined. The computations of charge transport-related quantities is compiled in Sec. 6.3.5. It includes the temperature-dependent polaron bandwidth and the mobility tensor of the charge carriers. The origin of the T dependence of the mobility
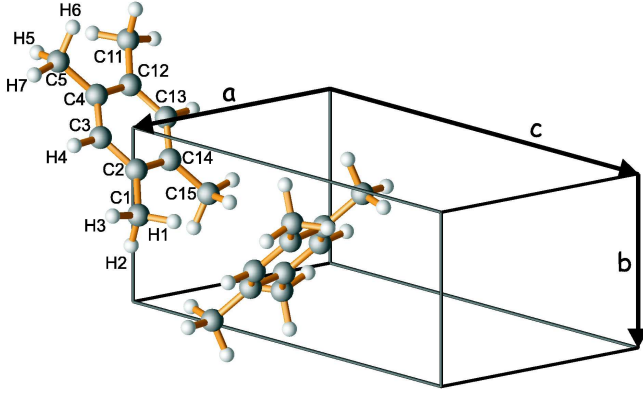
Figure 6.5: Nomenclature for carbon (C) and hydrogen (H) atoms in durene crystals.

Table 6.1: Lattice constants a, b, c (Å) and monoclinic angle β (°) for the durene crystal in different approximations for XC and experimental reference data from Ref. [83].

	LDA	GGA	GGA+vdW	Exp.
a	6.432	7.497	5.765	6.817
b	5.258	6.000	4.316	5.578
c	11.200	12.790	11.614	11.505
β	111.5	113.1	111.0	112.9

curves is discussed, and the anisotropy of the mobility is analyzed in detail. I put a special focus on the relationship between crystal packing geometry, molecular wavefunction overlap, and charge transport properties. The results include a visualization of the transport channels in durene which can be regarded as a prototypical herringbone-stacked crystal.

6.3.2 Geometric Structure

Based on the experimental findings for structural properties, the ground state geometry is obtained in a structural relaxation as described in Sec. 6.1.1. Thereby, unit cell parameters and atomic coordinates of crystalline durene, as obtained from neutron diffraction measurements, [83] serve as initial coordinates. In the ionic relaxation (total energy minimization), both the lattice parameters and the atomic basis are optimized. The symmetry is kept fix in the space group $P2_1/c$ (C_{2h}^5). The Brillouin zone is sampled using a grid dimension of 8×8×4. The structural relaxation is performed with different descriptions for exchange and correlation, namely, the LDA, GGA, and GGA+vdW approaches (see Sec. 6.1.2). The results for the lattice structure and molecular geometry are compared in Tabs. 6.1 and 6.2, respectively. In addition to the computational results, the experimental values [83] are reported as well for comparison.

One observes differences in the lattice parameters for durene across the used XC functionals. The values for the monoclinic angle β vary only between 1-2 degrees, while for the lattice constants a, b, and c, differences of up to 20% are found (cf. Tab. 6.1). Among

Table 6.2: Intramolecular bond lengths (Å) for the durene crystal. Root mean square (rms) value with respect to the experimental reference [83].

	LDA	GGA	GGA+vdW	Exp.
C1-C2	1.484	1.506	1.476	1.508
C2-C3	1.391	1.400	1.393	1.399
C3-C4	1.391	1.400	1.389	1.401
C4-C5	1.484	1.506	1.479	1.508
C4-C12	1.400	1.410	1.400	1.409
C1-H1	1.107	1.100	1.082	1.092
C1-H2	1.110	1.101	1.081	1.096
C1-H3	1.102	1.097	1.077	1.088
C5-H7	1.103	1.097	1.086	1.093
C5-H6	1.109	1.101	1.086	1.095
C5-H5	1.108	1.100	1.092	1.092
C3-H4	1.100	1.093	1.094	1.090
	rms	rms	rms	
	0.016	0.004	0.010	

the XC functionals used, the LDA compares best to the measurements. LDA lattice constants are only 2-6% smaller than in the experiments. The good accordance of theoretical and experimental lattice parameters is lost to some extent when taking gradient corrections for XC into account. In GGA, the lattice constants are overestimated by 7-10 %. This result shows that the intermolecular interaction is not equally well accounted for within the common approximations for exchange and correlation, which is in accordance to findings of previous studies. [74, 75] Like for typical van der Waals bonded systems, the underestimation of long-range electron correlations in GGA yields incorrect lattice parameters but the effect is less pronounced than one might have expected. This indicates that even though the van der Waals interaction is very important for the occurrence of a stable durene crystal, there are likely additional effects contributing to the bonding between the molecules. Otherwise, the GGA lattice constants would compare worse to the experimental values.

The GGA+vdW approach, which has been used successfully for van der Waals bonded systems previously, [74] is not able to improve GGA lattice parameters for durene but, in fact, leads to a strong underestimation of the lattice constants a and b by more than 15%. Due to a small molecule rotation during the relaxation, the c lattice constant in GGA+vdW is not as severely underestimated as the a and b lattice constants but is very similar to the experimental one (cf. Tab. 6.1). It is observed that the shortcoming of the GGA with respect to the dispersive forces is less severe for durene than for the systems studied previously. [74, 75] As a result, the van der Waals forces overcompensate the failure of the GGA, which results in an underestimation of the lattice constants here. The reason might be that the durene crystal is not exclusively bonded by vdW forces but, as discussed elsewhere, also weak

hydrogen bonds of the C-H$\cdots\pi$ type contribute. [48, 88]

In conclusion from the findings in Tab. 6.1, the lattice parameters and, hence, the *inter*molecular interactions in durene crystals are described most reliably in LDA.

For the *intra*molecular geometry of durene in crystal phase, Tab. 6.2 compares the theoretical findings with experimental data. One finds that each of the XC functionals is able to reproduce bonding distances (cf. Tab. 6.2) and angles[3] (not shown as a table) for durene correctly. Differences across the XC functionals are small. As expected, for purely intramolecular properties, the vdW correction gives rise to only minor changes in the GGA values. From Tab. 6.2, one concludes that the best values for the intramolecular geometry are obtained within GGA but, in fact, all three approximations yield very similar results. This is additionally confirmed by the investigation of the bond angles. [48]

Based on these findings for the accuracy of the description of intermolecular and intramolecular geometry, further studies are performed using the LDA for the XC functional. In particular, the importance of the intermolecular interaction and its influence on charge transport parameters highlights the LDA as best suited.

This result shows that even though LDA has some difficulties describing strong hydrogen bonds [67, 72], it is very successful in the case of the weak C-H$\cdots\pi$-bond. No overbinding effects as for water [72] or for amino acids [68] have been found in the studies here.

In conclusion of this section, it is shown that simulations within LDA are able to give parameters for intramolecular as well as intermolecular bonds in good accordance to the experiment. Although the intramolecular properties come out slightly better in GGA, the LDA calculations give the best overall description of durene crystals due to its accurate lattice parameters. Hence, for all further calculations and, in particular, the calculations of the vibrational modes, I proceed using only the LDA for the XC functional. The geometric ground state serves as a starting point for all further computations.

6.3.3 Vibrations

Lattice vibrations are investigated by using the methods discussed in Sec. 6.1.3. A set of phonon modes with eigenvectors and mode frequencies is obtained by diagonalizing the dynamical matrix. Here, I focus on the most relevant findings. A full mode description of all Γ point phonons in the crystal as well as a description for the gas-phase molecule vibrations has been compiled in a related publication. [48] The lower energy modes in the crystal are listed in Tab. 6.3.

A symmetry classification has been carried out by an analysis of the modes by means of group theory. For the durene crystal, neglecting the three zero-frequency acoustic modes, the

---

[3]A more comprehensive characterization which also includes bonding angles is compiled elsewhere. [48]

Table 6.3: Phonon modes for the durene crystal with frequencies (in cm^{-1}) and symmetry classification. Mode descriptions hold for all subsequent empty lines. Abbreviations: torsion (tors), wagging (wagg), translation (T), and rotation (R).

Frequency	Symmetry	Mode description
224.8	A_u	butterfly
219.0, 218.2	A_g, B_g	CH$_3$ tors
214.3	B_u	butterfly
201.0, 193.6, 186.9, 186.4	B_u, A_u, A_g, A_u	CH$_3$ tors
180.2	B_u	C-CH$_3$ wagg, CH$_3$ tors
175.2	A_u	C-CH$_3$ wagg
173.7, 163.1	B_g, B_u	CH$_3$ tors
140.2, 140.2	A_g, B_g	R$_{CH}$
120.7, 113.2	A_g, B_g	R$_L$
102.4	A_u	T$_c$
84.0	B_u	T$_b$
61.7	A_g	R$_6$
53.2	A_u	T$_a$
51.5	B_g	R$_6$

141 optical modes can be represented as

$$\Gamma_{vib}^{cryst} = 36A_g + 36B_g + 35A_u + 34B_u.$$

Here, the index g (u) denotes even (odd) symmetry. In the crystalline phase, one obtains the 9 intermolecular vibrations below 150 cm^{-1}. These are classified as three translations (T) basically along the lattice vectors $\boldsymbol{a}, \boldsymbol{b}$, and $\boldsymbol{c}$ and six librations (R), i.e., molecule rotations about the axes corresponding to the principal moments of inertia (cf. Tab. 6.3). The 6 librational normal modes have even symmetry, i.e., they are not IR-active, whereas the three translational modes belong to u representations and should have more or less strong transition dipole moments. [89]

In recent experimental IR studies on the vibrational properties of durene the low-frequency region has been investigated up to 600 cm^{-1}. [86] IR spectra have also been simulated in the course of this work and are discussed elsewhere [48] since this thesis is limited in space. From these investigations one concludes that for the spectral range below 600 cm^{-1}, measurements and theoretical predictions agree very well.

For even lower frequencies in the region of the intermolecular phonons, however, the spectra recorded from suspension are not useful. For example, the translational modes can only be seen in the spectra of single crystals. [89] In the experiments of Ref. [89] the peak positions change upon cooling the crystals from room temperature down to 80 K. These low-T values can be compared to the DFT calculations. At this temperature, the T_b (T_a) translation is found at 70 (45) cm^{-1} which is in surprisingly good accordance to the findings
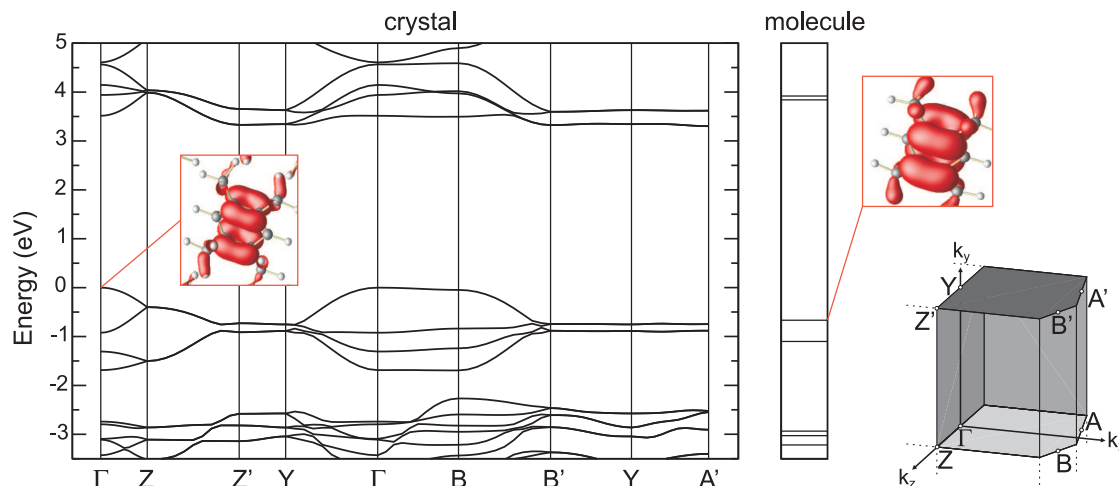
Figure 6.6: Band structure of durene along special lines in the Brillouin zone in comparison to molecular energy levels. The valence band maximum is set to zero. The definition of the high-symmetry points is depicted at the irreducible wedge of the Brillouin zone. Important high-symmetry lines: ΓB along a^*, ΓY along b, and ΓZ along c^*. The absolute square of the wavefunctions of the HOCO and the HOMO are depicted in the insets.

of 84 (53) cm^{-1}. Even for the T_c mode the value of 102 cm^{-1} accords reasonably well with the experimental wave number of 74 cm^{-1}.

The modes with g symmetry are not visible in the IR signal but in Raman measurements. The Raman spectrum of powder samples of durene [86] shows a major contribution from the spectral region below 150 cm^{-1}. Correspondingly, in the calculations one finds such modes between 110 and 140 cm^{-1} associated with librations (cf. Tab. 6.3). Furthermore, the experimental Raman frequencies [86] in the range of 250-1650 cm^{-1} are also well reproduced by the calculations.

6.3.4 Electronic Structure

In Fig. 6.6, I have plotted the band structure of durene crystals in comparison to the energy levels in durene molecules. All values are obtained as eigenvalues of the Kohn-Sham equation as discussed in Sec. 6.1.4. The most important high-symmetry lines are ΓB along the a^* direction, ΓY along the b direction, and ΓZ along the c^* direction (the latter is defined as being perpendicular to the ab plane; see Fig. 6.4). Note that the energy gap cannot directly be compared to experimental excitation energies (see discussion in Sec. 6.1.4). The insets in Fig. 6.6 also shows plots of crystal and molecular orbitals for the highest occupied crystal orbital (HOCO) and the highest occupied molecular orbital (HOMO), respectively.

The bands are formed by delocalized π orbitals of the molecule. Since the crystal unit cell contains two molecules, there are twice the number of states per unit cell in comparison to the gas-phase species. At Γ, the HOCO and the HOCO-1 are similar to the HOMO as seen from the insets in Fig. 6.6. The same analogy holds for the states below, namely, the

HOCO-2 and HOCO-3 (see Fig. 6.2) which are formed from the HOMO-1. The identification of the hole states with former molecular orbitals is justified by visual identification on the one hand and the correspondence of the energy levels on the other. From Fig. 6.6 it is obvious that the relative energetic positions of molecular orbitals experience changes below 1eV when transforming into Bloch states in the crystal, thus the energetic ordering is comparable to the energy structure in the molecule. Of course a rather strong band dispersion occurs due to the intermolecular interaction (electronic coupling). Investigating the states in the conduction band, a correspondence between molecular orbitals and crystal orbitals, established by their characteristic shapes (not shown in Fig. 6.6), has been confirmed as well.

For the valence bands, i.e. for the holes, a rather strong energy dispersion for the HOCO/HOCO-1 is found which results in a large bandwidth. The bandwidth can be quantified by the band splitting at Γ, which is mainly due to the interaction of both molecules in a crystal unit cell (cf. Fig. 6.4). The splitting amounts to 0.92 eV yielding a large transfer integral. Similarly, the HOCO-2/HOCO-3 exhibits a splitting of 0.38 eV at Γ. These values give rise to bandwidths that are unusually large for an organic molecular crystal and indicate potentially high hole mobilities in durene crystals. For the conduction bands, i.e. the electron states, similar effects are observed. The bands formed from the two lowest unoccupied molecular orbitals (LUMO and LUMO+1) overlap in energy since the dispersion is much larger than the original energy difference of 0.1 eV between LUMO and LUMO+1. The corresponding total splitting (LUCO/LUCO+3) at Γ is 1.05 eV which also indicates possibly high electron mobilities in durene crystals. From the widths of the bands one can anticipate potentially high mobilities for both electrons and holes in durene crystals. Their directional dependence, however, does not result from the bandwidth but from the band dispersion along various directions.

Interestingly, the band dispersion is extremely anisotropic. A very strong dispersion is found in b (ΓY) direction and in c^* (ΓZ) direction for the HOCO/HOCO-1 as well as for the HOCO-2/HOCO-3. But also the electron states exhibit the same characteristic anisotropy as found for the holes. A highly relevant quantitative measure for the directional dependence of mobilities are effective masses m^*. I address the observed anisotropy by studying the direction dependence of m^*. According to the definition of the inverse effective mass tensor in Eq. (5.3), the values at the valence and conduction band edges (critical points in the BZ) can be calculated for arbitrary directions. In Tab. 6.4 I have compiled the effective masses for various directions at the Γ-point for the uppermost valence band and the lowest conduction band.

The lowest mass is measured for electrons. For this type of charge carriers the effective mass is 0.49 m_e in c-direction. In the same direction one also observes the smallest hole mass

Table 6.4: Effective masses of electrons and holes at the Γ point in units of the free electron mass m_e.

direction	c	$c^*(\Gamma Z)$	$b(\Gamma Y)$	a	$a^*(\Gamma B)$
m_{el}^*	0.49	0.58	12.8	4.88	-11.9
m_{hole}^*	0.68	0.77	1.16	3.55	9.71

of 0.68 m_e. This is even smaller than along the monoclinic b axis (1.16 m_e). In contrast, both holes and electrons are very immobile perpendicular to the bc-plane. In this direction (a^*), the observed effective masses are higher by one order of magnitude or even negative. This strong anisotropy found from the analysis of the effective masses implies that durene crystals are effective two-dimensional electronic systems. This is similar to another group of herringbone-stacked organic molecular crystals, namely, the oligoacene crystals such as naphthalene as discussed in Sec. 6.2. From these findings, very anisotropic hole mobilities may be expected. [25, 44] The hole mobility should be minimal in a^* direction whereas high mobilities are expected to occur within the bc plane.

6.3.5 Charge Transport

In the preceding section, charge transport properties of durene crystals have been studied by means of bare electronic quantities which serve as precursors for transport characteristics. The electronic structure has been examined and its anisotropy has been rationalized with the concept of an effective band mass for electrons and holes. In contrast to conventional semiconductors, the relatively weak intermolecular bonds in OMCs lead to a strong interaction between the charge carriers and the lattice vibrations. Consequently, the concept of an electron/hole moving in bands and showing bandlike mobilities as in traditional inorganic crystals might no longer hold and polarons are formed. [22] I turn now to the inclusion of the electron-phonon scattering and come to the modeling of polaronic effects. The investigation of charge transport is restricted to holes since for the electrons the experimental data for comparison are incomplete.

A prominent polaronic effect is the bandwidth narrowing which reflects the increased mass of the polaron and results in a reduced band velocity (see Eq. (4.43)). In Sec. 3 this temperature-dependent effect has been quantified (see Eq. (3.44)) to

$$\widetilde{\varepsilon}_{MN} = (\varepsilon_{MN} - \Delta_{MN})\, e^{-\frac{1}{2}\sum_\lambda (1+2N_\lambda)G_\lambda}, \tag{6.6}$$

where Δ_{MN} describes polaron-binding effects and

$$G_\lambda = 2\left(g_{MM}^\lambda\right)^2 + \sum_{K \neq M}\left(g_{MK}^\lambda\right)^2 \tag{6.7}$$
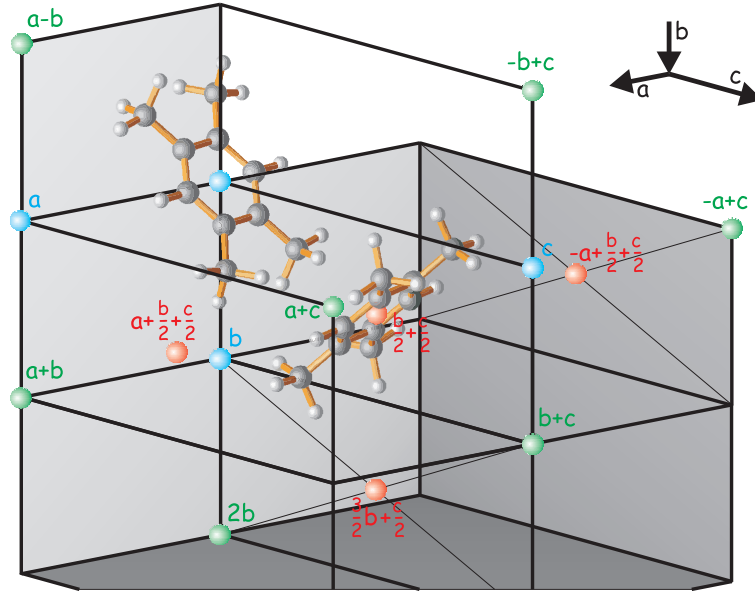
Figure 6.7: Symmetry-reduced set of most important transfer integrals.

are effective coupling constants containing all local and non-local terms (see Eq. (3.43)). The transition from the bare transfer integrals ε_{MN} to the polaron transfer integrals $\widetilde{\varepsilon}_{MN}$ amounts to a reduction of the values due to the exponential narrowing factor in (6.6) which includes the temperature T via the phonon numbers $N_\lambda = \left(e^{\hbar\omega_\lambda/k_B T} - 1\right)^{-1}$ as well as all orders of the carrier-phonon interaction via G_λ.

In order to obtain the necessary material parameters in Eqs. (6.6) and (6.7), *first princi-ples* calculations have been performed using the methods outlined in Sec. 6.1.5. In Fig. 6.7, the symmetry-reduced set of the used transfer integrals in Eq. (6.5) is plotted as colored dots at molecular sites. Besides the on-site energy and the neighbors associated with the lattice vectors in each direction, $\mathbf{R}_M - \mathbf{R}_N = 0, \pm\boldsymbol{a}, \pm\mathbf{b}, \pm\mathbf{c}$ (blue), I also consider the transfer inte-grals belonging to other lattice vectors $\mathbf{R}_M - \mathbf{R}_N = \pm(\boldsymbol{a}\pm\mathbf{b}), \pm(\boldsymbol{a}\pm\mathbf{c}), \pm(\mathbf{b}\pm\mathbf{c}), \pm 2\mathbf{b}$ (green) as well as non-lattice vectors $\mathbf{R}_M - \mathbf{R}_N = \pm(\mathbf{b}/2\pm\mathbf{c}/2), \pm(\boldsymbol{a}\pm(\mathbf{b}/2\pm\mathbf{c}/2)), \pm(3\mathbf{b}/2\pm\mathbf{c}/2)$ (red). The same mapping method is used to measure the band-structure changes due to phonon distortions to obtain the hole-phonon coupling constants (see Sec. 6.1 for details). In consistency to the theory the symmetric low-energy rotational modes are taken into consid-eration as in previous work.[4] [25, 31] They correspond to wavenumbers of 51.5, 120.7, and 140.2 cm^{-1} (see Tab. 6.3) and effective couplings $\frac{G_\lambda}{2}$ of 0.51, 0.05, and 1.16, respectively. [5]

In the first column of Tab. 6.5, a compilation of the bare hole transfer integrals which fit best to the ground-state band structure is given. The two molecules within a unit cell ($\varepsilon_{\frac{b}{2}+\frac{c}{2}} = 103.7$ meV) and the two adjacent molecules along b ($\varepsilon_b = 116.2$ meV) exhibit the

---

[4]The inclusion of other modes is not necessary as discussed for naphthalene.
[5]Note that in a related publication [58] the definition of the quantities G_λ vary by a factor of 2.

Table 6.5: Bare hole-transfer integrals ε, polaron transfer integrals $\widetilde{\varepsilon}$ according to Eq. (6.6), and resulting bandwidths (in meV).

	bare holes	polarons $(T = 0\ \text{K})$	polarons $(T = 300\ \text{K})$
$\widetilde{\varepsilon}_a$	-3.3	-0.5	-0.001
$\widetilde{\varepsilon}_b$	116.2	21.7	0.045
$\widetilde{\varepsilon}_c$	-6.7	-1.3	-0.003
$\widetilde{\varepsilon}_{a+b}$	0.7	0.0	0.000
$\widetilde{\varepsilon}_{a-b}$	0.7	0.1	0.000
$\widetilde{\varepsilon}_{a+c}$	-1.6	-0.3	-0.001
$\widetilde{\varepsilon}_{a-c}$	-0.5	-0.1	-0.000
$\widetilde{\varepsilon}_{b+c}$	-7.7	-1.5	-0.003
$\widetilde{\varepsilon}_{b-c}$	0.5	0.0	0.000
$\widetilde{\varepsilon}_{2b}$	-21.6	-4.9	-0.010
$\widetilde{\varepsilon}_{\frac{b}{2}+\frac{c}{2}}$	103.7	18.6	0.038
$\widetilde{\varepsilon}_{a+\frac{b}{2}+\frac{c}{2}}$	5.3	0.9	0.002
$\widetilde{\varepsilon}_{-a+\frac{b}{2}+\frac{c}{2}}$	2.0	0.3	0.001
$\widetilde{\varepsilon}_{\frac{3b}{2}+\frac{c}{2}}$	2.9	0.5	0.001
bandwidth	952	171	0.35

strongest electronic interaction. As a result of the hole-phonon coupling, one observes a strong reduction of these values at room temperature, and even at $T = 0$ K there is already a significant decrease due to zero-point vibrations. From these polaron transfer integrals one can directly calculate the T-dependent polaron bandwidth which reduces from the bare value of 952 meV to 171 meV at $T = 0$ K and to 0.35 meV at $T = 300$ K.

Following Holstein's original idea, the size of the polaron and the transport mechanism can be estimated from the energy ratio $\frac{E_p}{B}$ (see Sec. 2.3.1). Here I use $\frac{E_p}{B_p}$, where B_p is the polaron bandwidth, in order to account for the temperature dependence of the bandwidth as discussed above. To estimate the transport mechanism from the findings about the polaron bandwidths one has to compare the bandwidths, which reflects the energy gain due to delocalization, to the polaron binding energy $E_p = \sum_\lambda g_\lambda^2 \hbar\omega_\lambda = 24$ meV reflecting the localization aspect. Comparing E_p to B_p for different T, where B_p varies between 171 meV and 0.35 meV, evidently, the carriers are very unlikely delocalized at room temperature but can be regarded rather delocalized at 0 K. Accordingly, band transport will not be a suitable concept for the description of carrier motion at room temperature but for small T it should give good results. At this point, however, no statement is possible about the transport mechanism in the intermediate temperature regime.

In order to model the charge transport in durene crystals, the above-described polaron-band picture is helpful but, in itself, not sufficient. Due to the large carrier-phonon coupling and, hence, strong localization, the bandlike transport may be suppressed and, instead, ther-
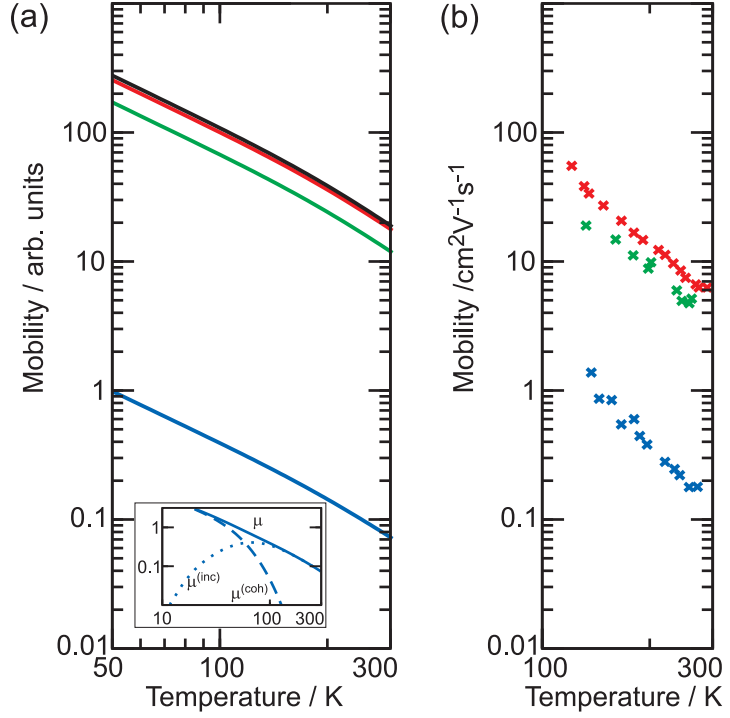
(a)

(b)

Figure 6.8: (a) Solid lines: Calculated durene hole mobilities μ according to Eq. (6.8). Values for b (red), c (black), 35° off bc plane (green), and $a^* \equiv \perp bc$ (blue). Inset: Dashed line: Band mobility $\mu^{(coh)}$, as calculated by setting $\Phi_\lambda(t) \equiv 0$ in Eq. (6.8). Dotted line: Hopping mobility $\mu^{(inc)} = \mu - \mu^{(coh)}$. (b) Measured durene hole mobilities from Ref. [39]. Data points for 45° between b and c (red), 35° off bc plane (green), and a^* (blue).

mally activated hopping may become important. In general, for ordered crystals which exhibit a large bandwidth on the one hand but also strong polaronic effects on the other, an *a priori* assumption whether bandlike transport or hopping is prevailing cannot be made, as discussed in Sec. 1. In fact, it has been stated previously in the thesis that the sharp transition from band transport to hopping can only be described within a transport theory treating both on equal footing. I make use of the recently developed expression for the mobility tensor based upon a non-perturbative evaluation of the Kubo formula [31, 44], which has been introduced in the discussion of Eq. (4.55). The expression reads[6]:

$$\mu_{\alpha\beta} = \frac{e_0}{2k_B T \hbar^2} \sum_{M,N} (R_{M\alpha} - R_{N\alpha})(R_{M\beta} - R_{N\beta})$$
$$\times \int_{-\infty}^{\infty} dt F_{MN} e^{-\sum_\lambda G_\lambda(1+2N_\lambda)} e^{+\sum_\lambda G_\lambda \Phi_\lambda(t)} e^{-\frac{t^2}{\tau^2}} , \qquad (6.8)$$
$$F_{MN} = (\epsilon_{MN} - \Delta_{MN})^2 + \frac{1}{2} \sum_\lambda \left(\hbar\omega_\lambda g_{MN}^\lambda\right)^2 \Phi_\lambda(t).$$

As an important feature, one recognizes that the (coherent) narrowing term $e^{-\frac{1}{2}\sum_\lambda(1+2N_\lambda)G_\lambda}$ from Eq. (6.6) reappears in the mobility but is now supplemented by an additional exponent containing $\Phi_\lambda(t) = N_\lambda e^{i\omega_\lambda t} + (1+N_\lambda)e^{-i\omega_\lambda t}$. This exponent explicitly describes (incoherent) scattering events with absorption and emission of phonons, and its opposite sign indicates a

---

[6]The mobility expression used for this part of the thesis is different to the one derived in Chap. 4 (Eq. (4.37)) since the study had been carried out before the theory in Chap. 4 has been developed. The subsequent discussion of the mobility anisotropy, however, is not affected by the choice of the mobility expression, at least not as far as temperatures above 100 K are concerned for which experimental measurements are published.
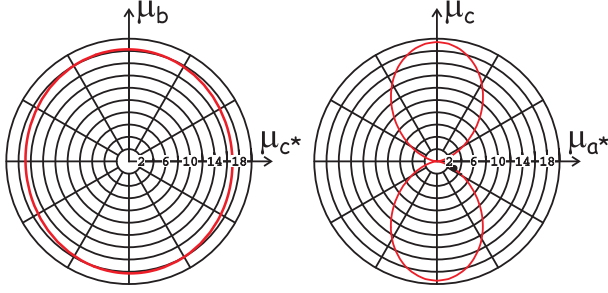
Figure 6.9: Hole mobilities in durene within the herringbone-stacking (*bc*) plane and the perpendicular ca^* plane.
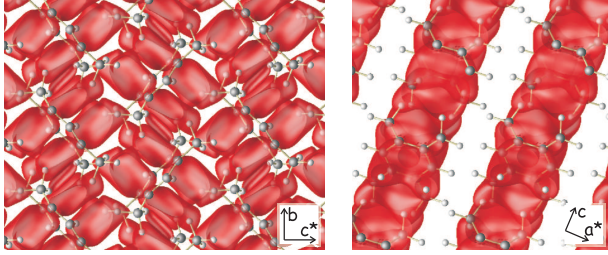

Figure 6.10: HOMO-overlap density in durene as described in the text as a visualization tool for the relevant carrier channels in herringbone-stacked materials. View onto the herringbone (*bc*) plane (left) and onto the ca^* plane (right).

thermally activated, i.e., hopping contribution to the mobility.

In the following, the results for the anisotropy and temperature dependence of the hole mobilities in durene crystals are presented. The theoretical analysis is based upon Eq. (6.8) in conjunction with an *ab initio* determination of all relevant material parameters according to the methods described in Sec. 6.1.

The durene hole mobilities are plotted in Fig. 6.8 (a). First, I discuss the T dependence. As an important result, it is found that in spite of small transfer integrals at $T = 300$ K, the mobility curves still exhibit a behavior that is commonly associated with bandlike transport: decreasing mobilities with increasing T. The same behavior is found in the experiments in Fig. 6.8 (b). Moreover, this decrease is almost independent of the direction, in accordance to the experimental data. The simultaneous presence of a very narrow band and a seemingly bandlike mobility behavior is at first somewhat surprising and puzzling. It can only be understood by the complex interplay between the band narrowing and hopping terms in Eq. (6.8), which is illustrated in the inset of Fig. 6.8 (a). While at low T the total mobility is basically governed by the band narrowing term (dashed line), the hopping term (dotted line) becomes increasingly important at higher T. Nonetheless, the underlying thermally activated behavior at high T, where it dominates the total mobility, becomes masked due to the overall $1/T$ prefactor in Eq. (6.8), see also Ref. [44].

As another important result, one finds that the direction dependence of the absolute mobility values is highly anisotropic. This is analyzed in polar plots in Fig. 6.9. It gets obvious that within the herringbone (*bc*) plane the changes upon angular variation are small but along the perpendicular direction (a^*) the mobilities drop by two orders of magnitude, see also Fig. 6.8 (a). This anisotropy is confirmed by experimental findings from time-of-flight

measurements [39]; only the difference between in-plane and out-of-plane values is somewhat smaller in the experiments, see Fig. 6.8 (b).

An important observation is that the anisotropy in the mobility stems from an anisotropy in the underlying electronic structure. For example, the small a^* mobility can be traced back to the transfer integrals in this direction: only the small values for ε_a, $\varepsilon_{a+\frac{b}{2}+\frac{c}{2}}$, and $\varepsilon_{-a+\frac{b}{2}+\frac{c}{2}}$ give minor contributions compared to the much larger values ε_b and $\varepsilon_{\frac{b}{2}+\frac{c}{2}}$ for the bc plane. This is also true including hole-phonon interaction.

In view of these findings, I conclude that the anisotropy in the electronic coupling between molecules is a valuable precursor for the resulting mobility anisotropy in the crystal. Moreover, this electronic coupling between the molecular orbitals can be directly estimated from the overlap of the wavefunctions (see definition of the transfer integrals in Eq. (3.2)). The orbital plots in the insets of Fig. 6.6 give no indication for a preferred overlap direction. However, from molecular orbital theory, it can be expected that these orbitals are mainly extended perpendicular to the molecular plane, i.e., the plane of the π-electron system. The normal vector to this plane lies nearly completely in the bc-plane (herringbone plane) with a deviation of less than $2°$. Hence, a strong wavefunction overlap may be expected within herringbone planes. This amounts to a strong wavefunction overlap between the two molecules in the unit cell, i.e., within the bc plane (see Fig. 6.4) and of adjacent molecules belonging to different unit cells in b direction, which is the reason for the respective transfer integrals $\varepsilon_{\frac{b}{2}+\frac{c}{2}}$ and ε_b being much larger than between molecules lying in different herringbone planes.

In order to illustrate the implications of such a pairwise overlap of wavefunctions for the crystal as a whole, I have computed the sum $\sum'_{ij} |\psi_i(\mathbf{r})\psi_j(\mathbf{r})|$ over all pairs of overlapping HOMO wavefunctions of durene molecules in crystal geometry, where the sum excludes $i = j$. This results in an overlap density and gives an excellent impression of the formation of global transport channels.[7] Figure 6.10 shows the overlap density in an isosurface plot. The sum of all pairwise contributions gives rise to a dense herringbone pattern leading to the formation of wide hole-transport channels traversing the entire herringbone-stacking plane. The bc-planes are nearly isotropically filled which corresponds nicely to the findings for the bc-mobilities in Fig. 6.9. In contrast thereto, the top view (ca^*-plane) exhibits that the overlap density nearly vanishes between the individual herringbone planes. Due to such large gaps between the two-dimensional channels it is clear that the carriers are confined to the herringbone planes. In order to move through the crystal in the perpendicular a^* direction, the holes have to overcome these gaps which strongly reduces the mobility, in agreement with the simulations for this direction. These findings are particularly relevant because they allow for

---

[7]If $i = j$ was included the resulting quantity resembles the charge density for which a correlation between density and anisotropy of electronic coupling was found as well [90]. The overlap density used here, however, is an even better indicator.

an understanding why the transport channels in herringbone-based OFET devices are often confined to the surface layers. [8]

In summary, based on *first principles* DFT calculations with several approximations for XC, the ground state geometry has been investigated. Proceeding with the best performing LDA functional, vibrational and electronic properties have been analyzed. Large bandwidths were found for valence and conduction bands along with a strong anisotropy in the crystal band structure, which was further rationalized by the calculation of band effective masses. Besides the anisotropy, the influence of the temperature on the effective electronic structure has been studied making use of the polaron concept. It was found that the polaron bandwidth is strongly reduced at $T = 300$ K which rather points to a hopping mechanism for transport at room temperature.

This was further examined in a study on the hole mobility in durene crystals. The mobility was investigated within a sophisticated theory which takes polaronic effects, hopping, and band transport into account. I have analyzed the temperature dependence and anisotropy of hole mobilities in durene. The temperature dependence was found to be equal for all directions, with a dominating mobility contribution from band transport for low T and hopping for room temperature. As an example for herringbone-stacked materials, durene essentially shows a two-dimensional mobility characteristic. This feature was traced back to the wave-function overlap which leads to large transfer integrals. As an important observation, the directional distribution of the largest transfer integral governs the mobility anisotropy. An analysis of the overlap density is proven a powerful tool to understand and visualize the resulting carrier-transport channels in such crystals. In addition to the two-dimensional plots, these transport channels are even more impressive in 3D views as created in a movie[8] for a related publication. [58]

6.4 Guanine

6.4.1 Introduction

The study of crystalline guanine (see Fig. 6.11 for a structural overview) is motivated by several aspects. As one of the DNA bases, guanine has an outstanding role over the usual "suspects" in organic electronics. This is related to the self-assembly of DNA, which may be of importance in building up organic electronic devices in a bottom-up approach. Its π conjugation should give rise to wide HOMO/LUMO bands similarly to the oligoacenes and durene but the anisotropy is unknown. Due to the occurring strong hydrogen bonds,

---

[8]The movie showing the hole overlap density in durene crystals can be downloaded from http://ftp.aip.org/epaps/appl_phys_lett/E-APPLAB-93-052847/254195_0_vid_0_k71b6k.mpeg.
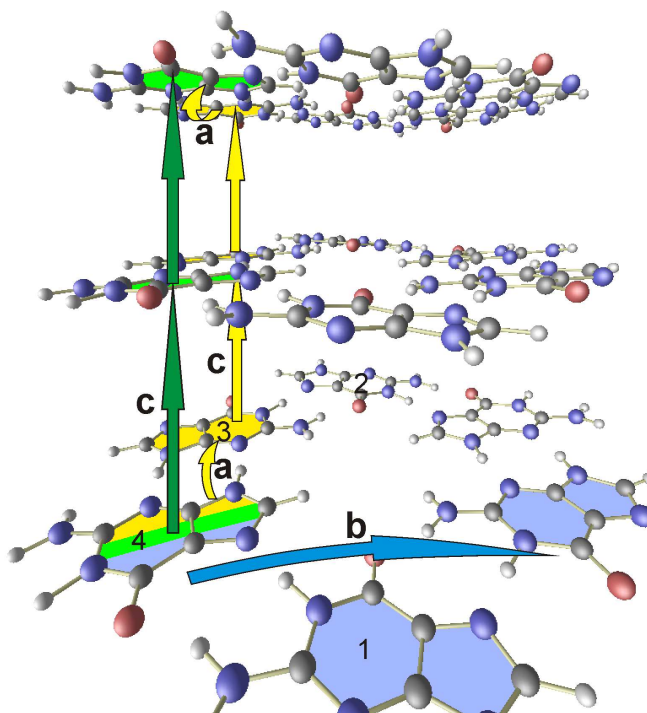
Figure 6.11: Perspective view to the layers in a guanine crystal (three molecular planes are shown). For clarity, the plane distances in the vertical stacking direction have been doubled and water molecules have been omitted. The four molecules in a single unit cell are labeled from 1 to 4 each of which represents also a vertical stack. Transport pathways are indicated by arrows (c: along the stack, a and b: between the stacks).

which are not present in acene-type crystals like naphthalene or durene, guanine crystallizes in a structure different to the herring-bone fashion, which may give a different anisotropy characteristic as well.

In addition, the DNA molecule itself (e.g. in form of a poly-guanine–poly-cytosine sequence) is considered to be interesting to study. [91] In solution, the DNA bases are stacked along the helix axis and the π-π interaction along this direction led to the notion of a (semi-) conducting molecular channel very soon after the discovery of the real structure. [92] Also, an enormous knowledge of synthesizing and manipulating the DNA has been gathered over the past decades. Therefore, nanowires based on the DNA are considered promising candidates for molecular devices toward the further miniaturization of electronic technology and have been studied actively in the past. [93–100]

A different type of transport study, namely, through a guanosine derivative in a field effect transistor geometry has been carried out recently. [101] In contrast to DNA, where the charge transport occurs along the stack through intrastrand or interstrand pathways (c or a direction, respectively, in Fig. 6.11), Ref. [101] investigated the charge transport along a ribbon structure of guanines across the hydrogen bridges within single molecular planes (b direction in Fig. 6.11). The transport in this direction does not fit into the simple overlap-of-π-orbitals picture. In order to better understand the anisotropy arising from the relative orientation of the guanine molecules, it is instructive to consider three-dimensional guanine crystals as a model system. The guanine crystals studied here have the great advantage to provide many transport pathways simultaneously due to the anisotropy of the molecular
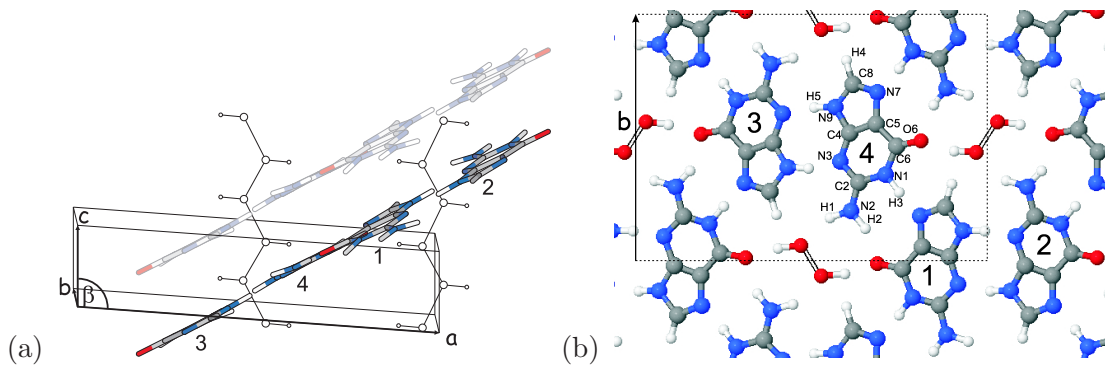
Figure 6.12: (a) Monoclinic unit cell of the guanine monohydrate crystal with atomic basis of four guanine molecules. Neighboring parallel layer and water columns along the c-axis are indicated. (b) View along the c direction of the crystal. The dashed box indicates the unit cell with the lattice vector **b**. Black double lines represent hydrogen atoms in a hydrogen bridge bond of the OH···O type in the water columns.

arrangement, among them, a stack similar to the base pair stack in DNA and a ribbon geometry as used in the transistor experiment of Ref. [101].

Previously, much computational effort has been spent to determine the structural properties of the gas-phase guanine molecule as well as its vibronic and electronic excitations. However, much less work has been devoted to condensed aggregates. [102–105]

The structural results and vibrational properties of guanine crystals are presented in Sec. 6.4.2 and Sec. 6.4.3, respectively. Electronic properties follow in Sec. 6.4.4, and Sec. 6.4.5 is devoted to the charge transport. The findings are discussed in relation to transport pathways in DNA-based structures like guanine quadruplexes and ribbons which are considered to play a major role in DNA-based nanoelectronics. The mobility results are interpreted by help of a novel visualization method for transport channels, which is derived from overlapping wavefunctions. An analysis of coherent and incoherent contributions to the mobility shows which mechanism dominates at room temperature in guanine structures with high purity and long-range order like crystals.

6.4.2 Geometry

The crystal structure of guanine is obtained from experimental results from X-ray diffraction [106]. Guanine crystallizes in a monoclinic crystal with axes **a**, **b**, and **c** and the monoclinic angle β between **a** and **c** as depicted in Fig. 6.12 (a). The molecules arrange in a more or less planar configuration in ($\bar{3}$01) planes. Water molecules are arranged in columnar structures interconnecting these planes as indicated in the figure.

Laterally, the arrangement is stabilized by a hydrogen bonding network between the guanine molecules as well as between the water columns and the guanine molecules. This bonding is different from what has been proposed for a guanine monolayer on graphite [107]
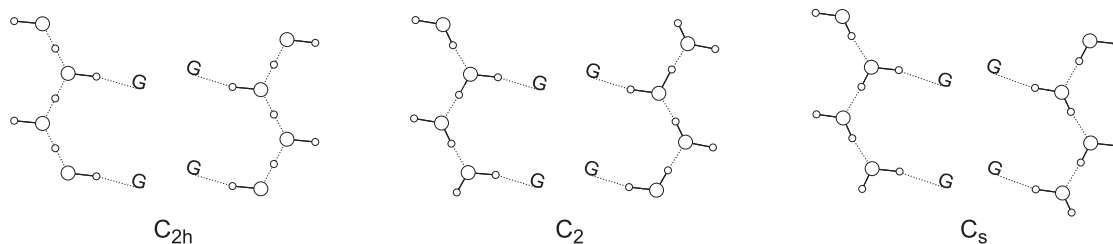
Figure 6.13: Schematic drawing of the columnar H_2O structures in the high-symmetry geometry (left) and low-symmetry configurations (middle and right).

or the Hoogsteen-bonded guanine tetraplexes. [108] From Fig. 6.12 (b) it can be seen that each water molecule forms an OH$\cdots$O hydrogen bond to an oxygen atom of one guanine molecule as well as an NH$\cdots$O hydrogen bond with an amino group of another guanine molecule. In the experimental studies [106], the positions of the water hydrogens could only be determined with large error bars, but also the positions of the water oxygens along the H_2O columns are affected by considerable uncertainty. Nevertheless, the dominating structure is clearly identified as a stacking of guanine molecules hydrogen-bonded to the water columns with space-group symmetry P2$_1$/c (C$_{2h}^5$) and associated point group C$_{2h}$. In the original paper, Thewalt et $al.$ (cf. Ref. [106]) discussed that the water columns may have a more complicated structure. This is motivated since the space group symmetry P2$_1$/c suggests symmetric hydrogen bonds, i.e., that the water hydrogens, which are not hydrogen-bonded to the guanines, are in a symmetric position between the water oxygens, which appears as an unlikely geometry. A more realistic asymmetric assignment of these hydrogens lowers the symmetry to either P2$_1$ (C$_2^2$) or Pc (C$_S^2$) with associated point groups C$_2$ and C$_S$, respectively. For better visualization, these three possible structures of the H_2O columns are sketched in Fig. 6.13 in a view along the monoclinic b axis. The assignment of the hydrogens to the upper oxygens in both columns gives the C$_S$ structure whereas the assignment to upper oxygens in one column and to lower oxygens in the other column results in a crystal with C$_2$ symmetry. For that reason, the three different crystal structures are investigated and compared with respect to energetic results, ground-state geometries, and vibrational and electronic properties. Henceforth, they will be named according to their point group symmetry: the C$_{2h}$, C$_2$, and C$_S$ structure.

The lattice parameters as derived from the total energy minimization are listed in Tab. 6.6 for the three different local arrangements of the H_2O columns. The LDA results are compared with the results derived within the GGA scheme and measured data from Ref. [106]. For the LDA lattice constants one obtains equilibrium values that are below those found experimentally. For a, b, and c this underestimation amounts to 5.4%, 3.3%, and 2.9%, respectively. These deviations seem to be in agreement with the general overbinding tendency

Table 6.6: Lattice constants a, b, and c (Å) and monoclinic angle β (deg) for the guanine monohydrate crystal in different structures and for different XC approximations. Experimental reference data from Ref. [106].

	LDA			GGA	Expt.
	C_{2h}	C_S	C_2	C_{2h}	
a	15.62	15.68	15.68	16.35	16.510(8)
b	10.91	10.93	10.93	11.25	11.277(8)
c	3.54	3.53	3.53	4.024	3.645(5)
β	94.2	94.4	94.4	98.9	96.8(1)

for covalent bonds using a local approach to XC and are very similar to the results for durene (cf. Sec. 6.3.2). The deviation of the monoclinic angle β from its measured value is 2.5° in average and somewhat larger than in durene. Within the DFT-GGA description, the two largest lattice constants, a and b, are increased and approach the measured values. This can be explained with the correction of the overbinding of the hydrogen bonding network of the guanines in agreement with general observations for hydrogen bridge bonds (cf. Refs. [67, 72, 109]). In order to explain the strong elongation of the c lattice constant within GGA, one has to consider the bonding mechanism perpendicular to the guanine sheets. Bonding in c direction is only partially governed by the hydrogen bonds of the water columns. Instead, the vdW interaction is expected to play a substantial role in the bonding along the c direction. As a result, within GGA one observes a significant expansion of the lattice perpendicular to the guanine sheets. The indirect guanine-water-guanine bridge obviously cannot prevent the expansion of the lattice in c direction that is caused by the failure of GGA describing the vdW interaction. The GGA calculations give intermolecular plane spacings of 3.64 Å. Compared to the experimental value of 3.30 Å, [106] this overestimation (10%) is larger than the underestimation in LDA (3.15 Å or -4.5%).

Finally, I compare the different structural models for the water columns. As seen from Tab. 6.6, one observes only very small changes in the lattice parameters going from the high-symmetry H_2O columns (C_{2h}) to columns of lower symmetry (C_S and C_2). Therefore, one concludes that the influence of the detailed arrangement of the hydrogen atoms in the columns on the lattice and, hence, on the intermolecular spacing of the guanine molecules is negligibly small. Between the two low-symmetry structures there is practically no difference at all.

In a related publication, the intramolecular guanine bond length and bond angles are compared as well in detail. [49] One finds that the three structures under investigation do not differ in the guanine geometries. Also, the comparison to the experimental findings yield only small deviations of 1.4° for bond angles between heavy atoms and bond length of 0.018

Å, which is very similar to the given error bars in the experiment. As a result, the structural influence of the water columns on the guanine molecules in the three different crystals is nearly identical.

Another important quantity is the total energy for the three structures. Here, one finds that, from the energetic point of view, the most symmetric crystal (C_{2h}) is the least stable one. A lower energy is obtained in both low-symmetry structures. It costs approximately 0.15 eV per unit cell or 0.84 kcal per mole water molecules to move the hydrogens into the mid-oxygen position in the C_{2h} structure. Since this holds for both low-symmetry structures, the potential for these hydrogens in-between the oxygens can be characterized as a double-well barrier.

6.4.3   Dynamic Properties

Having discussed the structural properties, I come to the investigation of the lattice vibrations. Thereby, I concentrate on the discussion of the low-frequency vibrations as displayed in Tab. 6.7, mainly for two reasons: First, they basically describe *inter*molecular vibrations and are therefore more sensitive to the actual bonding between the molecules. Second, because of their low frequencies, these modes can be occupied at room temperature and, hence, influence thermal properties and charge-transport characteristics of the crystal. The intermolecular vibrations can also indicate possible changes in the crystal bonding that can be detected immediately from changes in the mode frequency or the motion pattern of these modes.

For the three crystal structures of a guanine monohydrate crystal as discussed throughout this section, the presentation of the lowest energy vibrations in Tab. 6.7 includes the description of the modes, their frequencies, and a classification with respect to symmetry operations. A comprehensive list for all modes can be found in Ref. [49]. The low-frequency part, in general, is dominated by *inter*molecular modes where the molecules move as a whole. The large effective masses related to these translations and/or rotations of the molecules give rise to small frequencies. For similar reasons the lowest *intra*molecular vibration in the crystal, more precisely the bending motion of the guanine molecule as a whole (the so called butterfly mode), appears in this region as well. For the mode description of intermolecular modes the term T (R) for translation (rotation) of the guanine molecules is used if not indicated differently as, e.g., "H_2O: T", which denotes a translation of the water molecules or "H_2Ocol: T", which indicates that the water columns translate as a whole. The indices a, b, and c refer to the displacement direction more or less parallel to the crystal axes. For rotations, the index L (S) denotes the long (short) axis of the guanine molecule as the rotation axis within the guanine plane while c denotes the normal axis to the plane. Finally, due to

Table 6.7: Lowest phonon modes for the guanine monohydrate crystal with frequencies (in cm^{-1}), symmetry classification, and mode descriptions. For abbreviations see text or original paper [49].

| mode description	C_2 frequency	symm.	C_S frequency	symm.	C_{2h} frequency	symm.
T_b	187.2	B	187.0	A"	187.7	B_g
T_a	184.6	A	184.6	A'	186.5	A_g
R_c, T_a	179.6	A	179.7	A"	180.3	A_u
butterfly	176.2	A	176.2	A'	176.4	A_g
butterfly	170.5	B	170.3	A'	169.1	B_u
butterfly	168.1	B	168.8	A"	168.7	B_g
butterfly	161.2	A	160.9	A"	160.5	A_u
T_b	170.0	B	168.5	A'	168.2	B_u
R_c	156.5	A	156.5	A'	156.7	A_g
R_c	152.2	B	152.1	A'	152.2	B_u
R_L, T_a	148.4	B	149.1	A"	148.6	B_g
R_c; H_2Ocol: T_b	142.9	A	142.6	A"	143.8	A_u
R_c	137.6	B	137.5	A"	138.0	B_g
R_L, T_a	125.0	B	125.1	A"	124.6	B_g
R_L	122.1	A	122.1	A'	122.4	A_g
H_2Ocol: $T_{b/a}$; T_b	120.4	A	119.4	A"	116.3	A_u
H_2Ocol: $T_{b/a}$	115.9	B	115.4	A'	115.2	B_u
R_L; H_2Ocol: $T_{a/b/c}$	107.2	A	107.3	A"	106.8	A_u
R_L	103.6	B	103.8	A'	103.4	B_u
R_S; H_2Ocol: T_c	99.2	B	98.6	A'	94.7	B_u
T_c	84.9	A	84.9	A'	85.6	A_g
R_S	85.1	B	85.0	A"	85.1	B_g
H_2Ocol: T_c; R_S	74.6	B	75.0	A'		
H_2Ocol: T_c					73.3	B_u
T_b; H_2Ocol: T_c	73.0	A	69.6	A'		
T_b					71.0	A_g
H_2Ocol: T_c; T_c, R_s			69.9	A"		
H_2Ocol: T_c; R_s, T_c	68.8	A				
H_2Ocol: T_c; T_c					67.2	A_u
T_c	57.7	B	57.8	A"	58.0	B_g
R_S; H_2Ocol: T_c	57.7	A	56.2	A"	57.0	A_u
T_c, R_S	49.7	A	48.7	A"	48.2	A_u
R_S	46.0	A	45.3	A'	43.9	A_g
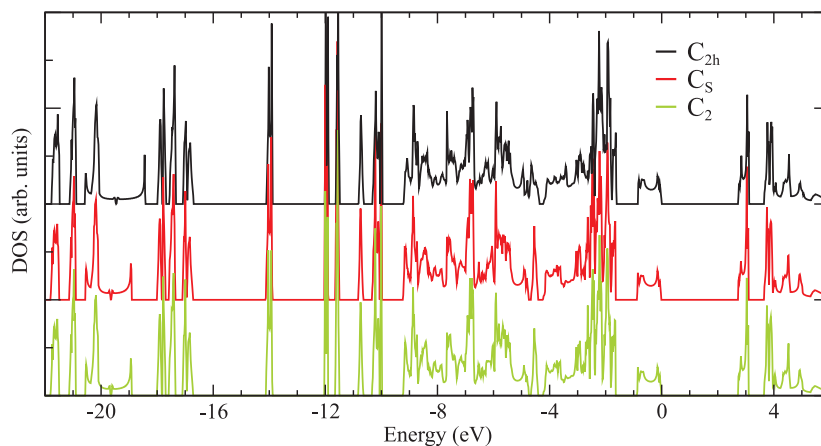
Figure 6.14: Electronic density of states. The valence band maximum is set to zero.

the symmetry classification of the modes of the C_{2h} structure one can identify IR-active and Raman-active modes as *ungerade* (u) and *gerade* (g) modes, respectively.

The results in Tab. 6.7 show that for the majority of the modes one can observe very similar mode patterns in all three crystals. These modes are put together under the same mode description. Hence, it follows that the influence of the water column arrangement on low-frequency modes related to guanine molecules is also small and that it is essentially restricted to modes with contributions from the water. Further evidence is found in the respective frequencies where deviations among the structures rarely exceed a few cm^{-1}.

In conclusion, similarly to the structural properties discussed in Sec. 6.4.2, also the vibrational properties of guanine crystals are only minimally influenced by the exact arrangement of the water columns. Even the energetically unfavorable C_{2h} structure gives nearly the same results as the more stable C_S and C_2 crystals, especially in the low-energy region relevant for thermal and/or charge transport.

6.4.4   Electronic Properties

The electronic DOS is plotted in Fig. 6.14 for the three geometries of the H_2O columns. Apparently, the graphs are again very similar among the structures. Once more, this indicates the localized nature and small magnitude of effects caused by structural modifications of the water columns. A closer inspection of the graphs reveals that the low-symmetry structures and the C_{2h} crystal differ in their electronic DOS primarily in the lower energy region around -20 eV. These modifications are attributed to states centered at the water columns and are discussed elsewhere. [49]

However, due to their energetic position, these states do not influence the HOCO and the LUCO which are the most important crystal orbitals for charge transport. The decomposition of the DOS with respect to the molecules (not shown as a plot) further confirms that HOCO
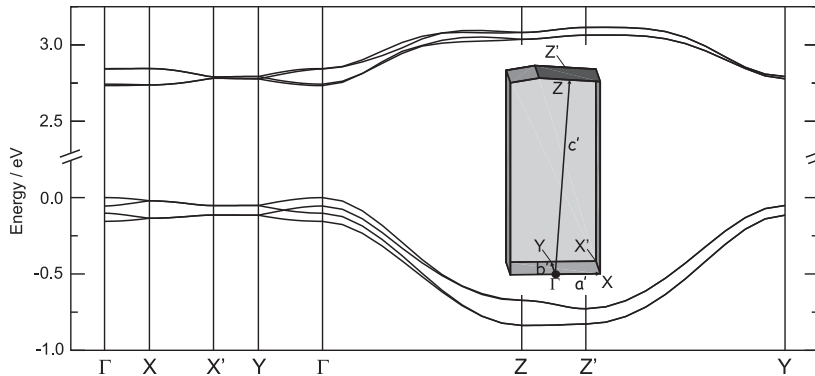
Figure 6.15: Bandstructure of the guanine crystal in the C_{2h} structure. The valence band maximum is set to zero. Inset: Irreducible part of the Brillouin zone with half reciprocal lattice vectors $\boldsymbol{a}$', $\boldsymbol{b}$', and $\boldsymbol{c}$'.

and LUCO are only derived from guanine orbitals. As an important consequence, it follows that for the three structures discussed throughout this section, the electronic DOS in the vicinity of the fundamental gap is nearly identical, as can be seen from Fig. 6.14.

In order to investigate the electronic properties further, I calculate the crystal band structure. A plot of the gap region is displayed in Fig. 6.15 for the C_{2h} crystal. The definition of critical points in the Brillouin zone is given in the inset of Fig. 6.15. At first, in agreement with the findings for the DOS, the variation among the three configurations in the regions of the highest valence bands and lowest conduction bands is only on the order of 10 meV, hence they would be hardly distinguishable in Fig. 6.15. Consequently, the figure shows only the band structure of the C_{2h} crystal. Moreover, this accordance holds for the entire HOMO band as well as for the LUMO band each of which consists of four bands lying energetically close to each other. From these findings it follows that the respective states in the C_2 structure and the C_S structure nearly coincide with their counterparts in the C_{2h} crystal.

Having discussed the negligible influence of the water molecules, I now turn to the electronic coupling between the guanine molecules themselves which causes the band dispersion. There are two types of such interactions. First there is an interaction *within* each guanine layer which is due to wavefunction overlap between the four guanine molecules in the unit cell. A good measure for this type of interaction is the Davydov splitting of the HOMO and LUMO bands at Γ. The energy difference at Γ between HOCO and HOCO-3 is found to be 0.16 eV, and the splitting between the LUCO and LUCO+3 amounts to 0.11 eV. Even though these splittings are not small, compared to the overall dispersion of the HOMO bands and the LUMO bands, they are of minor importance. The strong band dispersions are a consequence of the other type of interaction, namely the interaction *between* the guanine layers. In fact the largest dispersion of the guanine states is observed in the ΓZ direction, i.e. approximately the direction of the H_2O columns. The reason for this is the strong coupling of the molecular

states in that direction caused by the shape and the extent of the π orbitals. In that respect the crystals are similar to the DNA itself. There, the interaction of the π orbitals along the helix axis has already been suggested to be a prerequisite for a one-dimensional conducting channel by Eley and Spivey. [92] Moreover, doublets and triplets of guanines act as an effective hole trap due to their higher oxidation potential compared to single guanines, [110] which results from the coupling of the molecular states. In the a'b' plane the energy dispersion is approximately one order of magnitude smaller. A similar strong anisotropy was found for durene. However, for guanine strong band dispersion is found only in a single direction.

In guanine crystals the electronic coupling results in a bandwidth of 0.83 eV for the HOMO bands and of 0.38 eV for the LUMO bands. This is larger than the bandwidths found in comparable calculations for oligoacene crystals [25] and comparable to the bandwidth in durene crystals (cf. Sec. 6.3.4). It indicates that guanine crystals should indeed be considered as organic crystals with potential electronic applications, at least with hole transport in the stacking direction.

6.4.5   Charge Transport

From the band structure one obtains the transfer integrals according to a fit procedure similar to the one described for durene in Sec. 6.1.5. Here, I focus on hole transport in guanine crystals. The results are collected in Tab. 6.8. In order to describe temperature-induced effects in the electronic structure, I additionally take into account the vibrational degrees of freedom and the coupling between the charges and the vibrations according to the Holstein-Peierls Hamiltonian (2.3). For the guanine crystal one obtains effective coupling values[9] of $\frac{G_\lambda}{2} = 0.25, 0.09, 0.34$ for the three symmetrical rotations at $\hbar\omega_\lambda = 10.6, 15.2, 17.1$ meV (85.1, 122.4, and 138.0 cm^{-1}, respectively; see Tab. 6.7) according to the method described in Sec. 6.1.5 in more detail.[10] With these material parameters one can directly evaluate the mobility expression Eq. (6.8).[11] The result (assuming again a broadening of $\hbar/\tau = 0.1$ meV) is plotted in Fig. 6.16 which gives an overview over the temperature dependence of the mobility for different directions.

With increasing T the mobilities are strongly reduced underlining the effect of electron-phonon interaction and polaron formation. Decreasing mobilities with rising T as seen in Fig. 6.16 are known from band transport. In contrast, here one finds that at room temperature actually only a small fraction of the mobility is really due to coherent transport even for this

---

[9]Note that in a related publication [111] the definition of the quantities G_λ vary by a factor of 2.

[10]The inclusion of other modes is not necessary as discussed for naphthalene.

[11]The mobility expression used for this part of the thesis is different to the one derived in Chap. 4 (Eq. (4.37)) since the study had been carried out before the theory in Chap. 4 has been developed. The subsequent discussion of the mobility anisotropy, however, is not affected by the choice of the mobility expression, at least not for higher temperatures.

Table 6.8: Transfer integrals that best fit to the hole band structure. Values are given in meV. For denotation see 6.11.

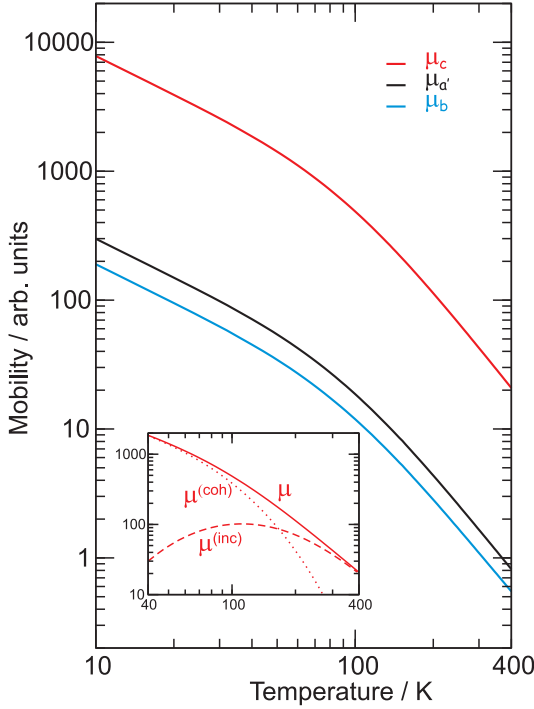|					
$\varepsilon_{11}^{\mathbf{a}}$	0.0	ε_{12}^{0}	-10.2	ε_{14}^{0}	1.2
$\varepsilon_{11}^{\mathbf{b}}$	4.1	$\varepsilon_{12}^{\mathbf{c}}$	48.2	$\varepsilon_{14}^{\mathbf{a}}$	8.0
$\varepsilon_{11}^{\mathbf{c}}$	170.4	$\varepsilon_{12}^{-\mathbf{c}}$	5.5	$\varepsilon_{14}^{\mathbf{c}}$	12.0
$\varepsilon_{11}^{\mathbf{2c}}$	11.7			$\varepsilon_{14}^{\mathbf{ac}}$	-5.7
$\varepsilon_{11}^{\mathbf{bc}}$	-1.2				

Figure 6.16: Temperature dependence of hole mobilities in guanine crystals. The mobility along the stack is given by μ_c, whereas $\mu_{a'}$ and μ_b measure the mobilities in perpendicular directions. Inset: Coherent ($\mu^{(coh)}$) and incoherent ($\mu^{(inc)}$) contributions to the total mobility μ.

model system of high purity. The inset in Fig. 6.16 shows the composition of the total mobility (in stacking direction) with respect to incoherent and coherent contributions. The coherent mobility is obtained by setting $\Phi_\lambda = 0$ in (6.8). In the low-T limit, coherent processes contribute most since the number of scatterers (N_λ) is small. The incoherent processes obtained by $\mu^{(inc)} = \mu - \mu^{(coh)}$ are negligible in this limit but become more important with rising T. The break even point depends on the static disorder of the sample and shifts to lower temperatures if the purity/crystallinity is reduced, i.e., the lower the crystallinity the lesser is the contribution from band transport. The total mobility in Fig. 6.16 represents the limit of ultrapure crystals. It is also interesting to consider strong disorder, like, e.g. the case of stacked molecules in DNA-like structures, which can be regarded as a limit with high impurities/low crystallinity compared to the model guanine crystal. In such a system the coherent contribution vanishes (in DNA coherent tunneling is only observed experimentally across very few bases [112]) and the total mobility is then given by $\mu^{(inc)}$ in Fig. 6.16. However, for high-purity crystals as assumed here it should be possible to achieve band-like conduction at least for low T.
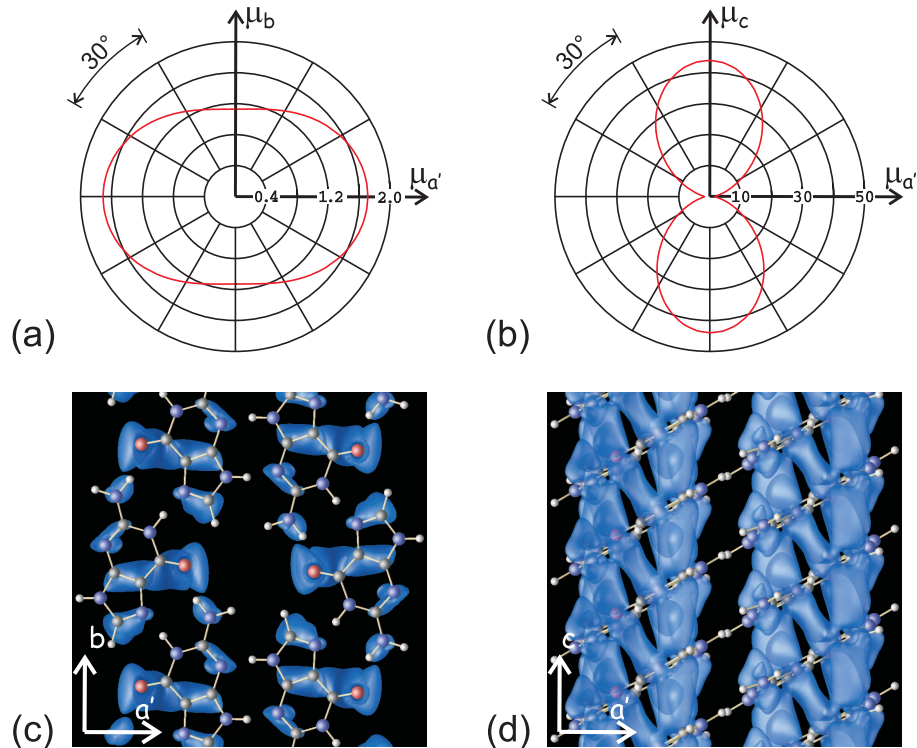
Figure 6.17: Comparison of mobility anisotropy (a), (b) and overlap of molecular orbitals (c), (d) in guanine crystals. Displayed is the hole mobility and HOMO overlap density as described in the text.

I now proceed with the discussion of the anisotropy of the charge-transport at room temperature. In order to gain a more comprehensive impression of the direction dependence, I present polar plots in Fig. 6.9 (a) and (b). Low mobilities are found in the plane perpendicular to the stacking direction ($a'b$ plane) in contrast to much ($\approx 30\times$) higher mobilities along the stack (c direction). This quasi one-dimensional characteristic is a direct consequence of the electronic coupling implied by the stacking motif (see Fig. 6.11). Although the molecules within the guanine planes are hydrogen-bridge bonded, the electronic coupling within such planes is small. In contrast, electronic coupling across the planes is strong and leads to high mobilities. A small off-angle from the low-mobility $a'b$-plane gives already strong contributions from the principal (c) direction. The discussed direction-dependence of the mobility is a direct consequence of the anisotropy of the bare electronic coupling. The reason are the relatively small non-local coupling constants for electron-phonon interaction and hence small non-local currents. [44]

As demonstrated in Sec. 6.3.4, a highly significant measure of the electronic coupling is the overlap of the involved molecular orbitals ψ_i. [58, 113] Therefore, one can directly access the origin of the mobility anisotropy by the anisotropy of the overlap of contributing electronic wavefunctions. This is studied here as well. In Fig. 6.9 (c) and (d), I have plotted the absolute value of the overlap density which is a total of all pairwise overlaps according

to $\sum'_{ij} |\psi_i(\mathbf{r})\psi_j(\mathbf{r})|$ where the sums run over all molecules but excluding $i = j$ as indicated by the prime. High density between the planes indicates a strong overlap of the π-orbitals between adjacent molecules in stacking direction (cf. Fig. 6.9 (d)). The resulting vertical columns represent hole transport channels. On the other hand, these vertical channels are very weakly connected to each other. More precisely, the overlap density between molecules of adjacent stacks is small. A view along the stacking direction (cf. Fig. 6.9 (c)) reveals the weak coupling within each stacking plane. As a result, charge carriers can hardly overcome the gaps resulting in low carrier mobility in a'- and b-direction. This is in accordance to the anisotropy factor of 30 in the mobilities seen in Fig. 6.16. For a three-dimensional view to the transport channels the reader is referred to a movie in a related publication. [111]

The most important findings of the study on guanine crystals can be summarized as follows: (i) Large bandwidths of the valence bands indicate possible high carrier mobilities in guanine crystals. (ii) The temperature dependence of the hole transport in guanine-derived systems can only be understood within the polaron concept. (iii) At room temperature only a small contribution to the mobility in guanine based materials comes from coherent transport. Due to thermal disorder, the dominating contribution originates from incoherent phonon-assisted hopping. (iv) As a consequence, no contribution to the hole mobility along a poly(dG) sequence in DNA-like structures should be due to coherent transport since the required crystallinity cannot be achieved. This, however, does not necessarily prevent high mobilities. (v) The analysis of the anisotropy of the mobility shows that transport along the stacks is strongly preferred over motion across the hydrogen bonds between the stacks. (vi) It is, however, possible to have also interstrand pathways in DNA-like structures although the hopping rate between adjacent guanines is reduced by a factor of 30. (vii) The quasi one-dimensional transport channels made visible by a novel technique are aligned along the stack in striking accordance to the calculated mobility anisotropy. (viii) The anisotropy of the bare electronic coupling is a strong indicator for the anisotropy in the carrier mobilities, even in the presence of strong polaronic effects.

Chapter 7

Summary and Outlook

7.1   Summary

In this thesis, I have presented a novel theoretical description of charge transport in organic crystals. One of the central messages from this work is that the two paradigms of coherent band transport and incoherent hopping coexist together in general and can be treated on equal footing. This leads to a polaron transport theory that bridges from Boltzmann's transport equation at low T to Marcus' electron transfer theory at high T. Thereby, it unifies the concepts of large polarons and small polarons, which were previously considered mutually exclusive. This was possible within a non-perturbative treatment of all relevant interactions. In the past, the sharp transition between the different transport mechanisms with changing temperature has led to intense discussions concerning the mechanism. Here, it is shown, that the description of this transition, supplemented by *first principles* material parameters, serves as an essential ingredient for the success of any transport theory for organic crystals. Below I briefly summarize the major findings of my thesis.

- A novel analytical expression for the charge carrier mobility has been derived.

- The non-perturbative derivation includes all orders of the electron-phonon interaction. Momentum and energy conservation are fulfilled in the contributing scattering processes.

- The mobility formula can be used directly with *ab initio* parameters for arbitrary crystalline materials and serves as a starting point for first principles studies.

- The mobility is naturally separable into two contributions: coherent band transport and incoherent thermally activated hopping, which are treated on equal footing in the theory. This gives very interesting results on the relative importance of both contributions and sheds new light on previous transport studies.

- In application to various interesting real materials, I was able to show that the famous $T^{-\gamma}$ power law dependence of the mobility on temperature can be understood as the seamless transition from coherent (band) to incoherent (hopping) transport. The parameter γ follows from the relative contribution of either transport modes.

- The new theory is superior to previous treatments of *small polaron* motion, which were based upon narrow-band theories. In the present derivation I was able to overcome the narrow-band approximation which directly leads to finite low-temperature mobilities for finite relaxation times τ. The unphysical low-temperature singularity of previous approaches is removed.

- In the limit of low temperatures, the present theory is equal to an expression derived from the Boltzmann transport equation.

- In the limit of high temperatures, the present theory obeys the same T dependence as the classical Marcus theory.

- Another strength of this theory is that the anisotropy in the mobility tensor is now much better accounted for. This improves the matching to the experimental mobility anisotropy as demonstrated for naphthalene crystals.

- The improved anisotropy description of the theory allows to analyze prevalent transport mechanisms in experiments directly from the anisotropy ratio.

- In addition to the theoretical and computational achievements I have developed a novel visualization method for the transport channels of the charge carriers. This is a very intuitive tool to gain an impression of the mobility anisotropy.

- Both durene and guanine crystals have hole bandwidths of approximately 1 eV. This highlights their potential as good charge-transport materials since these bandwidths are even larger than for the famous rubrene or the polyacene crystals.

- The polaron bandwidths are strongly narrowed compared to the bare hole bandwidths. Nevertheless, the temperature dependence of the mobility indicates predominantly band transport. In contrast, an in-depth analysis shows that hopping dominates at room temperature.

- The anisotropy of the durene hole mobilities identifies this crystal as a typical herring-bone stacked OMC with a 2D mobility characteristic (high mobilities in herring-bone plane versus low mobility perpendicular thereto) in contrast to the guanine crystal which exhibits a 1D mobility characteristic.
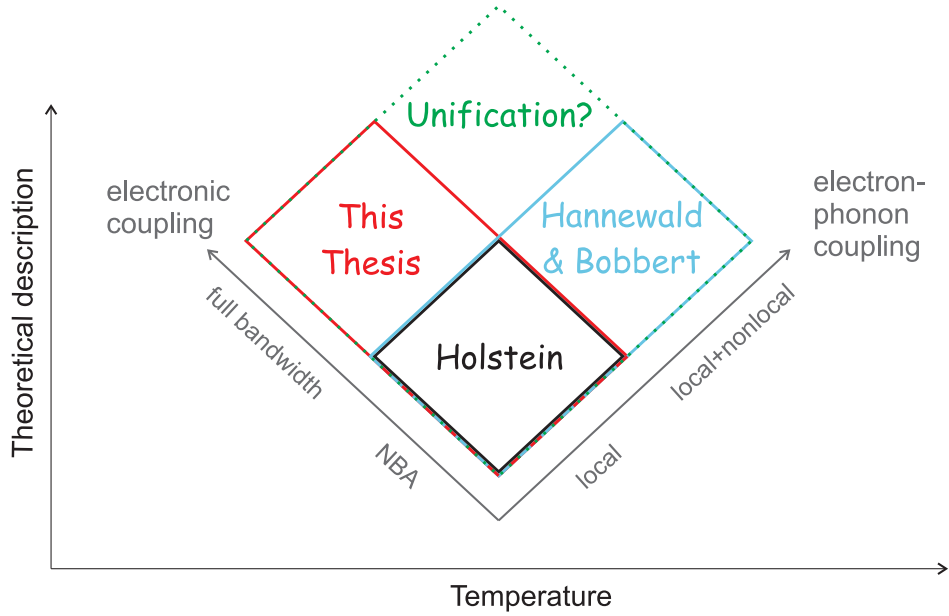
Figure 7.1: Schematic illustration of the development of the present theory (red frame) in relation to the previous theory by Hannewald and Bobbert [44] (blue frame) and Holstein's small polaron model [29] (black frame). The simultaneous description of the full bandwidth and the full electron-phonon coupling is an open question.

Finally, I hope that, taking different routes, one via an analytical treatment and another with some computational studies, this work contributes to the understanding of basic transport mechanisms in organic crystals and provides a basis for further systematic studies. Referring back to the quotations in Chap. 1, I think that at least some of the pieces of the "mobility puzzle" have been brought together, which, hopefully, stimulates further research in view of the achievements.

7.2   Outlook

With the theory developed in this thesis, the scheme in Fig. 1.1 became two-dimensional. After the extension of Holstein's model towards non-local electron-phonon coupling by Hannewald and Bobbert (first dimension), this second dimension into the direction of the full bandwidth has been explored. However, one domain (green question mark in Fig. 7.1) is still missing, which is needed to unify both theories completely. This is a real challenge, since the effort for the theoretical description, which is valid for the total green domain, cannot be estimated at present. The reason is that one may not be able to take advantage of simplifications, which are helpful in one part, also in the other part and vice versa. Nevertheless an extension to the full bandwidth including also nonlocal electron-phonon coupling is needed to be able to simultaneously describe electron and hole mobilities in naphthalene for all temperatures visible in Fig. 2.1. It would also be interesting to calculate the carrier mobility

of an inorganic crystal, to explore whether a seamless transition of the presented concepts is possible. This is a quite fundamental question.

There are many further interesting open issues. This includes the influence of acoustic phonons on the transport, which has not been addressed sufficiently so far. But also the role of disorder certainly deserves particular attention and additional research. Further organic crystals like rubrene, perylene, or pentacene should be studied theoretically and compared to the experiment. Interestingly, the influence of functional groups or isotope effects may give additional insight. Another direction to extend the theoretical description would be to include higher electric fields, i.e., to go beyond the linear response. In any case, I am sure that one or the other direction will be explored in the near future.

Bibliography

[1]   M. Berggren, O. Inganäs, G. Gustafsson, J. Rasmusson, M. R. Andersson, T. Hjertberg, O.Wennerstrom. "Light-emitting-diodes wuth variable colors from polymer blends." In: *Nature* 372 (1994), p. 444.

[2]   A. J. Heeger. "Light emission from semiconducting polymers: Light-emitting diodes, light-emitting electrochemical cells, lasers and white light for the future." In: *Solid State Commun.* 107 (1998), p. 673.

[3]   S. R. Forrest. "The road to high efficiency organic light emitting devices." In: *Org. Electron.* 4 (2003), p. 45.

[4]   A. R. Brown, A. Pomp, C. M. Hart, D. M. de Leeuw. "Logic gates made from polymer transistors and their use in ring oscillators." In: *Science* 270 (1995), p. 972.

[5]   A. Dodabalapur, L. Torsi, and H. E. Katz. "Organic transistors - 2-dimensional transport and improved electrical characteristics." In: *Science* 268 (1995), p. 270.

[6]   H. Sirringhaus, N. Tessler, and R. H. Friend. "Integrated optoelectronic devices based on conjugated polymers." In: *Science* 280 (1998), p. 1741.

[7]   M. Muccini. "A bright future for organic field-effect transistors." In: *Nat. Mater.* 5 (2006), p. 605.

[8]   M. E. Gershenson, V. Podzorov, and A. F. Morpurgo. "Colloquium: Electronic transport in single-crystal organic transistors." In: *Rev. Mod. Phys.* 78 (2006), p. 973.

[9]   X. Chi, D. Li, H. Zhang, Y. Chen, V. Garcia, C. Garcia, T. Siegrist. "5,6,11,12-Tetrachlorotetracene, a tetracene derivative with [pi]-stacking structure: The synthesis, crystal structure and transistor properties." In: *Org. Electron.* 9.2 (2008), p. 234.

[10] H. Klauk, U. Zschieschang, J. Pflaum, M. Halik. "Ultralow-power organic complementary circuits." In: *Nature* 445 (2007), p. 745.

[11] H. Yan, Z. H. Chen, Y. Zheng, C. Newman, J. R. Quinn, F. Dotz, M. Kastler, A. Facchetti. "A high-mobility electron-transporting polymer for printed transistors." In: *Nature* 457 (2009), p. 679.

[12] M. Granström, K. Petritsch, A. C. Arias, A. Lux, M. R. Andersson, R. H. Friend. "Laminated fabrication of polymeric photovoltaic diodes." In: *Nature* 395 (1998), p. 257.

[13] S. E. Shaheen, C. J. Brabec, N. S. Sariciftci, F. Padinger, T. Fromherz, J. C. Hummelen. "2.5% efficient organic plastic solar cells." In: *Appl. Phys. Lett.* 78 (2001), p. 841.

[14] P. Peumans, A. Yakimov, and S. R. Forrest. "Small molecular weight organic thin-film photodetectors and solar cells." In: *J. Appl. Phys.* 93 (2003), p. 3693.

[15] O. D. Jurchescu, J. Baas, and T. T. M. Palstra. "Effect of impurities on the mobility of single crystal pentacene." In: *Appl. Phys. Lett.* 84 (2004), p. 3061.

[16] V. C. Sundar, J. Zaumseil, V. Podzorov, E. Menard, R. L. Willett, T. Someya, M. E. Gershenson, J. A. Rogers. "Elastomeric transistor stamps: Reversible probing of charge transport in organic crystals." In: *Science* 303 (2004), p. 1644.

[17] I. N. Hulea, S. Fratini, H. Xie, C. L. Mulder, N. N. Iossad, G. Rastelli, S. Ciuchi, A. F. Morpurgo. "Tunable Fröhlich polarons in organic single-crystal transistors." In: *Nat. Mater.* 5 (2006), p. 982.

[18] A. K. Tripathi and J. Pflaum. "Correlation between ambipolar transport and structural phase transition in diindenoperylene single crystals." In: *Appl. Phys. Lett.* 89 (2006), p. 082103.

[19] N. Koch, A. Vollmer, I. Salzmann, B. Nickel, H. Weiss, J. P. Rabe. "Evidence for temperature-dependent electron band dispersion in pentacene." In: *Phys. Rev. Lett.* 96 (2006), p. 156803.

[20] N. Karl. "Organic Semiconductors." In: ed. by O. Madelung, M. Schulz, and H. Weiss. Vol. 17i. Landolt-Börnstein Numerical data and functional relationships in science and technology (New Series), Group III. Berlin: Springer, 1985, pp. 106–218.

[21] W. Warta and N. Karl. "Hot holes in naphthalene: High, electric-field-dependent mobilities." In: *Phys. Rev. B* 32 (1985), p. 1172.

[22] V. Coropceanu, J. Cornil, D. A. da Silva Filho, Y. Olivier, R. Silbey, J.-L. Brédas. "Charge Transport in Organic Semiconductors." In: *Chem. Rev.* 107 (2007), p. 926.

[23] E. A. Silinish and V. Čápek. *Organic Molecular Crystals*. New York: American Institute of Physics, 1994.

[24] Y. C. Cheng, R. J. Silbey, D. A. da Silva Filho, J. P. Calbert, J. Cornil, J. L. Brédas. "Three-dimensional band structure and bandlike mobility in oligoacene single crystals: A theoretical investigation." In: *J. Chem. Phys.* 118 (2003), p. 3764.

[25] K. Hannewald, V. M. Stojanović, J. M. T. Schellekens, P. A. Bobbert, G. Kresse, J. Hafner. "Theory of polaron band width narrowing in organic molecular crystals." In: *Phys. Rev. B* 69 (2004), p. 075211.

[26] K. Hummer and C. Ambrosch-Draxl. "Electronic properties of oligoacenes from first principles." In: *Phys. Rev. B* 72 (2005), p. 205205.

[27] G. Koller, S. Berkebile, M. Oehzelt, P. Puschnig, C. Ambrosch-Draxl, F. P. Netzer, M. G. Ramsey. "Intra- and Intermolecular Band Dispersion in an Organic Crystal." In: *Science* 317 (2007), p. 351.

[28] A. Troisi and G. Orlandi. "Charge-Transport Regime of Crystalline Organic Semiconductors: Diffusion Limited by Thermal Off-Diagonal Electronic Disorder." In: *Phys. Rev. Lett.* 96 (2006), p. 086601.

[29] T. Holstein. "Studies of Polaron Motion, Part II." In: *Ann. Phys.* 8 (1959), p. 343.

[30] G. D. Mahan. *Many-Particle Physics*. New York: Kluwer Academic Publishers, 2000.

[31] K. Hannewald and P. A. Bobbert. "Ab initio theory of charge-carrier transport in ultrapure organic crystals." In: *Appl. Phys. Lett.* 85 (2004), p. 1535.

[32] R. J. Silbey and R. W. Munn. "General theory of electronic transport in molecular crystals. I. Local linear electron-phonon coupling." In: *J. Chem. Phys.* 72 (1980), p. 2763.

[33] V. M. Kenkre, J. D. Andersen, D. H. Dunlap, C. B. Duke. "Unified Theory of the Mobilities of Photoinjected Electrons in Naphthalene." In: *Phys. Rev. Lett.* 62 (1989), p. 1165.

[34] V. M. Kenkre. "Finite-bandwidth calculations for charge carrier mobility in organic crystals." In: *Phys. Lett. A* 305 (2002), p. 443.

[35] S. Fratini and S. Ciuchi. "Dynamical Mean-Field Theory of Transport of Small Polarons." In: *Phys. Rev. Lett.* 91 (2003), p. 256403.

[36] L. Giuggioli, J. D. Anderson, and V. M. Kenkre. "Mobility theory of intermediate-bandwidth carriers in organic crystals: Scattering by acoustic and optical phonons." In: *Phys. Rev. B* 67 (2003), p. 045110.

[37] Y. C. Cheng and R. J. Silbey. "A unified theory for charge-carrier transport in organic crystals." In: *J. Chem. Phys.* 128 (2008), p. 114713.

[38] M. Hultell and S. Stafström. "Polaron dynamics in highly ordered molecular crystals." In: *Chem. Phys. Lett.* 428 (2006), p. 446.

[39] Z. Burshtein and D. F. Williams. "Temperature dependence and anisotropy of charge carrier mobilities in durene." In: *Phys. Rev. B* 15 (1977), p. 5769.

[40] J. E. Anthony, J. S. Brooks, D. L. Eaton, S. R. Parkin. "Functionalized Pentacene: Improved Electronic Properties from Control of Solid-State Order." In: *J. Am. Chem. Soc.* 123 (2001), p. 9482.

[41] V. Podzorov, E. Menard, A. Borissov, V. Kiryukhin, J. A. Rogers, M. E. Gershenson. "Intrinsic Charge Transport on the Surface of Organic Semiconductors." In: *Phys. Rev. Lett.* 93 (2004), p. 086602.

[42] R. Zeis, C. Besnard, T. Siegrist, C. Schlockermann, X. L. Chi, C. Kloc. "Field effect studies on rubrene and impurities of rubrene." In: *Chem. Mater.* 18 (2006), p. 244.

[43] J. Y. Lee, S. Roth, and Y. W. Park. "Anisotropic field effect mobility in single crystal pentacene." In: *Appl. Phys. Lett.* 88 (2006), p. 252106.

[44] K. Hannewald and P. A. Bobbert. "Anisotropy effects in phonon-assisted charge-carrier transport in organic molecular crystals." In: *Phys. Rev. B* 69 (2004), p. 075212.

[45] E. M. Conwell. *High Field Transport in Semiconductors*. New York: Academic Press, 1967.

[46] R. A. Marcus and N. Sutin. "Electron transfer in chemistry and biology." In: *Biochim. Biophys. Acta* 811 (1985), p. 265.

[47] R. A. Marcus. "Electron transfer reactions in chemistry. Theory and experiment." In: *Rev. Mod. Phys.* 65 (1993), p. 599.

[48] F. Ortmann, K. Hannewald, and F. Bechstedt. "*Ab initio* studies of structural, vibrational, and electronic properties of durene crystals and molecules." In: *Phys. Rev. B* 75 (2007), p. 195219. DOI: 10.1103/PhysRevB.75.195219.

[49] F. Ortmann, K. Hannewald, and F. Bechstedt. "Guanine crystals: A first principles study." In: *J. Phys. Chem. B* 112 (2008), p. 1540. DOI: 10.1021/jp076455t.

[50] A. Troisi and G. Orlandi. "Dynamics of the Intermolecular Transfer Integral in Crystalline Organic Semiconductors." In: *J. Phys. Chem. A* 110 (2006), p. 4065.

[51] T. Holstein. "Studies of Polaron Motion, Part I." In: *Ann. Phys.* 8 (1959), p. 325.

[52] N. W. Ashcroft and N. D. Mermin. *Solid State Physics*. Philadelphia: Saunders, 1976.

[53] I. G. Lang and Y. A. Firsov. "Kinetic theory of semiconductors with low mobility." In: *Sov. Phys. JETP* 16 (1963), p. 1301.

[54]   R. G. Kepler. "Charge Carrier Production and Mobility in Anthracene Crystals." In: *Phys. Rev.* 119 (1960), p. 1226.

[55]   O. H. Leblanc. "Hole and Electron Drift Mobilities in Anthracene." In: *J. Chem. Phys.* 33 (1960), p. 626.

[56]   J. M. Ziman. *Electrons and Phonons.* Oxford: Clarendon Press, 2001.

[57]   D. K. Ferry. *Semiconductor Transport.* London: Taylor & Francis, 2000.

[58]   F. Ortmann, K. Hannewald, and F. Bechstedt. "Ab initio description and visualization of charge transport in durene crystals." In: *Appl. Phys. Lett.* 93 (2008), p. 222105. DOI: 10.1063/1.3033830.

[59]   F. J. Morin. "Lattice-Scattering Mobility in Germanium." In: *Phys. Rev.* 93 (1954), p. 62.

[60]   F. J. Morin and J. P. Maita. "Electrical Properties of Silicon Containing Arsenic and Boron." In: *Phys. Rev.* 96 (1954), p. 28.

[61]   P. Blood. "Electrical Properties of *n*-Type Epitaxial GaAs at High Temperatures." In: *Phys. Rev. B* 6 (1972), p. 2257.

[62]   G. G. Roberts, N. Apsley, and R. W. Munn. "Temperature dependent electronic conduction in semiconductors." In: *Phys. Rep.* 60 (1980), p. 59.

[63]   G. Kresse and J. Furthmüller. "Efficiency of *ab-initio* total energy calculations for metals and semiconductors using a plane-wave basis set." In: *Comput. Mater. Sci.* 6 (1996), p. 15.

[64]   G. Kresse and J. Furthmüller. "Efficient iterative schemes for ab initio total-energy calculations using a plane-wave basis set." In: *Phys. Rev. B* 54 (1996), p. 11169.

[65]   G. Kresse and D. Joubert. "From ultrasoft pseudopotentials to the projector augmented-wave method." In: *Phys. Rev. B* 59 (1998), p. 1758.

[66]   M. Preuss, W. G. Schmidt, K. Seino, J. Furthmüller, F. Bechstedt. "Ground- and Excited-State Properties of DNA Base Molecules from Plane-Wave Calculations using Ultrasoft Pseudopotentials." In: *J. Comput. Chem.* 25 (2004), p. 112.

[67]   R. Maul, F. Ortmann, M. Preuss, K. Hannewald, F. Bechstedt. "DFT studies using supercells and projector-augmented waves for structure, energetics, and dynamics of glycine, alanine, and cysteine." In: *J. Comput. Chem.* 28 (2007), p. 1817. DOI: 10.1002/jcc.20683.

[68]   R. Maul, M. Preuss, F. Ortmann, K. Hannewald, F. Bechstedt. "Electronic excitations of glycine, alanine, and cysteine conformers from first-principles." In: *J. Phys. Chem. A* 111 (2007), p. 4370. DOI: 10.1021/jp068294j.

[69]   H. J. Monkhorst and J. D. Pack. "Special points for Brillouin-zone integrations." In: *Phys. Rev. B* 13 (1976), p. 5188.

[70]   J. P. Perdew and A. Zunger. "Self-interaction correction to density-functional approximations for many-electron systems." In: *Phys. Rev. B* 23 (1981), p. 5048.

[71]   J. P. Perdew. In: *Electronic Structure of Solids '91.* Ed. by P. Ziesche and H. Eschrig. Berlin: Akademie-Verlag, 1991, p. 11.

[72]   D. R. Hamann. "H_2O hydrogen bonding in density-functional theory." In: *Phys. Rev. B* 55 (1997), R10157.

[73]   J. P. Perdew, J. A. Chevary, S. H. Vosko, K. A. Jackson, M. R. Pederson, D. J. Singh, C. Fiolhais. "Atoms, molecules, solids and surfaces: Applications of the generalized gradient approximation." In: *Phys. Rev. B* 46 (1992), p. 6671.

[74] F. Ortmann, F. Bechstedt, and W. G. Schmidt. "Semiempirical van der Waals correction to the density functional description of solids and molecular structures." In: *Phys. Rev. B* 73 (2006), p. 205101. DOI: 10.1103/PhysRevB.73.205101.

[75] F. Ortmann, W. G. Schmidt, and F. Bechstedt. "Attracted by long-range electron correlation: Adenine on graphite." In: *Phys. Rev. Lett.* 95 (2005), p. 186101. DOI: 10.1103/PhysRevLett.95.186101.

[76] W. G. Schmidt, K. Seino, M. Preuss, A. Hermann, F. Ortmann, F. Bechstedt. "Organic molecule adsorption on solid surfaces: chemical bonding, mutual polarisation and dispersion interaction." In: *Appl. Phys. A* 85 (2006), p. 387. DOI: 10.1007/s00339-006-3691-0.

[77] M. Preuss and F. Bechstedt. "Vibrational spectra of ammonia, benzene, and benzene adsorbed on Si (001) by first principles calculations with periodic boundary conditions." In: *Phys. Rev. B* 73 (2006), p. 155413.

[78] R. O. Jones and O. Gunnarsson. "The density functional formalism, its applications and prospects." In: *Rev. Mod. Phys.* 61 (1989), p. 689.

[79] P. Hohenberg and W. Kohn. "Inhomogeneous Electron Gas." In: *Phys. Rev.* 136 (1964), B864.

[80] W. Kohn and L. J. Sham. "Self-consistent equations including exchange and correlation effects." In: *Phys. Rev.* 140 (1965), A1133.

[81] C. H. Stam. "Refinement of crystal-structure of durene." In: *Acta Crystallogr. B* 28 (1972), p. 2630.

[82] E. Prince, L. W. Schroeder, and J. J. Rush. "A constrained refinement of the structure of durene." In: *Acta Cryst.* B 29 (1973), p. 184.

[83] M. Plazanet, M. R. Johnson, J. D. Gale, T. Yildirim, G. J. Kearley, M. T. Fernández-Díaz, D. Sánchez-Portal, E. Artacho, J. M. Soler, P. Ordejón, A. Garcia, H. P. Trommsdorff. "The structure and dynamics of crystalline durene by neutron scattering and numerical modelling using density functional methods." In: *Chem. Phys.* 261 (2000), p. 189.

[84] C. B. Harris, R. M. Shelby, and P. A. Cornelius. "Effects of Energy Exchange on Vibrational Dephasing Times in Raman Scattering." In: *Phys. Rev. Lett.* 38 (1977), p. 1415.

[85] S. Marks, P. A. Cornelius, and C. B. Harris. "A critical test of vibrational dephasing theories in solids using spontaneous Raman scattering in isotopically mixed crystals." In: *J. Chem. Phys.* 73 (1980), p. 3069.

[86] A. Pawlukojć, I. Natkaniec, G. Bator, L. Sobczyk, E. Grech, J. Nowicka-Scheibe. "Low frequency internal modes of 1,2,4,5-tetramethylbenzene, tetramethylpyrazine and tetramethyl-1,4-benzoquinone INS, Raman, infrared and theoretical DF studies." In: *Spectrochim. Acta A* 63 (2006), p. 766.

[87] A. K. Tripathi, C. Arndt, and J. Pflaum. private communication.

[88] G. R. Desiraju and T. Steiner. *The Weak Hydrogen Bond in Structural Chemistry and Biology.* NY: Oxford University Press, 1999.

[89] A. Hadni, B. Wyncke, G. Morlot, X. Gerbaux. "Translational Frequencies of Molecules in Naphtalene, Durene, and Anthracene Single Crystals at Low Temperatures." In: *J. Chem. Phys.* 51 (1969), p. 3514.

[90] F. Ortmann, K. Hannewald, and F. Bechstedt. "Electronic properties of durene crystals: Implications for charge transport." In: *Phys. Stat. Sol. b* 245 (2008), p. 825. DOI: 10.1002/pssb.200743427.

[91]   G. B. Schuster, ed. *Long-Range Charge Transfer in DNA II*. Topics in Current Chemistry, Vol. 237. Berlin/Heidelberg: Springer, 2004.

[92]   D. D. Eley and D. I. Spivey. "Semiconductivity of Organic Substances." In: *Trans. Faraday Soc.* 58 (1962), p. 411.

[93]   C. A. Mirkin, R. L. Letsinger, R. C. Mucic, J. J. Storhorff. "A DNA-based method for rationally assembling nanoparticles into macroscopic materials." In: *Nature* 382 (1996), p. 607.

[94]   A. P. Alivisatos, K. P. Johnsson, X. Peng, T. E. Wilson, C. J. Loweth, M. P. Bruchez, P. G. Schultz. "Organization of 'nanocrystal molecules'." In: *Nature* 382 (1996), p. 609.

[95]   E. Braun, Y. Eichen, U. Sivan, G. Ben-Yoseph. "DNA-templated assembly and electrode attachment of a conducting silver wire." In: *Nature* 391 (1998), p. 775.

[96]   H.-W. Fink and C. Schönenberger. "Electrical conduction through DNA molecules." In: *Nature* 398 (1999), p. 407.

[97]   P. J. de Pablo, F. Moreno-Herrero, J. Colchero, J. Gómez Herrero, P. Herrero, A. M. Baró, Pablo Ordejón, José M. Soler, Emilio Artacho. "Absence of dc-Conductivity in λ-DNA." In: *Phys. Rev. Lett.* 85 (), p. 4992.

[98]   B. Giese, J. Amaudrut, A.-K. Köhler, M. Spormann, S. Wessely. "Direct observations of hole transfer through DNA by hopping between adenin bases and by tunneling." In: *Nature* 412 (2001), p. 318.

[99]   R. G. Endres, D. L. Cox, and R. R. P. Singh. "Colloquium: The quest for high-conductance DNA." In: *Rev. Mod. Phys.* 76 (2004), p. 195.

[100]   H. Cohen, C. Nogues, R. Naaman, D. Porath. "Direct measurement of electrical transport through single DNA molecules of complex sequence." In: *Proc. Nat. Acad. Sci.* 102 (2005), p. 11589.

[101]   G. Maruccio, P. Visconti, V. Arima, S. D'Amico, A. Biasco, E. D'Amone, R. Cingolani, R. Rinaldi, S. Masiero, T. Giorgi, G. Gottarelli. "Field Effect Transistor Based on a Modified DNA Base." In: *Nano Lett.* 3 (2003), p. 479.

[102]   R. Di Felice, A. Calzolari, E. Molinari, A. Garbesi. "Ab initio study of model guanine assemblies: The role of π-π coupling and band transport." In: *Phys. Rev. B* 65 (2001), p. 045104.

[103]   M. Plazanet, N. Fukushima, and M. R. Johnson. "Modelling molecular vibrations in extended hydrogen-bonded networks – crystalline bases of RNA and DNA and the nucleosides." In: *Chem. Phys.* 280 (2002), p. 53.

[104]   P. Otto, E. Clementi, and J. Ladik. "The electronic structure of DNA related periodic polymers." In: *J. Chem. Phys.* 78 (1983), p. 4547.

[105]   F. Bogár and J. Ladik. "Correlation corrected energy bands of nucleotide base stacks." In: *Chem. Phys.* 237 (1998), p. 273.

[106]   U. Thewalt, C. E. Bugg, and R. E. Marsh. "The Crystal Structure of Guanine Monohydrate." In: *Acta Cryst.* B 27 (1971), p. 2358.

[107]   S. J. Sowerby, M. Edelwirth, and W. M. Heckl. "Self-Assembly at the Prebiotic Solid-Liquid Interface: Structures of Self-Assembled Monolayers of Adenine and Guanine Bases Formed on Inorganic Surfaces." In: *J. Phys. Chem. B* 102 (1998), p. 5914.

[108]   K. Phillips, Z. Dauter, A. I. H. Murchie, D. M. J. Lilley, B. Luisi. "The crystal structure of a parallel-stranded guanine tetraplex at 0.95 angstrom resolution." In: *J. Mol. Biol.* 273 (1997), p. 171.

[109]   P. H. Hahn, W. G. Schmidt, K. Seino, M. Preuss, F. Bechstedt, J. Bernholc. "Optical absorption of water: Coulomb effects versus hydrogen bonding." In: *Phys. Rev. Lett.* 94 (2005), p. 037404.

[110]   I. Saito, T. Nakamura, K. Nakatani, Y. Yoshioka, K. Yamaguchi, H. Sugiyama. "Mapping of the Hot Spots for DNA Damage by One-Electron Oxidation: Efficiency of GG Doublets and GGG Triplets as a Trap in Long-Range Hole Migration." In: *J. Am. Chem. Soc.* 120 (1998), p. 12686.

[111]   F. Ortmann, K. Hannewald, and F. Bechstedt. "Charge Transport in Guanine-Based Materials." In: *J. Phys. Chem. B* 113 (2009), p. 7367. DOI: `10.1021/jp901029t`.

[112]   F. D. Lewis, T. Wu, Y. Zhang, R. L. Letsinger, S. R. Greenfield, M. R. Wasielewski. "Distance-Dependent Electron Transfer in DNA Hairpins." In: *Science* 277 (1997), p. 673.

[113]   J.-L. Brédas, J. P. Calbert, D. A. da Silva Filho, J. Cornil. "Organic Semiconductors: A theoretical characterization of the basic parameters governing charge transport." In: *Proc. Natl. Acad. Sci. USA* 99 (2002), p. 5804.

Deutsche Zusammenfassung

Das Verstehen des Ladungstransports ist einer der zentralen Schwerpunkte bei der Untersuchung von halbleitenden Kristallen. Insbesondere das komplexe Zusammenspiel zwischen Elektronen und Phononen in den dabei relevanten Streuprozessen ist nur auf quantenmechanischer Grundlage beschreibbar. Für Materialien mit starker Kopplung der elektronischen und vibronischen Freiheitsgrade sind diese Prozesse und damit auch die charakteristischen Eigenschaften der resultierenden Ladungsträgermobilität bisher nur unvollständig verstanden. Insbesondere gilt dies für die organischen Kristalle, die in den letzten Jahren wegen ihrer Bedeutung für die organische Elektronik stark in den Forschungsfokus gerückt sind.

Die vorliegende Arbeit beschäftigt sich mit dem Ladungstransport durch organische Kristalle. Die im Rahmen meiner Dissertation erhaltenen Ergebnisse sind in ihrer Darstellung unterteilt in einen theoretischen Teil und einen anwendenden Teil. Der theoretische Teil beschreibt die mikroskopische Modellierung des Ladungstransports durch Kristalle im Allgemeinen, wobei besonderes Augenmerk auf der Beschreibung der Elektron-Phonon-Wechselwirkung liegt. Gerade dieser Streukanal bestimmt für ultrareine Kristalle maßgeblich die Größe der Ladungsträgermobilität und deren Temperaturabhängigkeit. Andere Streuprozesse werden effektiv behandelt. Der zweite Teil stellt die Ergebnisse zur temperatur- und richtungsabhängigen Mobilität für einige ausgewählte organische Molekülkristalle vor. Hierbei fokussiere ich insbesondere auf die Darstellung des Zusammenhangs zwischen Anisotropie in der Mobilität und Struktur der Kristalle.

Von theoretischer Seite wird gezeigt, wie die beiden Konzepte des Bandtransports und der Hüpfbewegung konsistent innerhalb eines Formalismus beschreibbar sind. Ein im Rahmen des Kubo-Formalismus abgeleiteter neuartiger expliziter Ausdruck für die Mobilität beinhaltet vollständig beide Transportmechanismen, welche sich auf natürliche Weise aus einer Separation der beitragenden Terme ergeben. Die Gültigkeit dieser Mobilitätsformel reicht vom Geltungsbereich der Boltzmann-Gleichung für tiefe Temperaturen bis zu hohen Temperaturen, dem klassischen Anwendungsgebiet der Marcus-Theorie. Es wird gezeigt, wie beide Grenzfälle enthalten sind. Das entspricht einer vereinheitlichten Beschreibung von delokalisierten Bloch-Elektronen, schwach lokalisierten („großen") Polaronen und stark lokalisierten („kleinen")

Polaronen. Die konzeptionelle Erweiterung des ursprünglichen Holstein-Modells kleiner Polaronen ist nicht-störungstheoretisch bezüglich der Elektron-Phonon-Kopplung vollzogen worden. Es ergeben sich über die Elektron-Phonon-Streuung stark temperaturabhängige Beiträge des kohärenten und nicht-kohärenten Transports. Die starke Temperaturabhängigkeit vermag erstmals die Schwierigkeiten oder Inkonsistenzen zu erklären, die bei früheren Beschreibungen der Ladungsträgermobilität in Molekülkristallen unter Beschränkung auf nur einen der beiden Transportmechanismen auftraten.

Bei der Herleitung der neuen Mobilitätstheorie wurden so fundamentale Konzepte wie Energie- und Impulserhaltung bei den elementaren Streuereignissen berücksichtigt, was nur dadurch möglich wurde, dass über die sonst übliche Näherung schmaler Bänder hinausgegangen wurde. Als wichtiges Ergebnis dessen wurde insbesondere eine unphysikalische Singularität für den Tieftemperaturgrenzfall behoben, die in früheren Erweiterungen des Holstein-Modells stets present war. Durch den nahtlosen Übergang zum Bandtransport bei niedrigen Temperaturen ermöglicht die Theorie auch eine im Allgemeinen bessere Beschreibung der Richtungsabhängigkeit der Mobilität. Dies wurde in Anwendung auf Naphthalin exemplarisch gezeigt, was zu einer besseren Übereinstimmung in Vergleich zum Experiment führt und eine weitere wesentliche Verbesserung der theoretischen Beschreibung darstellt.

Der resultierende Ausdruck für die Ladungsträgermobilität lässt sich direkt mit Materialparametern von Kristallen auswerten. Diese Größen können, wie in der Anwendung gezeigt, aus sog. *first principles* oder *ab initio* Rechnungen (parameterfreie Methoden) wie etwa der Dichtefunktional-Theorie gewonnen werden. Diese Dissertation ist somit ein Ausgangspunkt für eine *ab initio*-Beschreibung des Ladungstransports.

Die Anwendung dieser *ab initio*-Beschreibung des Ladungstransports ist ein zentraler Bestandteil meiner Studien zu einzelnen Molekülkristallen. Neben dem bereits erwähnten Naphthalin (engl.: naphthalene), wurden erstmalig auch Durol (engl.: durene) und Guanin (engl.: guanine) studiert. Die Untersuchungen zu Durol und Guanin beinhalten zudem umfangreiche strukturelle Charakterisierungen und detaillierte Analysen der Gitterschwingungen und elektronischen Struktur.[1] Die Breite der Valenzbänder beider Kristalle ist außerordentlich hoch im Vergleich zu den für den Ladungstransport favorisierten Oligoacen-Kristallen oder Rubren, was ihre Bedeutung für den Ladungstransport hervorhebt. Die temperaturabhängigen Polaron-Bandbreiten sind hingegen stark reduziert. Die berechneten Löcher-Mobilitäten deuten zwar zunächst dennoch auf einen bandartigen Transportmechanismus hin, was im Falle von Durol auch mit experimentellen Ergebnissen korelliert, aber durch eingehende Untersuchungen konnte gezeigt werden, dass bei Raumtemperatur tatsächlich der Hüpfmechanismus

---

[1]Nicht alle Ergebnisse konnten in die Dissertation aufgenommen werde. Siehe angegebene Publikationen für ausführlichere Betrachtungen.

dominiert.

Sowohl Durol- als auch Guanin-Kristalle zeigen eine starke Anisotropie in der Löcher-Mobilität. Bei Durol zeigt sich eine zweidimensionale Charakteristik, bei der hohe Mobilitäten in der Ebene des Fischgräten-Musters auftreten, während senkrecht zu dieser Ebene viel niedrigere Werte erreicht werden. Im Gegensatz dazu zeigt der Guanin-Kristall relativ hohe Mobilitäten nur entlang einer Richtung, während in der Ebene senkrecht dazu die Werte deutlich kleiner sind und sich somit eine eindimensionale Charakteristik ergibt. Die Beziehung zur Struktur der Kristalle und den elektronischen Eigenschaften wurde erläutert. Insbesondere eine 3D-Visualisierung der anisotropen „Transport-Kanäle" ermöglicht ein tieferes Verständnis für den Zusammenhang von Struktur und Transporteigenschaften. Dazu wurde eine neue Methode der Darstellung entwickelt, die insbesondere die Unterschiede zwischen den Kristallen eindrucksvoll aufzeigt.

Abschließend hoffe ich, dass die zusammenhängende Arbeit aus einem analytisch modellierenden Teil und einem auf ausgewählte Kristalle anwendenden Teil zum grundlegenden Verständnis des Ladungstransports in Molekül-Kristallen beiträgt und zudem als Grundlage zu weiteren Untersuchungen anregt.

Danksagung

Mein Dank gilt Prof. Friedhelm Bechstedt und Dr. Karsten Hannewald für die Betreuung meiner Dissertation. Ich habe sehr von ihren Erfahrungen profitiert. Insbesondere für die vielen Fragen, die ich bei der Einarbeitung in dieses Gebiet hatte, hat sich Karsten viel Zeit genommen. Auch bei der Weiterentwicklung der theoretischen Grundlagen sind beide unschätzbare Gesprächspartner gewesen.

Darüberhinaus gilt mein Dank allen Kollegen der Arbeitsgruppe Festkörpertheorie für anregende Diskussionen in entspannter Atmosphäre. Durch sie habe ich auch Einblicke in andere Methoden und Gebiete bekommen.

Besonders danke ich meiner Familie für ihre Liebe und Unterstützung.

Ehrenwörtliche Erklärung

Hiermit erkläre ich ehrenwörtlich, dass ich die vorliegende Arbeit selbständig, ohne unzulässige Hilfe Dritter und ohne Benutzung anderer als der angegebenen Hilfsmittel und Literatur angefertigt habe. Die aus anderen Quellen direkt oder indirekt übernommenen Daten und Konzepte sind unter Angabe der Quelle gekennzeichnet.

Bei der Auswahl und Auswertung folgenden Materials haben mir die nachstehend aufgeführten Personen in der jeweils beschriebenen Weise unentgeltlich geholfen:

1. Prof. Dr. sc. nat. Friedhelm Bechstedt als betreuender Hochschullehrer,
2. Dr. Karsten Hannewald in betreuender Funktion.

Weitere Personen waren an der inhaltlich-materiellen Erstellung der vorliegenden Arbeit nicht beteiligt. Insbesondere habe ich hierfür nicht die Hilfe von Vermittlungs- bzw. Beratungsdiensten (Promotionsberater oder andere Personen) in Anspruch genommen. Niemand hat von mir unmittelbar oder mittelbar geldwerte Leistungen für Arbeiten erhalten, die im Zusammenhang mit dem Inhalt der vorgelegten Dissertation stehen.

Die Arbeit wurde bisher weder im In- noch im Ausland in gleicher oder ähnlicher Form einer anderen Prüfungsbehörde vorgelegt.

Die geltende Promotionsordnung der Physikalisch-Astronomischen Fakultät ist mir bekannt.

Ich versichere ehrenwörtlich, dass ich nach besten Wissen die reine Wahrheit gesagt und nichts verschwiegen habe.

Jena, den 31. März 2009